

THESIS FOR THE DEGREE OF LICENTIATE OF ENGINEERING

**Subsynchronous Resonance in Doubly-Fed Induction
Generator Based Wind Farms**

SELAM CHERNET



Department of Energy and Environment
CHALMERS UNIVERSITY OF TECHNOLOGY
Gothenburg, Sweden, 2016

Subsynchronous Resonance in Doubly-Fed Induction Generator Based Wind Farms
SELAM CHERNET

© SELAM CHERNET, 2016.

Division of Electric Power Engineering
Department of Energy and Environment
Chalmers University of Technology
SE-412 96 Gothenburg
Sweden
Telephone +46 (0)31-772 1000

Printed by Chalmers Reproservice
Gothenburg, Sweden, 2016

To mom who inspires me!

Subsynchronous Resonance in Doubly-Fed Induction Generator Based Wind Farms
SELAM CHERNET
Department of Energy and Environment
Chalmers University of Technology

Abstract

The objective of this thesis is to investigate the risk for instabilities due to SubSynchronous Resonances (SSR) conditions in large wind farms connected to series-compensated transmission lines. In particular, the focus is on Doubly-Fed Induction Generator (DFIG) based wind farms. Analytical models of the system under investigation are derived in order to understand the root causes that can lead to instabilities. A frequency dependent approach, based on the Nyquist criterion, has been applied in order to investigate the risk for SSR in DFIG based wind turbines. Through this approach, it is shown that the observed phenomenon is mainly due to an energy exchange between the power converter of the turbine and the series compensated grid. This phenomenon, here referred to as SubSynchronous Controller Interaction (SSCI), is driven by the control system of the turbine, which presents a non-passive behavior in the subsynchronous frequency range. The different factors that impact the frequency characteristic of the wind turbine, thereby making the system prone to SSCI interaction, have been investigated. Through this analysis, it is shown that in a DFIG wind turbine, the current controller in the rotor-side converter plays a major role and that the risk for SSR increases when increasing its closed-loop bandwidth. In addition, it is shown that the output power generated from the wind turbine has an impact on the frequency characteristic of the turbine.

Time-domain studies are performed on an aggregated wind turbine model connected to a series-compensated transmission line with the objective of verifying the analytical results obtained through frequency-domain analysis. Based on the theoretical analysis, mitigation strategies are proposed in order to shape the impedance behavior of the wind turbine in the incident of SSCI. The effectiveness of the proposed mitigation strategies are evaluated both theoretically through frequency domain analysis and using detailed time-domain simulations.

Index Terms: Wind power, Doubly-Fed Induction Generator (DFIG), SubSynchronous Resonance (SSR), SubSynchronous Controller Interaction (SSCI), Induction Generator Effect (IGE), impedance-based analysis, passivity.

Acknowledgments

My sincere gratitude goes to my supervisor Prof. Massimo Bongiorno for his technical guidance, immense encouragement, and continuous support during this research work. Prof. Massimo's patience, positive attitude and exemplary guidance have been my immense inspirations throughout this period. I would also like to extend my thanks to my examiner Prof. Torbjörn Thiringer for the interesting discussion sessions and his invaluable comments. Moreover, I would like to thank both these professors for giving me the opportunity of coming back to Chalmers.

I would also like to thank Dr. Hector Zelaya De La Parra, from ABB corporate research, as well as Dr. Stefan Lundberg for being my co-supervisors during the first half of this work. I would also like to express my gratitude to Dr. Mebtu Beza for being my co-supervisor during the past year as well as for the countless fruitful discussions and friendship throughout my time in Chalmers.

The financial support for the project granted by ABB is greatly appreciated. Additionally, I would like to extend my special thanks to Dr. Georgios Demetriades and Dr. Jan Svensson, from ABB corporate research, for their helpful and constructive comments during our meetings. I would also like to thank Prof. Lennart Harnefors for his insightful guidance at the start of this work. My acknowledgment also goes out to the dynamic team at Vestas Wind Systems: Dr. Gert K. Andersen, Dr. Torsten Lund and Prof. Philip Carne Kjaer for their knowledgeable and practical inputs while carrying out this work.

Many thanks to the members of the division who have assisted me in several ways and helped to create a fun working environment. A special thanks to my roommate Ehsan Berhrouzian for making our room the best in the division.

Finally, I would like to extend my gratefulness to the almighty God for all the blessings in my life. My Parents, Tesfaye Chernet and Ghiday G/Egzibher and my siblings, Rahwa Tesfaye and Nebyou Tesfaye, thank you for your endless love and support throughout my life. Last but not least, I would like to thank my husband Markos Kassa, for his love, support, encouragement and understanding. Thank you for challenging and inspiring me. I love you!

Selam Chernet
Gothenburg, Sweden
September, 2016

List of Acronyms

SSR	Sub-synchronous Resonance
SSCI	Sub Synchronous Control Interaction
IM	Induction Machine
IGE	Induction Generator Effect
TI	Torsional Interaction
TA	Torque Amplification
MMF	Magnetic Motive Force
FSM	Frequency Scanning Method
EMTP	Electro Magnetic Transient Program
SISO	Single Input Single Output
IEEE	Institute of Electrical and Electronics Engineers
IEEE FBM	IEEE First Benchmark Model
IEEE SBM	IEEE Second Benchmark Model
FSIG	Fixed Speed Induction Generator
FPC	Full Power Converter
DFIG	Doubly-Fed Induction Generator
SCIG	Squirrel Cage Induction Generator
BTB	Back To Back
RSC	Rotor Side Converter
GSC	Grid Side Converter
DC	Direct Current
pu	per unit
LPF	Low Pass Filter
WRIG	Wound Rotor Induction Generator
VSC	Voltage Source Converter
IGBT	Insulated Gate Bipolar Transistor
PLL	Phase Locked Loop
IMC	Internal Mode Control
PCC	Point of Common Coupling
AGO	Advanced Grid Operation
FRT	Fault Ride Through
STATCOM	Static Synchronous Compensator
SVC	Static Var Compensator
GCSC	Gate-Controlled Series Capacitor

TCSC	Thyristor Controlled Series Capacitors
EA	Estimation Algorithm
LPF-EA	Low-Pass Filter based Estimation Algorithm
FLL	Frequency-Locked Loop

Contents

Abstract	v
Acknowledgments	vii
List of Acronyms	ix
Contents	xi
1 Introduction	1
1.1 Background and motivation	1
1.2 Aim of the thesis and main contribution	2
1.3 Structure of the thesis	3
2 Subsynchronous Resonance in Power Systems	5
2.1 Introduction	5
2.2 SSR definition and classification	6
2.3 SSR analysis and investigation methods	7
2.3.1 Frequency Scanning Method	8
2.3.2 Eigenvalue analysis	8
2.3.3 Time domain simulations	8
2.3.4 Input admittance approach	8
2.4 SSR in classical generator units	9
2.5 SSR in wind generator units	13
2.5.1 SSR in fixed speed wind turbine	14
2.5.2 SSR in doubly fed induction generator	21
2.5.3 SSR in full-power converter wind turbines	22
2.6 Conclusion	23

Contents

3	DFIG Wind Turbine Model and Control	25
3.1	Introduction	25
3.2	DFIG wind turbine model	25
3.2.1	Induction generator	26
3.2.2	DC-link model	28
3.2.3	Protection for DFIG	28
3.3	DFIG control	29
3.3.1	Rotor-side converter controller	29
3.3.2	Grid-side converter controller	34
3.3.3	Phase-locked loop	38
3.4	Conclusion	40
4	System Admittance Modeling	41
4.1	Introduction	41
4.2	Investigated system overview	42
4.3	Grid admittance	43
4.4	DFIG admittance	45
4.4.1	WRIG with rotor-side current controller	46
4.4.2	Grid-side filter with GSC current controller	50
4.4.3	Combined WRIG, RSC and GSC current controllers	51
4.4.4	Active and reactive power controllers	52
4.4.5	DC-link voltage controller	54
4.4.6	Combined subsystems	57
4.4.7	Model verification	59
4.5	Conclusion	61
5	Frequency domain stability analysis and verification	63
5.1	Frequency domain stability analysis approach	64
5.2	Frequency domain analysis for DFIG system	65
5.2.1	Influence of induction generator	66
5.2.2	Influence of rotor-side converter	68
5.2.3	Influence of grid-side converter	74
5.2.4	Influence of operating condition	76
5.3	Frequency domain analysis for transmission line	78

5.4	Frequency domain stability analysis for interconnected system	80
5.4.1	Influence of controller parameters on system stability	81
5.4.2	Influence of operating condition on overall system stability	85
5.5	Conclusion	88
6	Utilization of DFIG Controller for SSR Mitigation	91
6.1	Introduction	91
6.2	DFIG turbine modification for SSR mitigation	92
6.2.1	Controller parameter variation for SSR mitigation - Passive mitigation .	92
6.2.2	SSR mitigation using controller variation - Active SSR mitigation . . .	94
6.2.3	Proposed SSR mitigation	94
6.3	Frequency domain stability analysis for modified system	98
6.3.1	Passive mitigation	98
6.3.2	Active mitigation	100
6.4	Time domain based simulation verification	101
6.5	Conclusion	104
7	Conclusions and future work	105
7.1	Conclusions	105
7.2	Future work	106
	References	109
A	Transformation for three-phase system	117
A.1	Introduction	117
A.1.1	Transformation of three-phase quantities into vectors	117
A.1.2	Transformation from fixed to rotating reference frame	118
B	Benchmark Model for SSR Studies	121
B.1	Introduction	121
B.1.1	IEEE First Benchmark Model (IEEE FBM)	121

Contents

Chapter 1

Introduction

1.1 Background and motivation

During the past 50 years, fixed series compensation has been successfully applied at the transmission level to improve the active power transfer and at the same time increase the power system's stability margin. Although various types of series compensation schemes based on power electronics have been proposed and adopted in actual installations, the use of fixed capacitor banks still remains the preferred choice, thanks to its simplicity and economic advantages. However, it has been reported that the presence of a series capacitor in the vicinity of a generation station presents the risk of poorly-damped oscillation below the system's rated frequency: a phenomenon known as SubSynchronous Resonance (SSR) [1]. SSR is a resonant condition where the generator system exchanges energy with the connecting electrical system below the subsynchronous frequency. SSR is not a new phenomenon and has been mainly observed in steam turbine and nuclear based generator system [2].

Up until 2009, it was generally believed that installation of fixed series compensation did not present any risk of SSR in case of large wind farms directly connected to the transmission grid. However, an eye opening scenario occurred in south Texas, where a wind farm experienced severe oscillations in the subsynchronous frequency range as a result of radial connection to a transmission line that was on series compensation [3] [4]. Being most of the wind turbines based on induction generators and power electronic devices (DFIG wind turbines), the phenomenon was initially attributed to self-excitation due to Induction Generator Effect (IGE) [5] [6]. Subsequent analysis has shown that the main cause of the interaction had to be attributed to the interaction between the controller of the wind turbine converters and the transmission line. In a DFIG wind turbine, the slip is controlled through the rotor-side converter. Under specific circumstances, dictated by the operating conditions and selected control parameters, the converter's control system can contribute to uncontrolled energy exchange between the generating system and the connecting grid. Therefore, investigation into the root causes of this phenomenon becomes crucial in understanding the mechanism that can lead to instability and thereby being able to propose effective mitigation methods.

Intensive research has been conducted in this field, trying to assess the potential risk of SSR

in DFIG-based wind farms when connected to fixed-series compensation. Some of these works evaluate the frequency response based on the transfer-function matrix of the system [7] [8]. In [8], a pole-zero mapping for the total radial system is used to evaluate the impact of different parameters such as controller gain and compensation level. Eigenvalue analysis of a DFIG based wind farm connected to series compensated transmission line can also be found in [9] [10] [11] [12]. However, in all these works the aggregated wind farm and the series compensated transmission line are represented with a high-order linearized state-space model. The disadvantage with this approach is that it can be bulky, as the entire system must be modeled as a single state-space representation, leading to the difficulty in properly assess the impact of the different parameters on the system stability. Furthermore, the entire mathematical model must be rebuilt in case of variations in the investigated system. Another approach is the impedance-based Nyquist stability analysis, presented in [13] [14]. However, in all these works only the impact of the inner current controller, level of series compensation and wind speed are considered, while all outer control loops are neglected in the analysis.

1.2 Aim of the thesis and main contribution

The aim of this thesis is to understand the root cause of the interaction due to SSR in wind turbines when connected to a series-compensated transmission line. The final goal is to better understand the SSR phenomenon in wind turbines and thereby be able to propose effective countermeasures. To the knowledge of the author, the main contribution of this thesis can be summarized as follows:

1. A detailed linearized mathematical model for the DFIG wind turbines connected to a series compensated transmission line has been derived and verified through time-domain simulations. The derived individual subsystem are used to perform frequency domain analysis to identify their behavior in the subsynchronous frequency range.
2. An impedance approach based on the Nyquist criterion has been proposed to identify the risk of SSCI in DFIG based wind farms when connected to a series-compensated transmission line. Individual subsystems constituting the DFIG farm and series compensated transmission line have been evaluated from a frequency-domain impedance approach under a variety of operating conditions and for different system controller parameters. The different factors that contribute to the risk of SSCI have been identified.
3. Two types of mitigation approaches have been developed and analyzed. The first approach involves impedance shaping through the variation of controller parameter whereas the second approach involves enhancement of system damping through the implementation of a damping controller in the rotor-side converter current controller loop.

1.3 Structure of the thesis

The thesis is organized into seven chapters. Chapter 1 presents the background, motivation and major contribution of the thesis. Chapter 2 of this thesis gives an overview of the various types of SSR and analysis methods employed to evaluate the risk of SSR both in classical generator units, like a steam-turbine, and in a wind turbine. An introduction to the different components and the controller of the DFIG wind turbine is presented in Chapter 3. In Chapter 4, the mathematical representation for the DFIG turbine and the series-compensated transmission line is derived. The derived mathematical model is then verified against a full-switching DFIG model simulated in PSCAD. Based on the results obtained from the derived model of Chapter 4, frequency-domain stability analysis is performed in Chapter 5. In this chapter, analytical conclusion based on frequency-domain analysis is performed to evaluate and identify system parameters and operating conditions that affect both the DFIG and transmission grid behavior. An impedance-based Nyquist criterion that employs the DFIG turbine impedance and the transmission grid admittance is introduced and utilized. Time-domain simulation performed in PSCAD/EMTDC is then used to verify the obtained analytical conclusions. Chapter 6 deals with the utilization of the DFIG controller to mitigate SSCI. Two mitigation approaches have been proposed. Both analytical and time-domain simulation are used to assess the impact of these techniques on the overall investigated system as well as on the aggregated DFIG model. Chapter 7 presents the conclusion and the future work.

Chapter 1. Introduction

Chapter 2

Subsynchronous Resonance in Power Systems

2.1 Introduction

Reinforcement of existing transmission lines to host the power from generator units is often needed [15]. With fast growth of renewable energy sources, like wind, solar, e.t.c, several challenges appear when dealing with the integration of the produced power into existing transmission system [16] [17]. Furthermore in many cases there might be the need for an upgrade of the transmission system in order to host the generated power, either by constructing new AC/DC system or by enhancing the transmission capacity of existing transmission line. Among the possible solutions, fixed series compensation is an economical solution to enhance the power transmission capabilities in existing grids [15]. However, series compensation is known to cause a risk for Subsynchronous Resonance (SSR) [17] [18] [19].

The first SSR incident was observed in Mohave project in south Nevada in 1970 [20]. A 750 MVA cross-compound turbine generator unit experienced shaft damages due to a ground fault that caused a 500 kV parallel transmission line to be switched out. This caused the turbine generator to be radially connected to a bus through a transmission line that was on series compensation [2]. Following the first incident in 1970 and a similar occurrence one year later, an IEEE working group was to investigate the cause of the damage [1]. The Mohave incident was an eye opener to the problem of SSR, but further investigation considering other turbine generation projects gave a reflection on how complex the problem can be [2]. An example is the Navajo project, which consisted of three tandem-compound turbine generator with a generation capacity of 750 MW and a 2900 km/500 kV transmission line [2] [21]. With the exception of short tie lines, all transmission lines were on series compensation. The initial analysis showed that the Navajo project would have faced a severe SSR problem. After a series of analysis [21], the project continued with the same level of series compensation but with additional countermeasures to reduce the risk of SSR [2].

The likelihood of SSR in renewable generator units, such as large wind farms, was not considered up until 2009. In 2009, an incident in southern Texas occurred, where the Gorilla-Zorilla

wind farm became radially connected to a series-compensated transmission line due to a fault on a parallel line [3] [22]. As most of the wind turbines are based on induction generator with power electronic devices, the phenomenon is in general attributed to self-excitation of the system due IGE or control system interaction [23] [19] [24].

In this chapter, a general introduction of the problem of SSR in power system together with the classification of the different types of SSR will be given. The analysis method to assess the risk of SSR will be presented in Section 2.3 with more details to be included in the chapters to follow. In Section 2.4, SSR in classical generator unit is addressed while Section 2.5 will cover SSR in wind generation units.

2.2 SSR definition and classification

In accordance with the definition of IEEE, subsynchronous resonance (SSR) is *an electrical power system condition where the electrical network exchanges energy with turbine generator at one or more of the natural frequencies of the combined system below the synchronous frequency of the system following a disturbance from an equilibrium point* [1].

There exist three types of classical SSR, namely: Induction Generator Effect (IGE), Torsional Interaction (TI), and Torque Amplification (TA). Based on the time required for the oscillation to build up, these can be further classified into groups: steady-state and transient SSR. The steady-state SSR comprises of IGE and TI. Since this kind of SSR typically build up slowly, they might be considered as small signal conditions (at least initially) and can be analyzed using linear model representation. The transient SSR includes TA, which is an SSR that occurs following a large system disturbance such as system faults. This is therefore a fast phenomenon that can reach dangerous level within a short period of time.

Induction Generator Effect (IGE): IGE is a pure electrical phenomenon caused by self excitation of the electrical system. The subsynchronous current that flows in the armature of the generator creates a Magnetic Motive Force (MMF) that rotates slower than the generator's MMF. This causes the synchronous generator to act as an induction generator in the subsynchronous frequency range. As a result, the resistance of the rotor as viewed from the terminal of the generator, at subsynchronous current, is negative [25] [26]. If the magnitude of the negative rotor resistance of the generator exceeds the sum of the armature and network resistance around the natural frequency of the network, the system presents an overall negative resistance against the subsynchronous current. This results in a self-excitation that leads to a growing subsynchronous current. IGE is a pure electrical phenomenon that does not involve the mechanical system of the generator unit.

Torsional Interaction (TI). TI is a electro-mechanical phenomenon that results in an energy exchange between the electrical system and the mechanical shaft of the generator unit. TI occurs when the electrical torque setup by the subsynchronous current component is electrical close to the natural frequency of the generator shaft. When this happens the rotor starts to oscillate around the rated speed with a frequency equal to the perturbation frequency, f_{per} . Besides its fundamental component, the induced terminal voltage will be constituted by two additional

2.3. SSR analysis and investigation methods

frequency components, a subsynchronous ($f_s - f_{per}$) and a supersynchronous components ($f_s + f_{per}$) [27]. If the generated torque components exceeds the inherent overall damping torque of the system, excitation occurs. During the planning stage for series compensation, the resonance frequency for the system is chosen so that it lies in the subsynchronous frequency range. For a loss-less line, this resonance frequency can be calculated as [25]:

$$\omega_n = \sqrt{\frac{1}{LC}} = \omega_B \sqrt{\frac{X_C}{X_L}} \quad (2.1)$$

where ω_B is the base frequency in rad/sec while X_C and X_L are the equivalent per-unit (pu) inductive and capacitive reactance, respectively. On the other hand, the natural frequencies (normally referred to as oscillation modes) of the mechanical system always lies in the subsynchronous range. For an SSR to occur, the natural frequency of the generator shaft system must coincide or is in the vicinity of the complementary frequency and at the same time the total damping of the system around this frequency is zero or negative. Meaning if there exist a condition where the frequencies coincides and the total damping of the system at that frequency is zero or negative, any exchange of energy will not die out but instead is sustained or growing through time. TI interaction manifests itself in generator units where the inertia of the turbine is in the same order of magnitude as the inertia of the generator (rotor), such as thermal power plants or nuclear power plants [28]. In a hydro generator station where the inertia of the generator is higher than the turbine inertia, any oscillation that are triggered in the turbine unit does not get reflected on to the rotor, which breaks the cycle and as a result minimizing the interaction that could possibly occur with the grid resonance.

Torque Amplification (TA). TA also known as Transient Torque is a phenomenon that occurs when the electrical resonance presented by the electrical system is close to one or more natural torsional frequencies of the mechanical system, following a disturbance from an equilibrium point. Following a disturbance, a high current level that tends to oscillate at the system's natural frequency (f_n), flows in the network. This charges up the capacitor which in turn discharges through the network into the generator. The resulting high torque is reflected on the mechanical system. If the complement of electrical natural frequency is close to one/more natural torsional frequency of the mechanical system, with the total damping torque begin negative or zero resulting in a growing/sustained oscillation. Unlike IGE and TI, the growing rate of TA is high and oscillating shaft torque can reach damaging level within a small amount of time [2]. In addition, as the non-linearity of the system comes into play, analysis using conventional linearized model will not feasible. As a result, analysis for TA must be performed using time-domain simulation program like EMTDC/PSCAD where the system non-linearity is well represented.

2.3 SSR analysis and investigation methods

Through the years different analytical tools have been developed to identify and analyze the risk for SSR. The most commonly used are the Frequency Scanning Method (FSM), Eigenvalue analysis and EMTP analysis. Eigenvalue analysis and FSM are only applicable for assessing the risk for steady-state SSR. On the other hand, EMTP, which takes into consideration the non-linear property of the different components involved, is used for assessing the risk for TA.

2.3.1 Frequency Scanning Method

FSM is a technique widely used to preliminary asses the risk of SSR in a system [25]. The principle is to compute the frequency-dependent equivalent resistance and reactance of the network, as seen from behind the generator's stator. If there exists an occurrence where the inductance goes to zero and the resistance is negative for the same frequency, a sustained oscillation persists at that frequency as a result of IGE. The advantage with this method is that it gives a quick check for the risk of instability due to SSR [28]. FSM is also a powerful tool to asses the risk of TI [25]. If there exists a network series resonance or a reactance minimum close to one of the shaft natural frequencies, it is an indication that there might be a risk for TI, although this needs to be verified with other analytical approaches. Damping torque analysis, which is an analytical method involving the computation of the damping torque presented by the electrical system (i.e. generator and network) and the mechanical system, is another approach used to analyze TI (as mentioned in section 2.4).

2.3.2 Eigenvalue analysis

Eigenvalue analysis requires the entire system to be defined in terms of linear differential equation. Based on the equations, the state space form is obtained for the entire system as:

$$\dot{x} = \mathbf{A}x + \mathbf{B}u \quad (2.2)$$

the eigenvalues can be obtained as a solution of the matrix equation below

$$\det[\lambda\mathbf{I} - \mathbf{A}] = 0 \quad (2.3)$$

Eigenvalue analysis has an advantage over FSM as it provides information about the oscillatory frequencies as well as the damping for these frequencies. The downside with eigenvalue analysis is that it can be bulky, especially for large system, as a single state-space model of the entire system is needed to perform the analysis.

2.3.3 Time domain simulations

PSCAD/EMTDC is a program used for numerical computation of system differential equation in time domain. The benefit it provides is that we are able to do a full nonlinear modeling of the system machine and other devices. Another important note is that TA can only be analyzed using EMTP approach since the non linearity of the system comes into play when studying this phenomenon. In this report, we also use PSCAD/EMTDC analysis to verify the conclusion reached using analytical or frequency based methods.

2.3.4 Input admittance approach

Various application have employed the concept of input admittance to evaluate the stability of a system and possible interaction that may exist, as in [29] [30] [14] [31] to mention a few.

2.4. SSR in classical generator units

Although, the mentioned works differ a bit in their analysis approach, they all share a core theory relating to the passivity of the system for a range of frequencies. It is stated in [32] that a Single Input Single Output (SISO) system ($F(s)$), represented with a transfer function $G(s)$ and a feedback $H(s)$ (see Fig. 2.1), is passive if and only if the closed-loop transfer function satisfies (2.4),

$$\operatorname{Re}[F(j\omega)] \geq 0, \forall \omega \geq 0 \quad (2.4)$$

where $F(j\omega)$ is the closed-loop transfer function. Meaning, for a system with a positive real part in a specific range of frequencies, if subjected to an oscillation within the same range, is immune to instability if it is able to dissipate the energy [29]. This holds provided that we are looking at the closed-loop system. In addition, the input admittance in corresponds with the passivity can also be used to evaluate the stability of closed-loop system, $F(s)$, by observing the individual transfer functions $G(s)$ and $H(s)$ [32]. For the interested reader, further details can be found in [32] [33] [34].

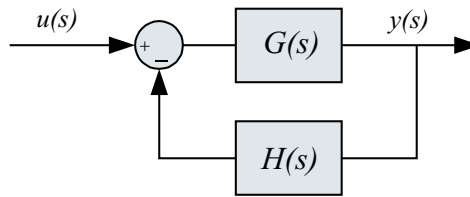


Fig. 2.1 Block diagram of a SISO system with feedback

Another approach for evaluation of system stability using input admittance is by employing the impedance or admittance transfer function in the same manner as above but instead of considering the closed-loop transfer function, we applying the Nyquist criterion on the open-loop transfer function [14]. This approach is further discussed in detail in chapter 5.

2.4 SSR in classical generator units

In 1970, The Mohave station located in southern Texas, experienced shaft damage when the station became radially connected to a transmission line on series compensation. A similar incident in 1971 occurred, which lead to the manual shut down of the station. Fig. 2.2, shows the power system of the station at the time of the incident. Due to a fault, the 500 kV transmission line was switched out by opening the circuit breaker. This caused the Mohave station to be radially connected to the Lugo bus through a transmission line that was on series compensation. The phenomenon observed included excessive field current, alarm for high vibration, field ground and negative-sequence currents as well as flickering lights in the control room, which continued for two minutes. Post incident investigations showed that the shaft section in the high pressure turbine experienced extreme heating as a result of cyclic torsional stress [2]. After thorough investigation, it was understood that the incident in Mohave was due to an interaction and exchange of energy between the mechanical system of the turbine generator and the series capacitor of the transmission line (what we refer today as TI) [2].

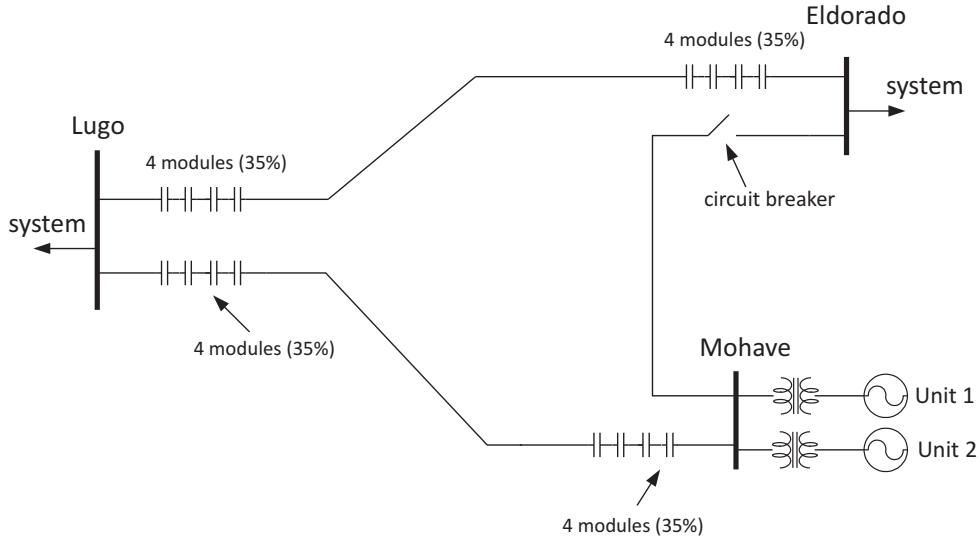


Fig. 2.2 Single-line diagram of the power system around Mohave station.

Following the two incident that occurred in Mohave, an IEEE working group for subsynchronous developed the IEEE first benchmark Model (IEEE FBM) and the IEEE Second Benchmark Model (IEEE SBM) for use in computer program simulation and development to investigate the risk of SSR. The IEEE FBM system consists of a synchronous generator connected to an infinite bus through a series compensated transmission line. Fig. 2.3 shows the layout of the IEEE FBM, while the detailed modeling and parameters can be found in the Appendix B.

Let us consider a steam turbine generator system with a number of pressure stages as shown in Fig. 2.4. The parameters for the turbine model are taken from the IEEE First Benchmark Model (IEEE FBM) that can be found in the Appendix B. The mechanical system presents five modes with characteristics frequencies 15.71 Hz, 20.205 Hz, 25.547 Hz, 32.28 Hz, and 47.456 Hz. When a mode is excited, the generator rotor will oscillate with a frequency (f_m), which is reflected on the generator voltage having both subsynchronous component ($f_0 - f_m$) and supersynchronous component ($f_0 + f_m$), where f_0 is the system frequency (see Fig. 2.5). The electrical torque in the dq frame can be written as

$$T_e = \text{Im} \left[\dot{i}_{dq} \left(\underline{\psi}_{dq} \right)^* \right] = i_q \psi_d - i_d \psi_q \quad (2.5)$$

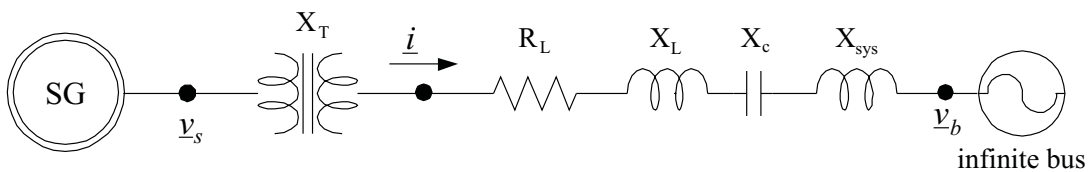


Fig. 2.3 Single-line diagram of a synchronous generator connected to an infinite bus through a series compensated transmission line.

2.4. SSR in classical generator units

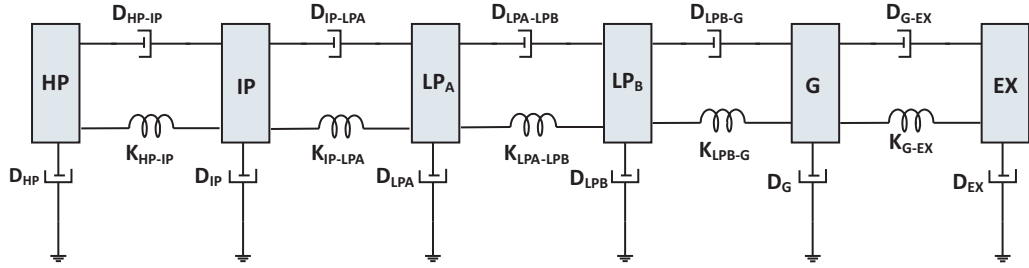


Fig. 2.4 six mass mechanical system representation of a turbine generation unit.

where i_{dq} is the armature current and ψ_{dq} is the stator flux. For small variation around an operating point, the linearized equation are

$$\Delta T_e = i_{q0}\Delta\psi_d + \psi_{d0}\Delta i_q - i_{d0}\Delta\psi_q - \psi_{q0}\Delta i_d \quad (2.6)$$

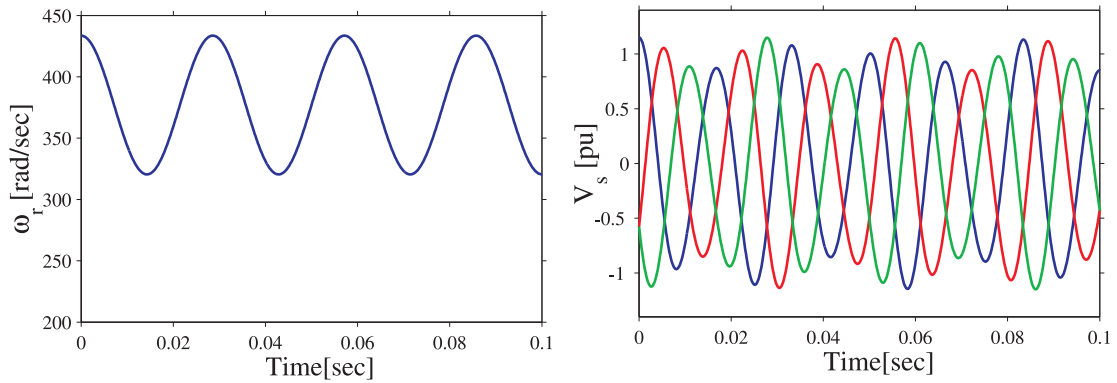


Fig. 2.5 Oscillation on rotor speed (ω_r) (left plot). Terminal voltage due to oscillation on rotor speed (right plot)

Let us consider the transfer function from $\Delta\omega_r$ to ΔT_e as shown in Fig.2.6

$$G_e(s) = \frac{\Delta T_e}{\Delta\omega_r}(s) \quad (2.7)$$

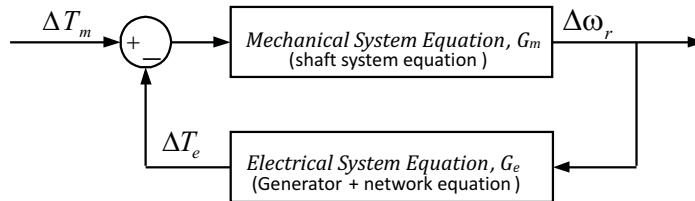


Fig. 2.6 Block diagram showing the interaction between mechanical and electrical system.

To get the frequency response of the system, the Laplace variable s in (2.7) is replaced with $j\omega_k$ where ω_k is the frequency of interest. The frequency response can be split into its real and

imaginary part as

$$G_e(j\omega_k) = \text{Re}[G_e(j\omega_k)] + j\text{Im}[G_e(j\omega_k)] = \Delta T_{De}(j\omega_k) - \frac{\omega_B}{\omega_k} \Delta T_{Se}(j\omega_k) \quad (2.8)$$

where ΔT_{De} and ΔT_{Se} are referred to as electrical damping and synchronization torque respectively [28]. The same definition holds for the mechanical damping (ΔT_{Dm}) and synchronization torque (ΔT_{Sm}). The inherent damping torque of the electrical system under consideration, which includes the generator and the series compensated transmission line, can thus be obtained by taking the real part of the transfer function from rotor speed ($\Delta\omega_G$) to electrical torque (ΔT_e) as

$$T_{De}(j\omega_m) = \text{Re} \left[\frac{\Delta T_e}{\Delta\omega_r}(j\omega_m) \right] \quad (2.9)$$

The extracted electrical damping torque according to (2.9) is depicted in right plot of Fig. 2.7. Similarly the mechanical damping of the system is depicted in the left plot of the same figure. SSR due to TI can occur in a power system if the electrical resonance of the system coincides or is electrically close to one of the natural frequencies of the generator-turbine system provided that the total damping of the system is zero or negative as described in (2.10). Observing the left and the right plot of Fig. 2.7, the total damping torque calculated based on (2.10) is negative for the second mode (20.205 Hz), which indicates a high risk of TI, if an oscillation at this specific frequency is triggered.

$$\Delta T_D(j\omega_m) = \Delta T_{De}(j\omega_m) + \Delta T_{Dm}(j\omega_m) \leq 0 \quad (2.10)$$

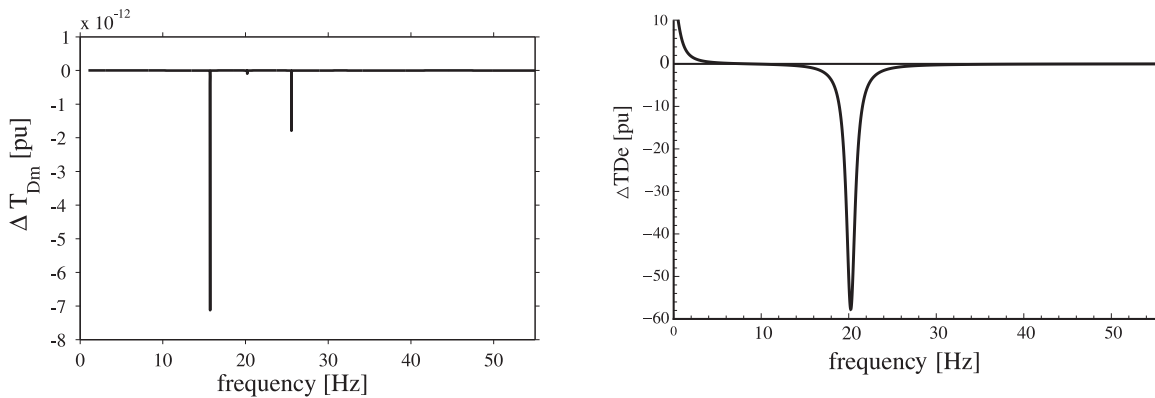


Fig. 2.7 Mechanical damping torque (*left plot*) and Electrical damping torque for 38% series compensation(*right plot*).

For investigation of SSR due to IGE, it is necessary to evaluate the subsynchronous rotating flux established by the subsynchronous current; in this case the synchronous generator inherits the behavior of an induction generator with a slip described by:

$$s_{ssr} = \frac{f_{sub} - f_r}{f_{sub}} \quad (2.11)$$

2.5. SSR in wind generator units

where f_{sub} is the frequency of subsynchronous flux and f_r is the frequency of the rotor flux. Accordingly, the equivalent rotor resistance can be described as:

$$R_{eq}^{sub} = \frac{R_r}{s_{SSR}} \quad (2.12)$$

As the speed of the subsynchronous component of the stator flux is less than the rotor flux vector that rotates at synchronous speed, the slip becomes negative that in turn causes the equivalent resistance to be negative. To assess the risk of IGE, the impedance of a synchronous generator for subsynchronous frequencies is plotted in Fig. 2.8. As it can be observed from the plot, due to the fictitious slip resulting from the presence of the subsynchronous current, the synchronous generator behaves like an induction generator with a negative rotor resistance. As a result, the impedance of the synchronous generator for the entire subsynchronous frequency range becomes negative. The problem of IGE prevails if and only if the total resistance of the system, as viewed from the rotor, becomes negative. That is, if the sum of the generator's resistance and network resistance is negative. IGE can occur in all types of generator units, including hydro generator units. On the contrary, if we observe Fig. 2.8, the negative resistance of the synchronous generator can possibly exceed the resistance of the network for higher frequency range. For the system resonance to occur within this range, the level of series compensation should be over 80% compensation. This level of compensation in reality does not exist due to thermal issues [2].

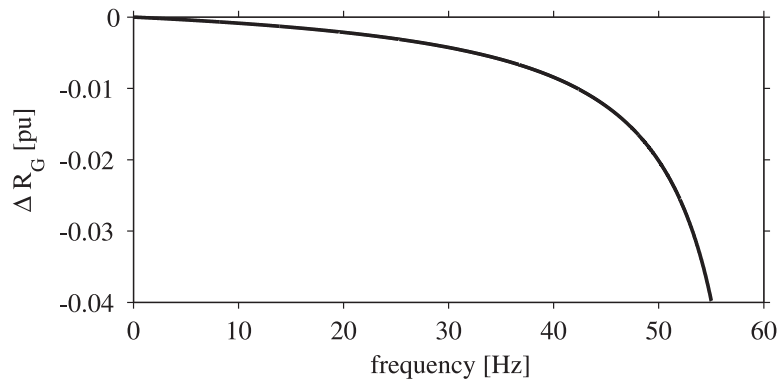


Fig. 2.8 Synchronous generator resistance for subsynchronous frequency range.

2.5 SSR in wind generator units

Renewable generator unit is a term given to an energy generation unit where the sources of energy are available abundantly in addition to being re-usable, such as: wind, hydro and solar energy. To minimize the impact of our energy demand on the environment, actual trends are favoring this kind of energy sources. But the shift is facing various challenges. For instance, in case of wind energy, large scale wind farms are located either offshore or onshore, at a remote locations, away from the load centers. One of the challenges is to transport the energy produced.

The focus of renewable energy source in this thesis is wind. Wind turbines typically can be divided in three types. These are the Fixed-Speed Induction Generator (FSIG) wind turbine, the Full-Power Converter (FPC) based wind turbine and the Doubly-Fed Induction Generator (DFIG) wind turbine. In the sections to follow, the different types of wind turbine together with the associated risk for SSR will be discussed

2.5.1 SSR in fixed speed wind turbine

A FSIG wind turbine mainly consists of a Squirrel Cage Induction Generator (SCIG) that is directly connected to the grid through a transformer, as depicted in Fig. 2.9. A SCIG consists of two windings, a stator winding and a rotor winding. The stator winding provides excitation and at the same time carries the generated armature current. The rotor in SCIG is short circuited and serves the purpose of carrying the induced current. A SCIG presents several advantages over other types of wind turbines, such as robustness, mechanical simplicity and relatively low price [35]. The major downside with this sort of machine, being inductive in nature, require reactive magnetizing current [16]. As a result, to improve the power factor of the generated power at the connection point, a shunt-connected capacitor bank is added to the system.

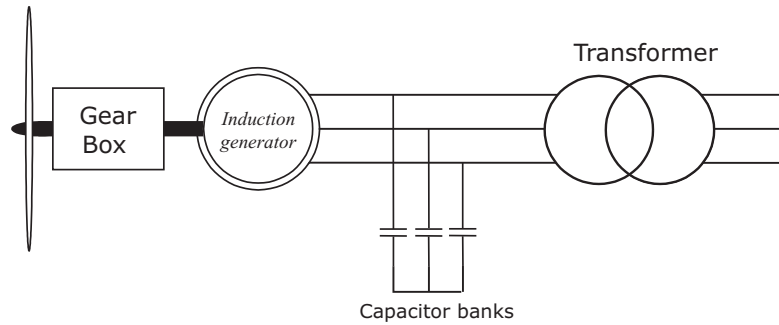


Fig. 2.9 Single-line diagram of a fixed-speed wind turbine.

If we observe the equivalent circuit diagram of an induction machine, shown in Fig. 2.10, the rotor resistance is negative when the induction machine is operated as a generator. This is due to the negative slip as also investigated in the previous section. Expressing the equations governing the IG in the rotating dq frame, the stator and rotor voltages in pu are expressed as:

$$\begin{aligned} v_s &= R_s i_s + j \frac{\omega_s}{\omega_B} \underline{\psi}_s + \frac{1}{\omega_B} \frac{d\underline{\psi}_s}{dt} \\ v_r &= R_r i_r + j \frac{\omega_2}{\omega_B} \underline{\psi}_r + \frac{1}{\omega_B} \frac{d\underline{\psi}_r}{dt} \end{aligned} \quad (2.13)$$

where R_s and R_r represent the pu stator and rotor resistances, respectively. The term ω_2 is the slip angular frequency, which is equivalent to $\omega_s - \omega_r$ with ω_r representing the rotor angular frequency. The term ω_B is the base angular frequency, which is equivalent to the synchronous angular frequency here expressed as ω_s . $\underline{\psi}_s$ and $\underline{\psi}_r$ are the stator and rotor fluxes, respectively, which are further expressed in terms of currents and reactances as:

2.5. SSR in wind generator units

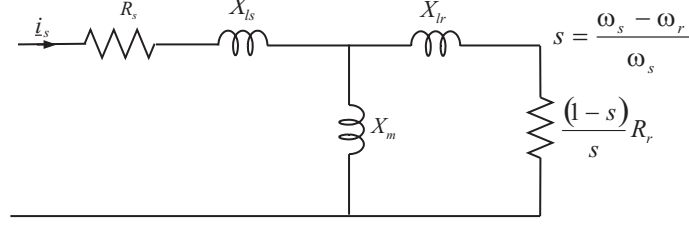


Fig. 2.10 Equivalent circuit of induction machine.

$$\begin{aligned}\underline{\psi}_s &= \frac{X_{ls}}{\omega_B} \underline{i}_s + \frac{X_m}{\omega_B} (\underline{i}_s + \underline{i}_r) = \frac{X_{ss}}{\omega_B} \underline{i}_s + \frac{X_m}{\omega_B} \underline{i}_r \\ \underline{\psi}_r &= \frac{X_{lr}}{\omega_B} \underline{i}_r + \frac{X_m}{\omega_B} (\underline{i}_s + \underline{i}_r) = \frac{X_{rr}}{\omega_B} \underline{i}_r + \frac{X_m}{\omega_B} \underline{i}_s\end{aligned}\quad (2.14)$$

where the different terms in the equation above have the meaning as in Fig.2.10. Breaking (2.13) into components and replacing the currents with the flux expressions of (2.14), the state-space equation of the system can be derived as

$$\begin{aligned}\dot{x}_G &= \mathbf{A}_G x_G + \mathbf{B}_G \mathbf{V}_s \\ \mathbf{y}_G &= \mathbf{C}_G x_G\end{aligned}\quad (2.15)$$

where

$$\begin{aligned}\mathbf{V}_s &= \begin{bmatrix} v_{sd} \\ v_{sq} \end{bmatrix}, \quad \mathbf{y}_G = \begin{bmatrix} i_{sd} \\ i_{sq} \end{bmatrix} \\ x_G &= [\psi_{sd} \quad \psi_{sq} \quad \psi_{rd} \quad \psi_{rq}]^T\end{aligned}\quad (2.16)$$

$$\mathbf{A}_G = \begin{bmatrix} \frac{-R_s X_{rr} \omega_B}{D} & \omega_s & \frac{R_s X_m \omega_B}{D} & 0 \\ \omega_s & \frac{-R_s X_{rr} \omega_B}{D} & 0 & \frac{R_s X_m \omega_B}{D} \\ \frac{R_r X_m \omega_B}{D} & 0 & \frac{-R_r X_{ss} \omega_B}{D} & s \omega_s \\ 0 & \frac{R_r X_m \omega_B}{D} & -s \omega_s & \frac{-R_r X_{ss} \omega_B}{D} \end{bmatrix}$$

$$D = \frac{X_{ss} X_{rr} - X_m^2}{\omega_B}$$

$$\mathbf{B}_G = \begin{bmatrix} \omega_B & 0 \\ 0 & \omega_B \\ 0 & 0 \\ 0 & 0 \end{bmatrix}, \quad \mathbf{C}_G = \begin{bmatrix} \frac{X_{rr}}{D} & 0 & \frac{-X_m}{D} & 0 \\ 0 & \frac{X_{rr}}{D} & 0 & \frac{-X_m}{D} \end{bmatrix}$$

Chapter 2. Subsynchronous Resonance in Power Systems

Taking the stator voltage as input and stator current as output, the admittance matrix in the dq frame can be expressed as

$$\begin{bmatrix} i_{sd}(s) \\ i_{sq}(s) \end{bmatrix} = \begin{bmatrix} Y_{Gdd}(s) & Y_{Gdq}(s) \\ Y_{Gqd}(s) & Y_{Gqq}(s) \end{bmatrix} \begin{bmatrix} v_{sd}(s) \\ v_{sq}(s) \end{bmatrix} \quad (2.17)$$

where s represent the Laplace variable. Note that in a SCIG, the rotor is short circuited, therefore the rotor voltage (v_r) is equal to zero. Being the admittance matrix symmetric, the phase admittance can be extracted from the dq admittance matrix as [36]:

$$Y_G(s) = Y_{Gdd}(s) + jY_{Gqd}(s) \quad (2.18)$$

The phase impedance for the generator is obtained from the phase admittance as

$$Z_G(s) = \frac{1}{Y_G(s)} = \frac{1}{Y_{Gdd}(s) + jY_{Gqd}(s)} \quad (2.19)$$

Replacing the Laplace variable s with $j\omega$ for steady-state representation, the real and imaginary part of $Z_G(j\omega)$ as a function of frequency can be plotted as shown in Fig. 2.11. Parameters used can be found in Appendix B, Table. B.5. The real part of the impedance is negative for the entire subsynchronous range while the imaginary part of the generator impedance is mainly positive, due to the inductive nature of both the stator and rotor circuits. The fact that the resistance is negative in the subsynchronous range only indicates potential risk for IGE. For IGE to exist, the total resistance of the generator in combination with network should become zero or negative. Comparing Fig. 2.11 with Fig. 2.8, it can be observed that the induction generator presents a tenth of order higher negative resistance as compared with the synchronous generator. This increases the probability of the grid impedance begin lower than the generators impedance over a wider frequency range, which indirectly increases the risk of IGE.

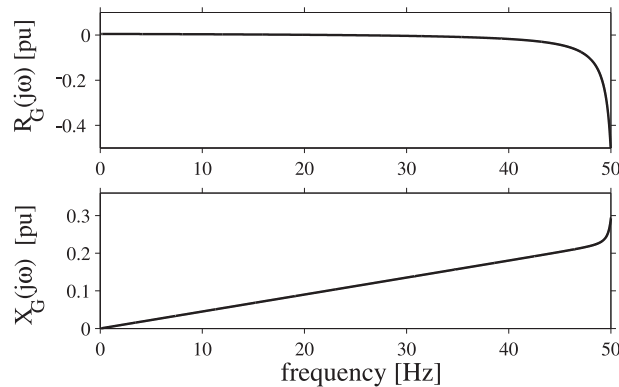


Fig. 2.11 Impedance of an induction generator in the synchronous frequency range.

To Evaluate the total resistance of an induction generator in series with a series-compensated transmission line, the transmission line model should be included. For this a rotating reference

2.5. SSR in wind generator units

frame that is fixed to the infinite bus is considered (see Fig. 2.3), which is represented with the capital letters DQ . The terminal voltage \underline{v}_s and \underline{v}_c in the DQ frame are expressed as

$$\begin{aligned}\underline{v}_s^{(DQ)} &= (R_L + jX_L)\dot{i}_s^{(DQ)} + \frac{X_L}{\omega_B} \frac{di_s^{(DQ)}}{dt} + \underline{v}_c^{(DQ)} + \underline{v}_b^{(DQ)} \\ \frac{d\underline{v}_c^{(DQ)}}{dt} &= -j\omega_s \underline{v}_c^{(DQ)} + \omega_B X_C \dot{i}_s^{(DQ)}\end{aligned}\quad (2.20)$$

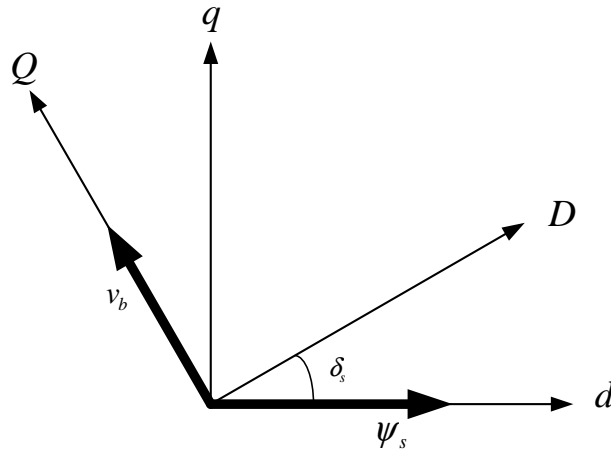


Fig. 2.12 Relation between dq and DQ frame.

The state-space equation for the network then can be expressed as

$$\frac{d}{dt} \begin{bmatrix} v_{c,D} \\ v_{c,Q} \end{bmatrix} = \mathbf{A}_N \begin{bmatrix} v_{c,D} \\ v_{c,Q} \end{bmatrix} + \mathbf{B}_N \begin{bmatrix} i_D \\ i_Q \end{bmatrix}\quad (2.21)$$

with

$$\begin{aligned}\mathbf{A}_N &= \begin{bmatrix} 0 & \omega_s \\ -\omega_s & 0 \end{bmatrix}, \quad \mathbf{B}_N = \begin{bmatrix} \omega_B X_C & 0 \\ 0 & \omega_B X_C \end{bmatrix} \\ C_N &= \begin{bmatrix} 1 & 0 \\ 0 & 1 \end{bmatrix}\end{aligned}$$

Expressing the terminal voltage (\underline{v}_s) in generator dq -reference frame

$$\underline{v}_s^{(dq)} = (R_L + jX_L)\dot{i}_s^{(dq)} + \frac{X_L}{\omega_B} \frac{di_s^{(dq)}}{dt} + e^{j\delta_s} \left(\underline{v}_c^{(DQ)} + \underline{e}_b^{(DQ)} \right)\quad (2.22)$$

where δ_s is as described in Fig.2.12. Since the terms in C_G are all constant and $\begin{bmatrix} i_{sd} \\ i_{sq} \end{bmatrix} = C_G x_G$, then the derivative of the current that appears in (2.22) can be expressed as

$$\frac{d}{dt} \begin{bmatrix} i_{sd} \\ i_{sq} \end{bmatrix} = C_G \dot{x}_G\quad (2.23)$$

Chapter 2. Subsynchronous Resonance in Power Systems

Substituting (2.23) into (2.22) followed by mathematical manipulation to express the equation in terms of matrices, the terminal voltage can be expressed as

$$\mathbf{V}_s = [\mathbf{F}]_G [\mathbf{G}]_G x_G + [\mathbf{F}]_G [\mathbf{P}]_G \left\{ \mathbf{Y}_N + \begin{bmatrix} 0 \\ \mathbf{V}_b \end{bmatrix} \right\} \quad (2.24)$$

with

$$\begin{aligned} [\mathbf{F}]_G &= \left[\mathbf{I}_2 - \frac{\mathbf{X}_L}{\omega_B} [\mathbf{C}_G] [\mathbf{B}_G] \right]^{-1} \\ [\mathbf{G}]_G &= [\mathbf{Z}_L] [\mathbf{C}_G] + \frac{\mathbf{X}_L}{\omega_B} [\mathbf{C}_G] [\mathbf{A}_G] \\ \mathbf{V}_s &= \begin{bmatrix} v_{s,d} \\ v_{s,q} \end{bmatrix} \end{aligned} \quad (2.25)$$

where \mathbf{I}_2 , $[\mathbf{Z}_L]$ and $[\mathbf{Y}_N]$ are

$$\begin{aligned} [\mathbf{Z}_L] &= \begin{bmatrix} \mathbf{R}_L & -\omega_s \mathbf{X}_L \\ \omega_s \mathbf{X}_L & \mathbf{R}_L \end{bmatrix}, \mathbf{I}_2 = \begin{bmatrix} 1 & 0 \\ 0 & 1 \end{bmatrix} \\ [\mathbf{Y}_N] &= \begin{bmatrix} v_{c,D} \\ v_{c,Q} \end{bmatrix} = [\mathbf{C}_N] \begin{bmatrix} v_{c,D} \\ v_{c,Q} \end{bmatrix} \end{aligned}$$

Matrix $[\mathbf{P}]_G$ accounts for the transformation matrix between the network reference frame and the generator reference frame and is expressed as

$$[\mathbf{P}]_G = \begin{bmatrix} \cos \delta_s & -\sin \delta_s \\ \sin \delta_s & \cos \delta_s \end{bmatrix}, \quad (2.26)$$

Now taking the terminal voltage expression in (2.24) and substituting it in the generator state-space equation (2.15) together with the network equation (2.21), the combined state-space for the generator and the transmission line can be expressed as [26]:

$$\dot{\mathbf{X}}'_G = \mathbf{A}'_G \mathbf{X}'_G + \mathbf{B}'_G E_b \quad (2.27)$$

where

$$\begin{aligned} \mathbf{A}'_G &= \begin{bmatrix} \mathbf{A}_G + \mathbf{B}_G [\mathbf{F}]_G [\mathbf{G}] & \mathbf{B}_G [\mathbf{F}]_G [\mathbf{P}]_G [\mathbf{C}_N] \\ \mathbf{B}_N [\mathbf{P}]_G^T \mathbf{C}_G & \mathbf{A}_N \end{bmatrix} \\ \mathbf{B}'_G &= \mathbf{B}_G [\mathbf{F}]_G [\mathbf{P}]_G \begin{bmatrix} 0 \\ 1 \end{bmatrix} \end{aligned} \quad (2.28)$$

The new state variables \mathbf{X}'_G are

$$\mathbf{X}_G = \left[\psi_{sd} \quad \psi_{sq} \quad \psi_{rd} \quad \psi_{rq} \quad e_{c,D} \quad e_{c,Q} \right]^T \quad (2.29)$$

2.5. SSR in wind generator units

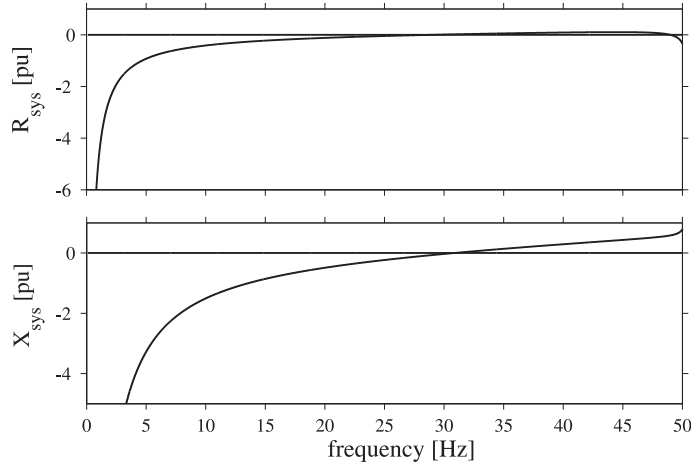


Fig. 2.13 Impedance of Induction generator radially connected to a series compensated network. Resistance in pu (*upper plot*), Reactance in pu (*lower plot*), $X_C = 0.35pu$

The induction generator's rotor speed (ω_r) expressed in terms of the slip (s) is considered as input during linearization. Extracting the phase impedance from (2.17) to (2.19), the total impedance for the generator in series with a transmission line on series compensation can be obtained. Fig. 2.13 shows the total impedance of a radial connection between an induction generator and a transmission line with 35% series compensation. From the figure, we can observe that the total resistance of the system is negative at the resonance frequency, which is a clear indication of risk for IGE. To summarize, fixed speed induction generator present a risk for IGE at a realistic level of compensation. This is attributed to the negative resistance that the generator presents towards the transmission network.

To evaluate the risk of torsional interaction, the electrical damping torque for the electrical system and the mechanical damping torque of the mechanical system is compared. The drive train for the fixed-speed wind turbine is modeled using the two-mass system shown in Fig. 2.14. The set of equation that define the dynamics of the mechanical drive train is expressed as:

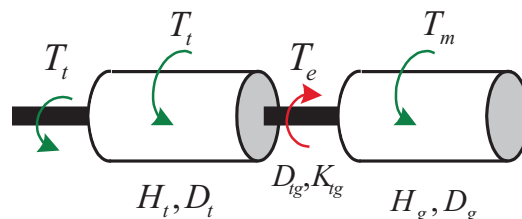


Fig. 2.14 Two mass representation for the mechanical system of an induction generation unit.

$$\begin{aligned}
 \frac{1}{\omega_B} \frac{d\delta_t}{dt} &= \omega_t \\
 2H_t \frac{d\omega_t}{dt} &= T_m - D_t \omega_t - D_{tg} (\omega_t - \omega_g) - K_{tg} (\delta_t - \delta_g) \\
 \frac{1}{\omega_B} \frac{d\delta_g}{dt} &= \omega_g \\
 2H_g \frac{d\omega_g}{dt} &= T_e - D_g \omega_g - D_{tg} (\omega_g - \omega_t) - K_{tg} (\delta_g - \delta_t)
 \end{aligned} \tag{2.30}$$

The mechanical damping torque is then calculated using the transfer function from the rotor speed to mechanical torque as:

$$T_{Dm}(s) = \text{Re} \left[\frac{\Delta T_m}{\Delta \omega_g}(s) \right] \tag{2.31}$$

Plotting the electrical damping torque against the mechanical damping torque as in Fig. 2.15 shows that the mechanical mode for a wind turbine occurs at a very low frequency, i.e. in the range 2-9 Hz. It is also known that when the various rotating components, like the gear box and the blades for instance, are lumped into a two-mass model, our view is limited when it comes to the different mechanical modes that might exist. In [37], where a five-mass model for the drive train is considered, the dominate frequency appeared at 2.5 Hz, i.e. still occurs at low frequencies. As a result, for an interaction between the mechanical and electrical system to occur, the negative electrical damping torque needs to occur at the complementary frequency of $f_o - f_m$, i.e. comes close to the synchronous frequency. The network resonance frequency occurs very close to the synchronous frequency if the level of series compensation is very high (about 90% compensation), which is not realistic in practical installation. In conclusion, the likelihood of SSR due to TI in wind farm is very low and as a result will not be further discussed in this work.

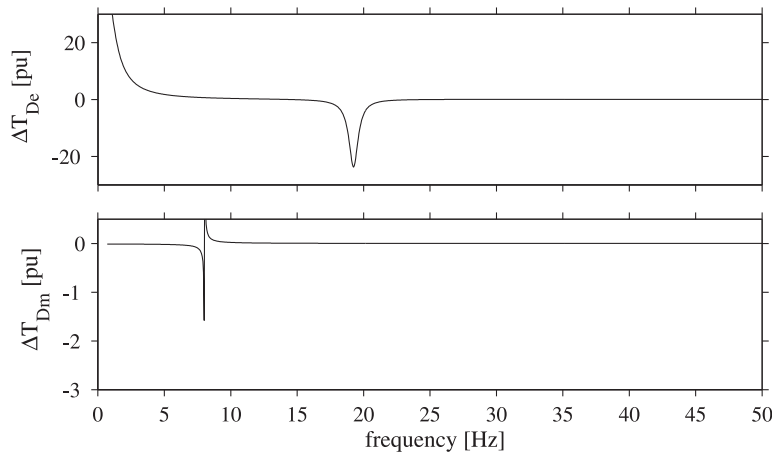


Fig. 2.15 Electrical damping torque (*upper plot*) and mechanical damping torque (*lower plot*) for induction generator connected to IEEE FBM network, $X_c = 0.35 pu$

2.5.2 SSR in doubly fed induction generator

Attention concerning SSR in variable-speed wind turbines came into focus following the incident in south Texas in 2009. Fig. 2.16, shows the single-line diagram of the transmission network topology around the Zorilla Gulf wind farm in south Texas. Two wind farms with installed capacity of 93.6 MW and 96 MW, respectively, were connected to the Ajo station [22]. The 345 kV transmission from Ajo to Rio Hondo has two stages of series compensation (17% and 33%) located at the Rio Hondo station, with both stages typically in service. During the incident, a single-line to ground fault occurred on the transmission line that goes from Nelson to Ajo. To clear the fault the circuit breaker was opened, which caused the Zorilla Gulf wind farm to be radially connected to the series-compensated line between Ajo and Rio Hondo. The system voltage oscillation started to build up with a peak voltage reaching up to 2 pu. This caused the shunt reactor at Ajo and the transmission line from Ajo to Rio Hondo to trip. The series capacitors have been bypassed in approximately 1.5 sec into the event. Measurements on the series capacitors indicated the presence of subsynchronous current. Within the wind farms, a large number of crowbars were activated [22].

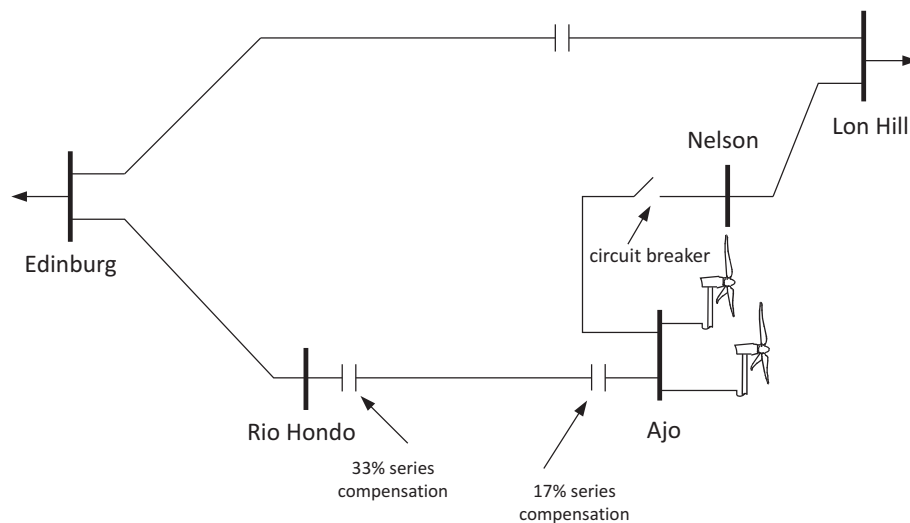


Fig. 2.16 Single-line diagram of the power system around Zorilla Gulf wind farm

The Zorilla Gulf wind farm was the first practical incident of SSR in variable speed wind turbine. Most of the installed wind turbines were of DFIG type. A typical DFIG wind turbine consists of an induction generator, whose stator is directly connected to the grid while a four quadrant Back-to-Back (BTB) converter connects the rotor to the grid. A three winding transformer connects the stator, the BTB converter and grid, as shown in Fig 2.17. Typically, the rotor-side converter (RSC) controls the torque and the reactive power of the generator, while the Grid Side Converter (GSC) controls the DC-link voltage and in some cases is utilized to control both the terminal and DC-link voltage [8] [22] [38] [39].

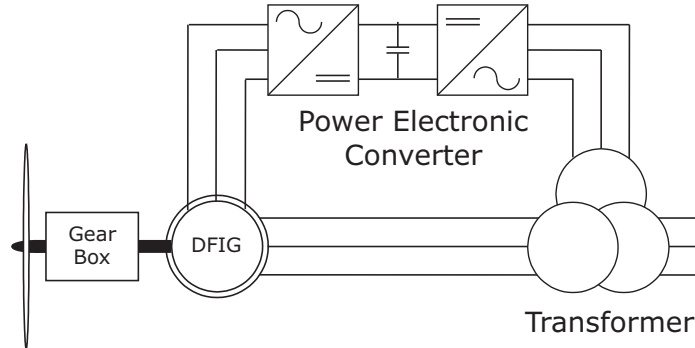


Fig. 2.17 Single-line diagram of a DFIG wind turbine

Following the incident, enormous efforts from the research community and turbine manufacturers were put forward to explain the phenomenon, while developing different mitigation techniques. The incident has been identified to have been caused by Subsynchronous Controller Interaction (SSCI) [3]. SSCI is a type of interaction that involves energy exchange between a power electronic device and a series compensated electrical network [23]. SSCI, like IGE, is a purely electrical phenomenon that does not involve the mechanical system. In most analysis, a modified model of the IEEE FBM for SSR analysis has been employed where the synchronous generator is replaced by an aggregate model of a DFIG farm [39] [9]. The focus of this thesis is to analyze the SSCI phenomenon in DFIG based wind farms, hence further details will be presented in the chapters that follow.

2.5.3 SSR in full-power converter wind turbines

Another variant of variable speed wind turbine solution is the full-power converter wind turbine. This wind turbine consists of a multiple-pole synchronous generator in series with a BTB converter as shown in Fig. 2.18. Due to variation in wind speed, the generated voltage at the generator terminal has a variable frequency. The BTB converter acts as a frequency converter to adopt the variable frequency voltage to the grid frequency.

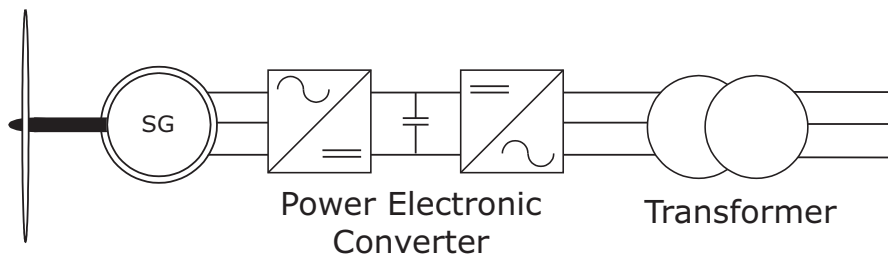


Fig. 2.18 Single-line diagram of a full-power converter wind turbine

The advantage of a full-power converter wind turbine over the DFIG, is the presence of BTB converter that creates a decoupling between the grid and the turbine. As a result, any oscillation that is triggered on the grid does not propagate towards the turbine. Hence SSR due to TI is very

unlikely in this types of wind turbines, although other type of interaction might need attention. Up to the time of writing this report, there exists no incident of SSR in wind farm involving full-power converter turbines.

2.6 Conclusion

In this chapter, an overview of the various types of SSR in power system has been covered. Various generator units and the associated types of SSR that can exist has been addressed. An introduction to different types of analysis approach has also been presented. SSR in classical generator units and fixed-speed wind turbines using linearized model has also been investigated.

Chapter 2. Subsynchronous Resonance in Power Systems

Chapter 3

DFIG Wind Turbine Model and Control

3.1 Introduction

The previous chapter has been dedicated to establish the basis for SSR both in classical and in wind-based generator units. Different investigation techniques used for assessing the risk of SSR have been addressed. As the focus of this thesis is on the investigation of SSCI in DFIG-based wind farms connected to series-compensated transmission lines, a proper model representation of the wind turbine becomes crucial. This chapter focuses on the description of the DFIG model used in this work. The purpose of the different components that build up a DFIG wind turbine is discussed. This is followed by a description of the control structure, thereby establishing the basis for the electrical dynamic behavior of the DFIG wind turbine.

3.2 DFIG wind turbine model

A typical configuration of a DFIG unit with its various components is illustrated in Fig.3.1. It consists of a Wound Rotor Induction Generator (WRIG). A Voltage Source Converter (VSC) based BTB converter, which allows operation in both the subsynchronous and supersynchronous speed range, connects the rotor to the grid. The stator of the induction generator is directly connected to the grid through a three-winding transformer. In the DFIG model that is considered for this work, the GSC controller controls the dc-link capacitor voltage while the RSC controller controls the PCC active and reactive power exchange of the DFIG. It is important to observe that only the slip power is handled by the converters. Therefore, the power rating for these converters are in the range of 15-30% of the turbine's rated power. This means that the losses in the converter and the cost of the converter are reduced in comparison to other topologies where the converter has to handle the total power.

In the subsections to follow, the model description of the induction generator followed by the model description for the dc-link capacitor are presented. Within this section, the description of the protection system for the DFIG is also addressed. In the next section, the model description for the RSC controller and GSC controller are covered. To avoid redundancy, the grid-side filter

model description is presented along side the GSC controller.

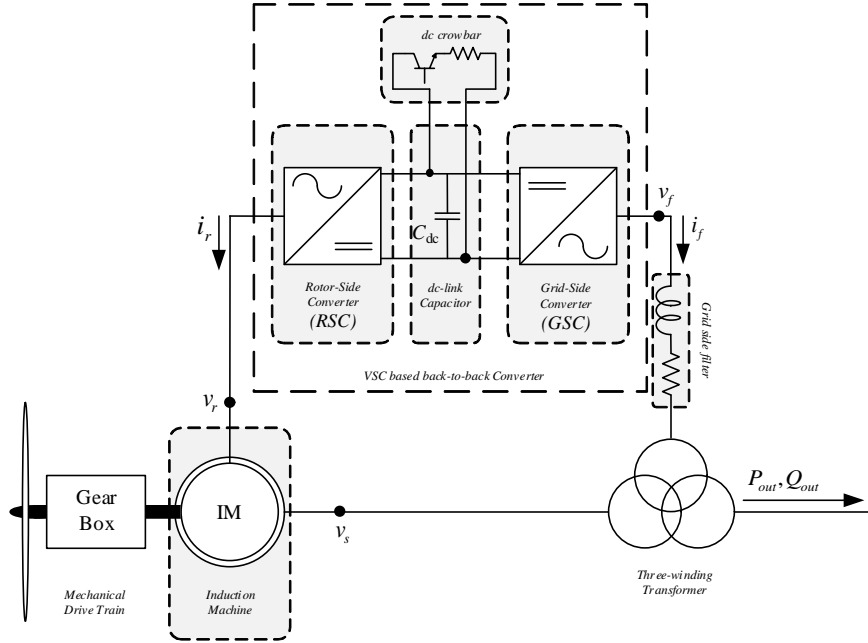


Fig. 3.1 Components of a DFIG turbine unit.

3.2.1 Induction generator

When modeling analytically an induction machine, a T-representation of the system can be adopted (see Fig.3.2(a)), where R_s and L_{ls} represent the stator winding losses and leakage inductance, respectively, while R_r and L_{lr} are the rotor winding losses and leakage inductance, respectively. The inductance L_m represents the magnetizing inductance of the machine while the back-EMF of the machine is represented as $j\omega_r \underline{\Psi}_r^{(s)}$ with ω_r representing the rotor angular frequency. Although this is an accurate way of modeling an induction machine, often when dealing with control systems, it is preferred to use a Γ -representation (Fig. 3.2(b)), due to its simplicity for deriving the control law. The main difference between these two models lies in where the leakage inductances are placed [38]. According to [40], it is possible to represent the machine with no loss of information by placing all the leakage inductances in the rotor circuit (see Fig. 3.2(b)). When moving from the T- to the Γ -representation, the relation between the different parameters [41]

$$\gamma = \frac{L_s}{L_m}, \quad \underline{v}_R = \gamma \underline{v}_r, \quad \underline{i}_R = \frac{\underline{i}_r}{\gamma}, \quad L_M = \gamma L_m \quad (3.1)$$

$$\underline{\Psi}_R = \gamma \underline{\Psi}_r, \quad R_R = \gamma^2 R_r, \quad L_R = \gamma L_{ls} + \gamma^2 L_{lr}$$

with $L_s = L_{ls} + L_m$. In this chapter and in the chapters that follow, expressions and parameters

3.2. DFIG wind turbine model

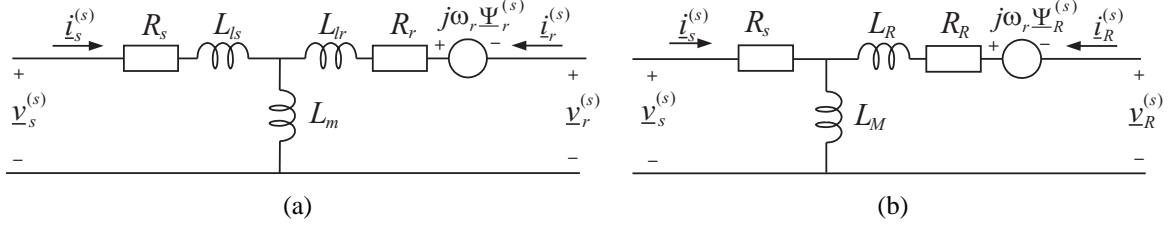


Fig. 3.2 Representation of an induction generator in the stationary-stator coordinate frame: (a) T-model representation and (b) Γ -model representation.

with the subscript “R” indicate that the Γ -representation of the machine is considered, whereas subscript “r” indicates T-model representation is considered.

With reference to the symbols introduced in Fig. 3.2(b), the equations governing the electrical dynamics of the machine in the stationary-stator coordinate frame are:

$$\underline{v}_s^{(s)} = R_s \underline{i}_s^{(s)} + \frac{d\underline{\Psi}_s^{(s)}}{dt} \quad (3.2)$$

$$\underline{v}_R^{(s)} = R_R \underline{i}_R^{(s)} + \frac{d\underline{\Psi}_R^{(s)}}{dt} - j\omega_r \underline{\Psi}_R^{(s)}$$

Using Park’s transformation, (3.2) can be transformed into the rotating dq -coordinate systems. Here, a flux-oriented dq frame, where the d -axis is aligned with the stator flux of the machine, has been selected. The resulting equations are given by (3.3)

$$\begin{aligned} \underline{v}_s^{(dq)} &= R_s \underline{i}_s^{(dq)} + \frac{d\underline{\Psi}_s^{(dq)}}{dt} + j\omega_s \underline{\Psi}_s^{(dq)} \\ \underline{v}_R^{(dq)} &= R_R \underline{i}_R^{(dq)} + \frac{d\underline{\Psi}_R^{(dq)}}{dt} + j\omega_2 \underline{\Psi}_R^{(dq)} \end{aligned} \quad (3.3)$$

ω_s corresponds to the synchronous angular frequency whereas $\omega_2 = \omega_s - \omega_r$ is the slip angular frequency. The stator and rotor fluxes expressed in (3.3) are given by

$$\underline{\Psi}_s^{(dq)} = L_M \left(\underline{i}_s^{(dq)} + \underline{i}_R^{(dq)} \right) \quad (3.4)$$

$$\underline{\Psi}_R^{(dq)} = L_M \underline{i}_s^{(dq)} + \underline{i}_R^{(dq)} (L_M + L_R) = L_R \underline{i}_R^{(dq)} + \underline{\Psi}_s^{(dq)}$$

Finally, the IG model must be completed by considering the mechanical dynamics of the machine. Here, it is important to stress that the aim of this work is on the investigation of resonance

conditions due to control interaction (SSCI, as discussed in Section 2.5.2); in this case, the mechanical system will have no impact on the system dynamics. For this reason, it is possible to model the mechanical side of the machine by simply using a single-mass representation, as

$$2H_g \frac{d\omega_g}{dt} = T_m - T_e - D_g \omega_g \quad (3.5)$$

where H_g is the inertia time-constant for the single mass. T_e and T_m are the electrical and mechanical torque, respectively. D_g is the damping coefficient while ω_g is the mechanical rotor speed. If a more detailed representation of the mechanical system is needed, a two-mass model as in the one presented in [9] can be adopted.

3.2.2 DC-link model

The dc-link of the BTB converter is modeled as a pure capacitor (losses are neglected). The aim of the dc-link for the BTB converter is to provide a temporary storage for the system to allow proper operation of the RSC and GSC. The capacitor is charged and discharged based on the power balance between the GSC and the RSC converter as indicated in Fig. 3.3.

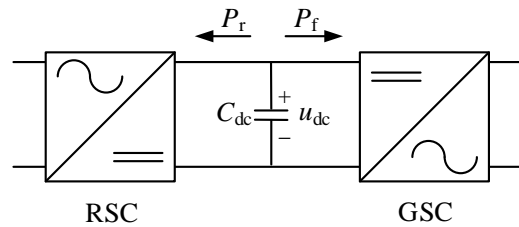


Fig. 3.3 DC-link model

With the signal convention given in Fig.3.3, the energy stored in the dc-link capacitor can be expressed as

$$\frac{dW_{dc}}{dt} = \frac{1}{2} C_{dc} \frac{du_{dc}^2}{dt} = -P_r - P_f \quad (3.6)$$

where W_{dc} is the energy stored in the dc-link while u_{dc} represents the dc-link capacitor voltage. Under the assumption that the dc-link capacitor C_{dc} is constant and the converters are lossless, the time derivative of the stored energy in the dc-link can be expressed in terms of the power balance between the RSC and GSC as in (3.6).

3.2.3 Protection for DFIG

The purpose of the protection system is to prevent any damage caused by high current as a result, for example, of sudden drop in the terminal voltage due to fault conditions in the grid.

From a hardware point of view, protection to the wind turbine is provided by using crowbars, either connected on the ac-side of the RSC or on the dc-link of the BTB converter. The latter will be discussed here. Fig.3.4 shows the single-line diagram for the BTB converter of the DFIG with dc crowbar. It is constituted by a breaking resistor in series with a static switch (typically, an IGBT) that is controlled using hysteresis control. The role of the dc-crowbar is to absorb the exceeding energy coming from the RSC during large disturbances in order to avoid excessive over-voltages across the dc-link capacitors.

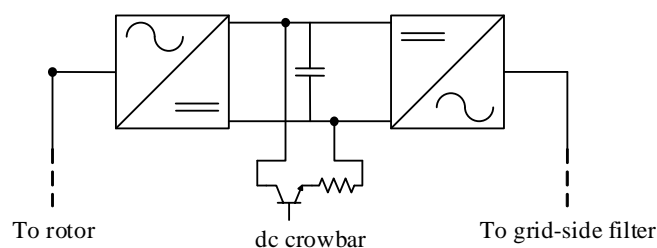


Fig. 3.4 Single-line diagram of DFIG converter with dc crowbar

However, the DFIG performance under large transient is beyond the scope of this work. For this reason, the dc crowbar is neglected during the modeling. For interested readers, additional information can be found in [42] [43].

3.3 DFIG control

The principle of using space vectors to represent three phase AC quantities as vectors having dc characteristics, creates the freedom of using conventional PI controller for control purposes. A typical control structure for a DFIG turbine is shown in Fig. 3.5. The RSC and GSC are controlled independently from each other. A Phase-Locked Loop (PLL) is used for synchronization purpose. The details of the different control loops are discussed in the upcoming subsections.

3.3.1 Rotor-side converter controller

The aim of the RSC is to control the terminal active and reactive power of the DFIG system. The control for this converter has a cascade structure, with an inner current controller and an outer power controller. The outer controller generates the reference rotor current ($i_{R,d}^*$ and $i_{R,q}^*$), which serve as an input to the inner current controller. The controller is derived based on the Γ -representation of induction generator. As a result, measured quantities and generator parameters are transformed to the Γ -representation using the expression given in (3.1).

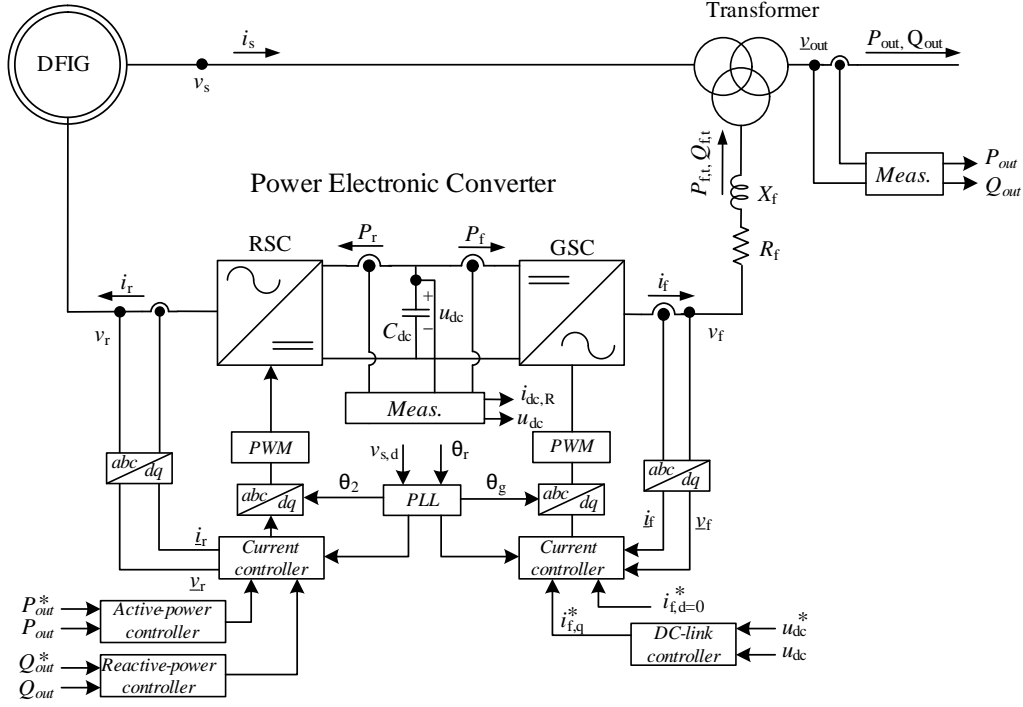


Fig. 3.5 Detailed controller structure for DFIG

Active and reactive power controller

The terminal power, P_{out} , of the wind turbine is composed of two components, the power through the stator, P_s , and the power through the grid side filter, $P_{f,t}$ as

$$P_{out} = P_s + P_{f,t} \quad (3.7)$$

The power through the stator has a proportional relation to the electrical torque and speed as

$$P_s \propto T_e \omega_r \quad (3.8)$$

where T_e is expressed as $T_e = 3n_p \text{Im} \left[\underline{\Psi}_s^{(dq)} \text{Conj} \left(\underline{i}_R^{(dq)} \right) \right]$. Considering a stator-flux oriented dq -frame, the electrical torque expression reduces to

$$T_e = 3 \left(n_p \Psi_{s,d} i_{R,q} \right) \quad (3.9)$$

From (3.8) and (3.9), it can be deduced that the q -component of the rotor current can be used to control the stator active power (P_s). However, the aim of the power controller is not to control the stator power (P_s) but the terminal power (P_{out}) of generator. In order to control the terminal power in a closed-loop manner, the power $P_{f,t}$ in (3.7) is considered as a disturbance as depicted in Fig. 3.6. The error introduced as a result of $P_{f,t}$ is instead taken care of by the integrator term of the power controller (see Fig. 3.6).

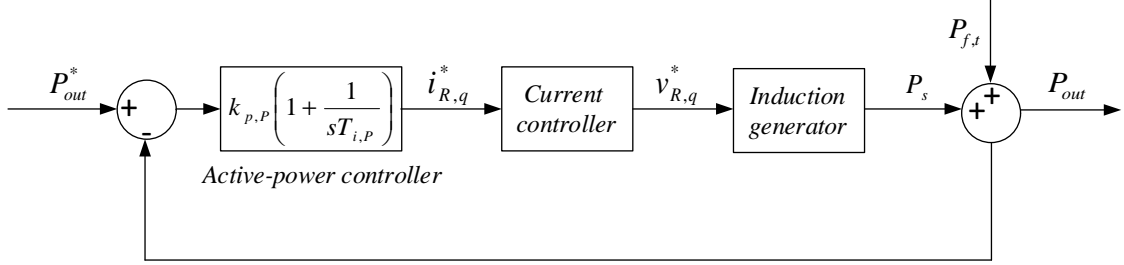


Fig. 3.6 Main structure for active power controller for DFIG

Similar to the active power, the terminal reactive power, Q_{out} , is composed of stator reactive power (Q_s) and reactive power through the grid-side filter ($Q_{f,t}$). According to [41], the reactive power through the stator (again, considering a flux oriented dq -frame and a Γ -representation of the machine) can be expressed as

$$Q_s = 3 \left[\omega_1 \Psi_{s,d} \left(\frac{\Psi_{s,d}}{L_M} - i_{R,d} \right) \right] \quad (3.10)$$

From (3.10), it can be seen that the stator reactive power (Q_s) can be controlled by controlling the d -component of the rotor current ($i_{R,d}$) whereas the reactive power contribution from the grid-side filter ($Q_{f,t}$) is effectively controlled to zero in steady-state by the GSC controller. The block diagram of the implemented reactive-power controller is depicted in Fig. 3.7.

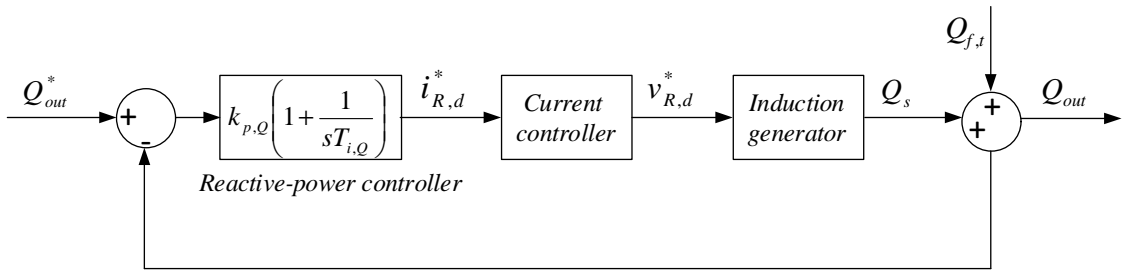


Fig. 3.7 Main structure for reactive power controller for DFIG

The pu control law governing the active and reactive power controller in the Laplace domain are then given as

$$i_{R,q}^*(s) = k_{p,P} \left(1 + \frac{1}{sT_{i,P}} \right) (P_{out}^*(s) - P_{out}(s)) \quad (3.11)$$

$$i_{R,d}^*(s) = k_{p,Q} \left(1 + \frac{1}{sT_{i,Q}} \right) (Q_{out}^*(s) - Q_{out}(s))$$

where “ s ” represents the Laplace variable. The terms k_p and T_i are the proportional gain and integrator time-constant, respectively. The outputs from these controllers serve as reference current input for the rotor current control loop.

Rotor-side current controller

Let us now observe the equivalent circuit of the induction generator (using Γ -representation) in series with the RSC shown in Fig. 3.8. The rotor voltage (v_R) at the rotor terminal in the dq frame can be expressed as:

$$\underline{v}_R^{(dq)} = R_R \underline{i}_R^{(dq)} + \frac{d\underline{\Psi}_R^{(dq)}}{dt} + j\omega_2 \underline{\Psi}_R^{(dq)} \quad (3.12)$$

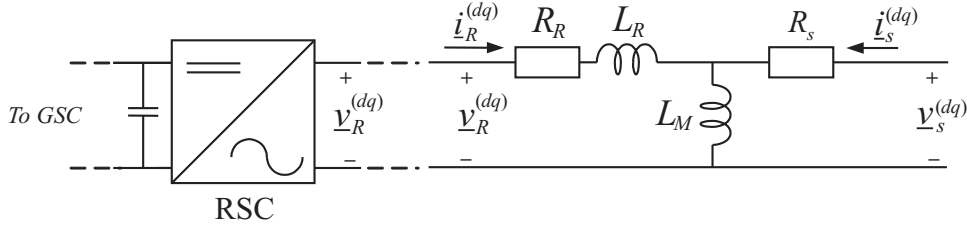


Fig. 3.8 RSC in series with Γ -model representation of an induction generator

Taking the rotor flux equation in (3.4) with $\underline{\Psi}_R^{(dq)} = L_R \underline{i}_R^{(dq)} + \underline{\Psi}_s^{(dq)}$ and substituting it into (3.12), the expression for the rotor voltage can be rewritten as

$$\underline{v}_R^{(dq)} = (R_R + j\omega_2 L_R) \underline{i}_R^{(dq)} + L_R \frac{d\underline{i}_R^{(dq)}}{dt} + \underbrace{\frac{d\underline{\Psi}_s^{(dq)}}{dt} + j\omega_2 \underline{\Psi}_s^{(dq)}}_{\underline{e}_{emf}^{(dq)}} \quad (3.13)$$

where $\underline{e}_{emf}^{(dq)}$ represents the back EMF of the machine. The above equation can be rearranged to describe the dynamics of the rotor current as

$$L_R \frac{d\underline{i}_R^{(dq)}}{dt} = \underline{v}_R^{(dq)} - R_R \underline{i}_R^{(dq)} - j\omega_2 L_R \underline{i}_R^{(dq)} - \underline{e}_{emf}^{(dq)} \quad (3.14)$$

Further, (3.14) can be expressed explicitly in terms of its d and q components as

$$\begin{aligned} L_R \frac{di_{R,d}}{dt} &= v_{R,d} - R_R i_{R,d} + \omega_2 L_R i_{R,q} - e_{emf,d} \\ L_R \frac{di_{R,q}}{dt} &= v_{R,q} - R_R i_{R,q} - \omega_2 L_R i_{R,d} - e_{emf,q} \end{aligned} \quad (3.15)$$

From (3.15), it can be observed that there exist a cross-coupling between the $i_{R,d}$ and $i_{R,q}$ currents. In the control law described in [41] [44], it is possible to decouple the cross-coupling between the $i_{R,d}$ and $i_{R,q}$ and compensate for the back EMF of the machine in order to archive

3.3. DFIG control

an independent control of the d - and q -current and, thereby, of the active and reactive power. This is accomplished by introducing a decoupling term $j\omega_2 L_R \dot{i}_R^{(dq)}$ and a feed-forward term for the estimated back EMF as

$$\underline{v}_R^{*(dq)} = \underline{v}_R^{(dq)'} + j\omega_2 L_R \dot{i}_R^{(dq)} + \hat{\underline{e}}_{emf}^{(dq)} \quad (3.16)$$

where $\underline{v}_R^{(dq)'}$ is the output from the PI controller. In this analysis, the converters are treated as lossless linear amplifiers. In addition they are assumed to be ideal, meaning that they are able to generate the reference voltage with no delay as

$$\underline{v}_R^{*(dq)} = \underline{v}_R^{(dq)} \quad (3.17)$$

Now moving the analysis to Laplace domain, the dynamics of the rotor current expressed in (3.14) can be rewritten as

$$sL_R \dot{i}_R^{(dq)}(s) = \underline{v}_R^{(dq)}(s) - R_R \dot{i}_R^{(dq)}(s) - j\omega_2 L_R \dot{i}_R^{(dq)}(s) - \hat{\underline{e}}_{emf}^{(dq)}(s) \quad (3.18)$$

Similarly, the reference voltage expression of (3.16) along side the structure for controller in Laplace domain can be expressed as

$$\begin{aligned} \underline{v}_R^{(dq)*}(s) &= \underline{v}_R^{(dq)'}(s) + j\omega_2 L_R \dot{i}_R^{(dq)}(s) + \hat{\underline{e}}_{emf}^{(dq)}(s) \\ &= F_{cc,R}(s) \left(\dot{i}_R^{(dq)*}(s) - \dot{i}_R^{(dq)}(s) \right) + j\omega_2 L_R \dot{i}_R^{(dq)}(s) + \hat{\underline{e}}_{emf}^{(dq)}(s) \end{aligned} \quad (3.19)$$

where $F_{cc,R}(s)$ is the transfer function of the controller applied to the current error. Under the previous assumption that $\underline{v}_R^{(dq)*} = \underline{v}_R^{(dq)}$ and assuming a perfect estimation of the back EMF, (3.18) and (3.19) can be combined as

$$\begin{aligned} sL_R \dot{i}_R^{(dq)}(s) &= -R_R \dot{i}_R^{(dq)}(s) + F_{cc,R}(s) \left(\dot{i}_R^{(dq)*}(s) - \dot{i}_R^{(dq)}(s) \right) \Rightarrow \\ \dot{i}_R^{(dq)}(s) &= \underbrace{\frac{1}{sL_R + R_R}}_{G_{cc,R}(s)} F_{cc,R}(s) \left(\dot{i}_R^{(dq)*}(s) - \dot{i}_R^{(dq)}(s) \right) \end{aligned} \quad (3.20)$$

Rearranging (3.20), the closed-loop expression from $\dot{i}_R^{(dq)*}(s)$ to $\dot{i}_R^{(dq)}(s)$ can be obtained as

$$\dot{i}_R^{(dq)}(s) = \underbrace{\frac{G_{cc,R}(s) F_{cc,R}(s)}{1 + G_{cc,R}(s) F_{cc,R}(s)}}_{G_{cc,cl}(s)} \dot{i}_R^{(dq)*}(s) \quad (3.21)$$

Using Internal Model Control (IMC) [45] [46], the closed-loop can be shaped as a first order low-pass filter having a closed-loop bandwidth $\alpha_{cc,R}$ as

$$G_{cc,cl}(s) = \frac{\alpha_{cc,R}}{s + \alpha_{cc,R}} = \frac{\frac{\alpha_{cc,R}}{s}}{1 + \frac{\alpha_{cc,R}}{s}} \quad (3.22)$$

Chapter 3. DFIG Wind Turbine Model and Control

From (3.21) and (3.22), the transfer function of the controller $F_{cc,R}(s)$ can be obtained as

$$F_{cc,R}(s) = \frac{\alpha_{cc,R}}{s} G_{cc,R}^{-1}(s) = \frac{\alpha_{cc,R}}{s} (sL_R + R_R) = \alpha_{cc,R}L_R + \frac{\alpha_{cc,R}R_R}{s} \quad (3.23)$$

which indicates that $F_{cc,R}(s)$ is a PI controller with a proportional $k_{p,cc}$ equal to $\alpha_{cc,R}L_R$ and integral gain $k_{i,cc}$ equal to $\alpha_{cc,R}R_R$. Here it is worth noting that the aim of the RSC is to control the active and reactive powers. As a result, the integral part of the inner current controller can be omitted as any steady-state error that could arise is taken care of by the integral action of the outer-loop controller. Under this assumption, the control law for the RSC current controller considered for this work is given by

$$\underline{v}_R^{*(dq)} = k_{p,cc} \left(\underline{i}_R^{(dq)*}(s) - \underline{i}_R^{(dq)}(s) \right) + j\omega_2 L_R \underline{i}_R^{(dq)}(s) + \underbrace{\frac{1}{sT_{LP} + 1}}_{H_{LP}(s)} \hat{e}_{emf}^{(dq)}(s) \quad (3.24)$$

where $k_{p,cc}$ is as defined in (3.23). Note that a low-pass filter term $H_{LP}(s)$ with a time constant T_{LP} is introduced to reduce the dynamics in the estimated back EMF.

3.3.2 Grid-side converter controller

The purpose of the GSC converter is to maintain the dc-link capacitor voltage to its reference value by controlling the active power flow through the grid-side filter. Similar to the RSC, it has a cascade structure with an outer dc-link voltage controller and an inner current controller (see Fig.3.5). The inner current controller receives the reference current ($\underline{i}_f^{(dq)*}$) from the outer controller and outputs the reference voltage ($\underline{v}_f^{(dq)*}$) for the GSC. The controller for the GSC is aligned with the grid flux meaning that the voltage vector, $\underline{v}_g^{(dq)}$ shown in Fig.3.9, is aligned with the q -axis. The apparent power at the terminal of the grid-side filter can be expressed as

$$S_{f,t} = P_{f,t} + jQ_{f,t} \xrightarrow{\text{for } v_{g,d}=0} 3 \left\{ jv_{g,q} \text{conj} \left[\underline{i}_f^{(dq)} \right] \right\} \quad (3.25)$$

Thus, the active and reactive power through the grid-side filter can be expressed as

$$P_{f,t} = 3v_{g,q}i_{f,q} \quad (3.26)$$

$$Q_{f,t} = 3v_{g,q}i_{f,d}$$

Grid-side current controller

Fig. 3.9 shows the equivalent circuit for the grid side filter along side the GSC. The grid-side filter consists of a inductance L_f and a resistance R_f . The voltage equation at the terminal of the GSC can be written as

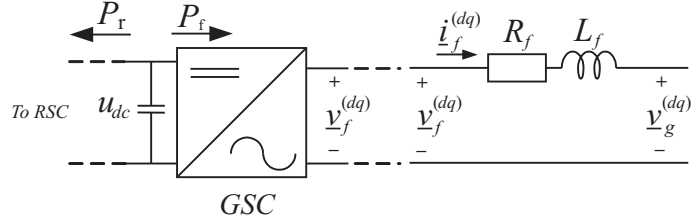


Fig. 3.9 GSC converter with grid-side filter

$$\underline{v}_f^{(dq)} = R_f \underline{i}_f^{(dq)} + L_f \frac{d\underline{i}_f^{(dq)}}{dt} + j\omega_s L_f \underline{i}_f^{(dq)} + \underline{v}_g^{(dq)} \quad (3.27)$$

Following the same procedure described for the derivation of the RSC current controller, the control law for the GSC current controller in the Laplace domain can be expressed as

$$\underline{v}_f^{*(dq)}(s) = \left(k_{pf,cc} + \frac{k_{if,cc}}{s} \right) \left(\underline{i}_f^{*(dq)}(s) - \underline{i}_f^{(dq)}(s) \right) + j\omega_s L_f \underline{i}_f^{(dq)}(s) + \underbrace{\frac{1}{sT_{LP} + 1}}_{H_{LP}(s)} \underline{v}_g^{(dq)}(s) \quad (3.28)$$

where, calling $\alpha_{cc,f}$ the closed-loop current controller bandwidth, the parameters for the PI regulator are given by $k_{pf,cc} = \alpha_{cc,f} L_f$ and $k_{if,cc} = \alpha_{cc,f} R_f$. Again, the measured grid voltage is filtered to reduce its dynamics. The block diagram describing the GSC current controller is depicted in Fig. 3.10

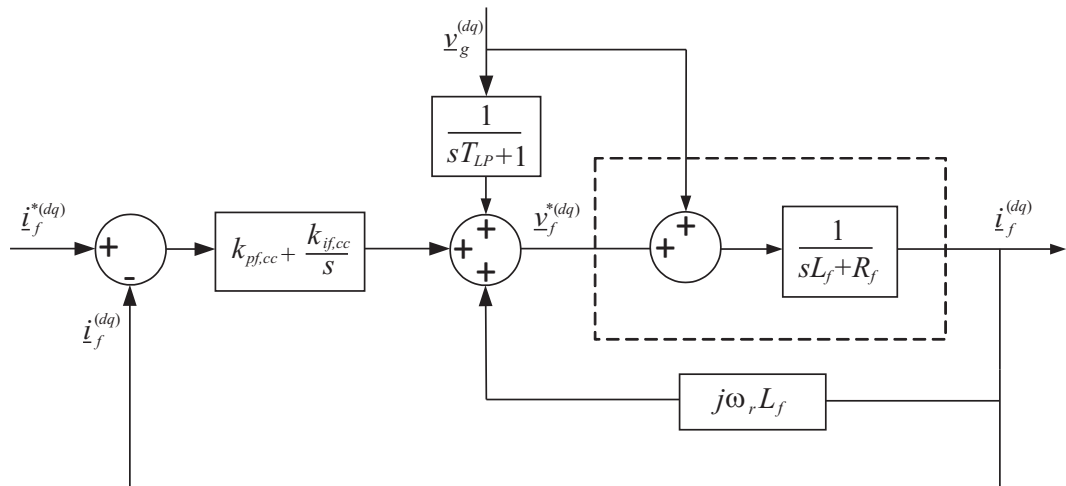


Fig. 3.10 Block diagram of the GSC current controller

Dc-link voltage controller

The dc-link capacitor voltage can be controlled in two ways: in terms of the dc-link voltage (u_{dc}) involving the flow of current in and out of the dc-link or in terms of the energy stored in the dc-link capacitor involving the power exchange. The latter is adopted in this thesis. For the sake of clarity, the dynamics of the dc-link described in (3.6) is repeated here

$$\frac{dW_{dc}}{dt} = \frac{1}{2}C_{dc} \frac{du_{dc}^2}{dt} = -P_f - P_R \quad (3.29)$$

where P_R is the power flowing into the RSC considering the Γ -representation of the induction generator. P_f is the power flowing into the GSC as indicated in Fig. 3.3. It should be noted that (3.29) is non-linear in nature due to the u_{dc}^2 term. With the aim of extracting the control law, the above expression can be linearized, resulting in

$$\frac{1}{2}C_{dc}u_{dc,0} \frac{d\Delta u_{dc}}{dt} = -\Delta P_f - \Delta P_R \quad (3.30)$$

where $u_{dc,0}$ is the dc-link voltage at the operating point. Equation (3.30) hints that, the relation is operating point dependent. To avoid this, a technique called feedback linearization [45] can be employed, in which a non-linear equation can be replaced with an equivalent linear equation where traditional control techniques can be employed. Here the square of the voltage, u_{dc}^2 , is replaced with a new variable, W , which in physical sense represents the energy in the capacitor as [42] [45]. The dc-link dynamics can now be rewritten as

$$\frac{1}{2}C_{dc} \frac{dW}{dt} = -P_f - P_R \quad (3.31)$$

Fig. 3.11 shows the open-loop dynamics for the dc-link capacitor. From the controller point of view, P_R can be viewed as a disturbance. Using IMC, as in previous sections, the dc-link controller can be shaped as a first order low-pass filter having a closed-loop bandwidth α_{dc} , resulting in a proportional controller with a gain $k_{p,dc} = -\alpha_{dc}C_{dc}$. As the dc-link voltage controller is an outer-control loop, any steady-state error that could arise due to parameters mismatch or disturbances can not be removed through a proportional controller. To alleviate this, a small integral term is introduced during the controller design. This is achieved by introducing active damping during the design as in [45] [47].

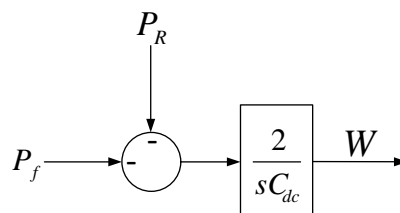


Fig. 3.11 Block diagram of dc-link capacitor dynamics

3.3. DFIG control

Considering the GSC to be lossless and the losses in the grid-side filter to be negligible, the power P_f at the terminal of GSC converter can be approximated as

$$P_f \approx P_{f,t} = 3v_{g,q}i_{f,q} \quad (3.32)$$

Inserting (3.32) into (3.31), under the assumption that the voltage vector is perfectly aligned with the q -axis as $\underline{v}_g = jv_{g,q}$, the dc-link expression from (3.31) reduces to

$$\frac{1}{2}C_{dc} \frac{dW}{dt} = -3|v_g|i_{f,q} - P_R \quad (3.33)$$

The control law governing the q -component of the filter current ($i_{f,q}^*$) with active damping term as implemented in [45] is expressed below

$$i_{f,q}^* = i'_{f,q} + G_a W \quad (3.34)$$

where $i'_{f,q}$ is the controller output and G_a is the gain of the active damping term. Considering the inner current controller is much faster than the outer loop for stability reasons ($i_{f,q}^* = i_{f,q}$), the above expression can be inserted in (3.33) to obtain

$$\frac{1}{2}C_{dc} \frac{dW}{dt} = -3|v_g| \left(i'_{f,q} + G_a W \right) - P_R \quad (3.35)$$

Treating P_R as a disturbance, the transfer function from $i'_{f,q}$ to W can be written as

$$W(s) = \frac{-6|v_g|}{\underbrace{sC_{dc} + 6|v_g|G_a}_{G_{dc}(s)}} i'_{f,q}(s) \quad (3.36)$$

with

$$i'_{f,q}(s) = F_{dc}(s) (W(s)^* - W(s))$$

F_{dc} represents the transfer function of the controller. With the aim of shaping the closed-loop system behavior to a first order low-pass filter that has a desired bandwidth of α_{dc} , $F_{dc}(s)$ can be obtained using IMC as

$$F_{dc}(s) = k_{p,dc} + \frac{k_{i,dc}}{s} = \frac{\alpha_{dc}}{s} G_{dc}^{-1}(s) = -\frac{\alpha_{dc}C_{dc}}{6|v_g|} - \frac{\alpha_{dc}G_a}{s} \quad (3.37)$$

As done in [45], by placing the poles of $G_{dc}(s)$ at α_{dc} , the closed-loop system can retain a closed-loop bandwidth corresponding to α_{dc} as

$$G_{dc}(s) = \frac{-6|v_g|}{sC_{dc} + 6|v_g|G_a} \Rightarrow \frac{6|v_g|G_a}{C_{dc}} = \alpha_{dc} \quad (3.38)$$

resulting in $G_a = \frac{\alpha_{dc} C_{dc}}{6|v_g|}$. Combining (3.37) with the Laplace transform of (3.34), an expression for the dc-link voltage controller is obtained as (3.39). A block-diagram description for the dc-link voltage controller is also shown in Fig. 3.12

$$i_{f,q}^*(s) = \left(k_{p,dc} + \frac{k_{i,dc}}{s} \right) (W(s)^* - W(s)) + G_a W(s) \quad (3.39)$$

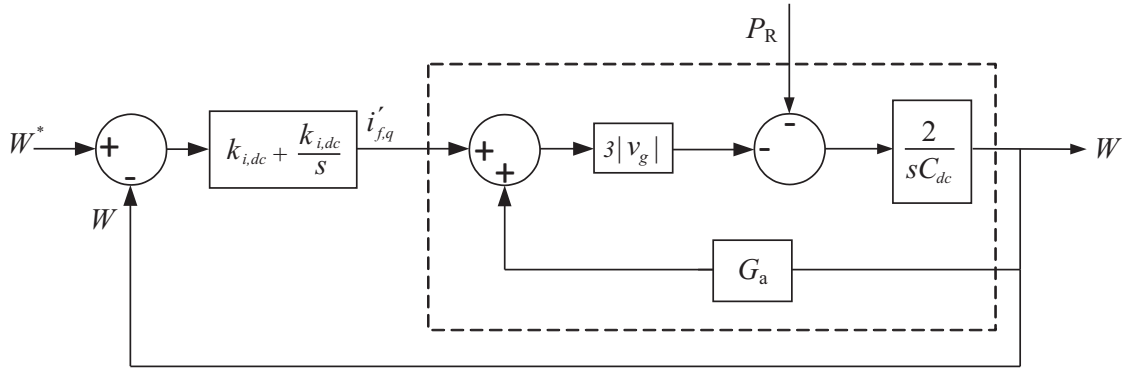


Fig. 3.12 Block diagram of the closed-loop controller for the dc-link voltage

As briefly mentioned earlier, the d -component of the filter current can be used to control the reactive power output from the GSC. In this thesis the reactive current component, $i_{f,d}$, is controlled to zero by setting $i_{f,d}^* = 0$. This is to indicate that in steady-state, the reactive power ($Q_{f,t}$) output from the grid-filter is effectively controlled to zero.

3.3.3 Phase-locked loop

In sections leading up to this, it has been mentioned that a stator flux oriented dq -coordinate frame has been used, where the voltage vector ($v_s^{(s)}$) is aligned with the q -axis. The alignment of the voltage vector with the q -axis is achieved through the knowledge of the phase angle (θ_s) for $v_s^{(s)}$. As the angle of the voltage vector is not known, a PLL is used for estimation purpose. The control law of the PLL is as below

$$\begin{aligned} \dot{\hat{\omega}}_s &= k_{i,PLL} \epsilon_{PLL} \\ \dot{\hat{\theta}}_s &= \hat{\omega}_s + k_{p,PLL} \epsilon_{PLL} \end{aligned} \quad (3.40)$$

where $\hat{\omega}_s$ and $\hat{\theta}_s$ are the estimated grid frequency and voltage angle, respectively. The gains $k_{p,PLL} = 2\alpha_{PLL}$ and $k_{i,PLL} = \alpha_{PLL}^2$ are selected in accordance to [48]. ϵ_{PLL} is the error signal for the PLL. In order to determine the error signal for the PLL, the focus is directed to Fig. 3.13 where a voltage vector ($v_s^{(s)}$) together with the stationary xy -frame and a non-aligned dq -frame is shown. As can be seen, the dq decomposition of the voltage vector ($v_s^{(s)}$) results in a non-zero d -component. It can be seen easily that the d -component of voltage is given by

$$v_{s,d} = - \left| v_s^{(s)} \right| \sin(\theta_s - \hat{\theta}_s) \quad (3.41)$$

Taking $\theta_s - \hat{\theta}_s$ to be very small ($\sin(\theta_s - \hat{\theta}_s) \approx (\theta_s - \hat{\theta}_s)$), (3.41) can be considered to extract the error signal, ε , for the PLL as

$$\varepsilon = - \frac{v_{s,d}}{\left| v_s^{(s)} \right|} \quad (3.42)$$

Therefore, by choosing the error signal (ε_{PLL}) as (3.42), the PLL can be made to adjust $\hat{\omega}_s$ thereby changing $\hat{\theta}_s$ until the error ($-\frac{v_{s,d}}{\left| v_s^{(s)} \right|}$) is set to zero.

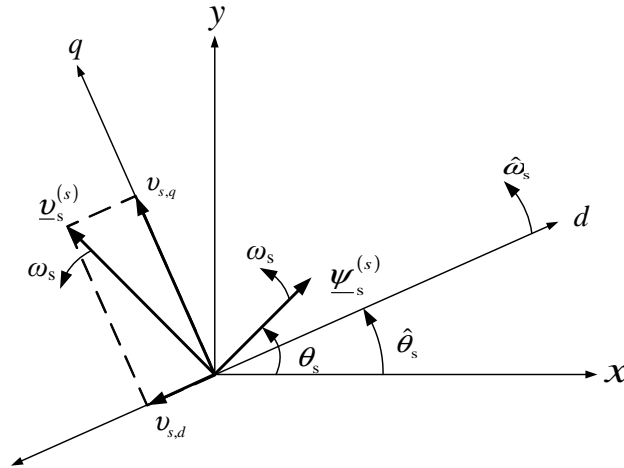


Fig. 3.13 Decomposition of voltage vector ($v_s^{(s)}$) into a non-aligned dq frame

Fig. 3.14 shows the block diagram of the adopted PLL structure. The voltage vector ($v_s^{(s)}$) is transformed to the dq -frame using the estimated $\hat{\theta}_s$. From the decomposed dq components of the voltage vector, the d -component is normalized with the magnitude of the voltage vector which is fed into the PLL structure described by (3.40) (shown highlighted in Fig. 3.14). The updated estimated phase is fed back to the stationary to dq transformation block to produce the updated dq decomposition of the voltage vector. This way, the PLL works to set the error to zero.

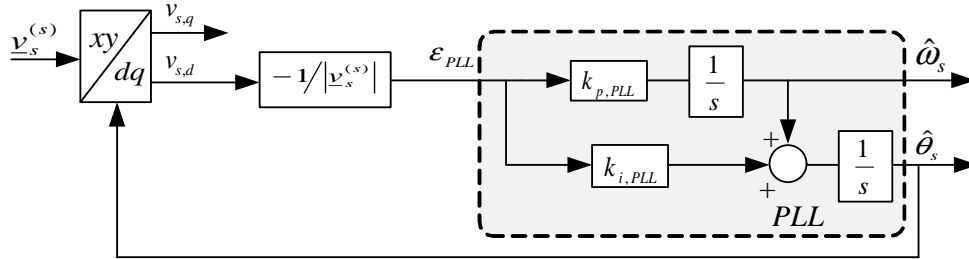


Fig. 3.14 Block diagram of PLL

Here it is important to stress that, if the investigation is related to the GSC, then the voltage vector ($\underline{v}_s^{(s)}$) in the above analysis should be replaced with filter voltage vector ($\underline{v}_g^{(s)}$). In a similar manner, transformations dealing with quantities on the rotor-side should take into account both the rotor speed (ω_r) and position angle (θ_r).

3.4 Conclusion

This chapter mainly focused on establishing an understanding on the modeling of a DFIG wind turbine system used in this work. The different components making up the wind turbine were explained. The chapter aims to create the basis for how the control system in this types of wind turbine works. A mathematical description of the control mechanism for the RSC and GSC are also presented.

Chapter 4

System Admittance Modeling

4.1 Introduction

In chapter 2, investigation techniques used to analyze the risk of SSR has been addressed. One of these techniques is the Eigenvalue analysis which requires a single mathematical model describing the overall system. eigenvalue analysis is a good tool in obtaining information regarding the damping of system modes with their corresponding frequency of oscillation. Numerous works investigating DFIG based wind farms connected to series compensated transmission line can be found. Among these, the most cited works are [9] and [10].

The work in [9], based on eigenvalue analysis, identifies and classifies the various modes of system as subsynchronous, supersynchronous, torsional and network modes. In identifying the impact of compensation level and output power (wind speed), the work neglected the torsional dynamics and turbine controller thereby focusing on the observation of the IGE phenomenon. However, the overall analysis was based on creating a linearized model of the overall system from a set of non-linear equations describing the system which is unique for each variation of system or controller parameter. In [10], the stability analysis has been performed using participation factor analysis of parameters (both of the system and the controller) to identify parameters and system conditions that influence the stability of the overall system. It evaluated the impact of system parameters like level of series compensation and wind speed on the dominant eigenvalue.

Another approach that has gained popularity is the impedance based analysis method. In [14], an impedance based Nyquist stability was employed to identify SSR risk in DFIG based wind farms. A space vector approach was used to develop the impedance both for DFIG and the series-compensated transmission line. The derived impedance model however did not take into account the outer-loop controllers. The work in [49], has been dedicated to develop three different small-signal sequence impedances of the DFIG that are valid for different frequency ranges. Based on the developed impedance of the DFIG and the impedance from transmission grid, the authors asses system stability based on the phase margin.

So far, irrespective of the analysis approach chosen, a proper mathematical representation of

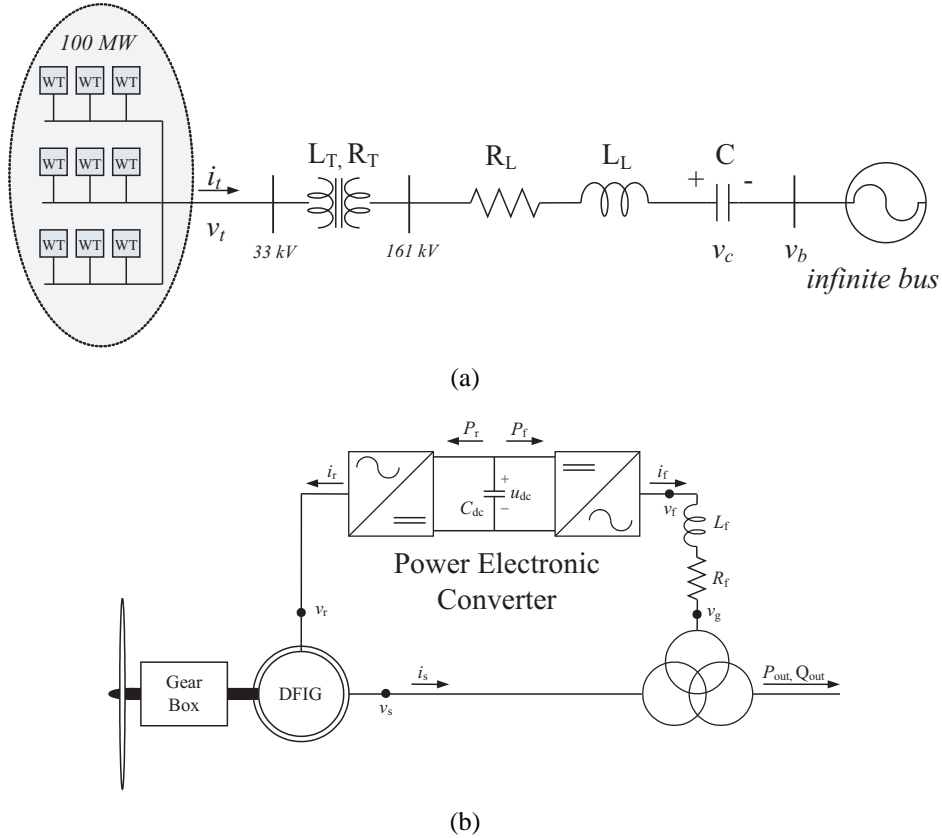


Fig. 4.1 (a) Single-line diagram of wind farm connected to a series-compensated transmission line, (b) single line diagram of a wind turbine unit.

the investigated system plays a major role in the whole process. This chapter tries to develop a mathematical representation for the system that can be utilized to identify and investigate the risk of SSCI. Section 4.2 starts off by presenting an overview of the investigated system. Section 4.3 is dedicated to the development of a model representation for the transmission grid. This is followed by a section dealing with model representation and verification of the DFIG system.

4.2 Investigated system overview

A single line diagram of the studied power system is shown in 4.1(a). It is adopted from the IEEE FBM where the synchronous generator is replaced with a 100 MW DFIG based wind farm. The 100 MW wind farm is an aggregate model of 50 wind turbines with each wind turbine rated at 2 MW. The 2MW DFIG model used in this work is based on a generic model that was verified against a 2-MW V90 Vestas turbine installed at Tvååker, Sweden [42]. It is based on the parameters of this 2 MW wind turbine that the 100 MW/33 kV aggregate model is developed. The wind farm is then connected to an infinite bus via a 161 kV series compensated transmission line. In this thesis, the point where the transmission line meets the low voltage

side of the transformer is referred to as the Point of Common Coupling (PCC). The values of the parameters for the aggregate model used in this work are presented in Table.5.1

This section broadly highlights the components of the investigated system. However, performing SSR stability analysis requires development of a proper system model. In the next section, the transmission grid admittance will be derived.

4.3 Grid admittance

Fig. 4.1(a) shows an aggregate wind farm radially connected to a series-compensated transmission line. The transmission line is derived based on IEEE FBM for SSR analysis (see Appendix), with the parameters adopted to accommodate the aggregate wind turbine model. v_t is the voltage at the connection point to the wind farm. R_T and R_L are the resistive losses of the grid transformer and the transmission line, respectively. L_T and L_L are the inductive losses of the grid transformer and the transmission line, respectively. C represents the capacitance of the fixed-series compensation whereas v_b represents the infinite bus voltage. The state-space representation of the transmission grid is derived in the DFIG rotating reference frame (dq) that is aligned with the stator flux. In reference with symbols shown in Fig. 4.1(a), the voltage at the connection point can be expressed as

$$v_t^{(dq)} = R_{tot}i_t^{(dq)} + L_{tot}\frac{di_t^{(dq)}}{dt} + j\omega_s L_{tot}i_t^{(dq)} + v_c^{(dq)} + v_b^{(dq)} \quad (4.1)$$

with $R_{tot} = R_L + R_T$ and $L_{tot} = L_L + L_T$. ω_s is the synchronous angular frequency. In a similar manner, the dynamics of the fixed-series capacitor can be written as

$$\frac{dv_c^{(dq)}}{dt} = \frac{1}{C}i_l^{(dq)} - j\omega_s v_c^{(dq)} \quad (4.2)$$

By explicitly extracting the d and q component of (4.1) and (4.2), the state-space expression for

TABLE 4.1. PARAMETERS OF THE 100 MW AGGREGATE MODEL

Rated power	100 MW
Rated voltage	33 kV
X_{ls}	0.158367 pu
X_m	3.8271871 pu
X_{lr}	0.065986 pu
R_s	0.0092417 pu
R_r	0.0075614 pu
X_f	1.055 pu
R_f	0.1055 pu
C_{dc}	437 μ F

Chapter 4. System Admittance Modeling

the transmission line can be derived as

$$\begin{aligned} \frac{d}{dt} \begin{bmatrix} \dot{i}_{t,d} \\ \dot{i}_{t,q} \\ v_{c,d} \\ v_{c,q} \end{bmatrix} &= \mathbf{A}_{TL} \begin{bmatrix} \dot{i}_{t,d} \\ \dot{i}_{t,q} \\ v_{c,d} \\ v_{c,q} \end{bmatrix} + \mathbf{B}_{TL,1} \begin{bmatrix} v_{t,d} \\ v_{t,q} \end{bmatrix} + \mathbf{B}_{TL,2} \begin{bmatrix} v_{b,d} \\ v_{b,q} \end{bmatrix} \\ \begin{bmatrix} \dot{i}_{t,d} \\ \dot{i}_{t,q} \end{bmatrix} &= \mathbf{C}_{TL} \begin{bmatrix} \dot{i}_{t,d} \\ \dot{i}_{t,q} \\ v_{c,d} \\ v_{c,q} \end{bmatrix} \end{aligned} \quad (4.3)$$

where

$$\begin{aligned} \mathbf{A}_{TL} &= \begin{bmatrix} -\frac{R_{tot}}{L_{tot}} & \omega_s & -\frac{1}{L_{tot}} & 0 \\ -\omega_s & -\frac{R_{tot}}{L_{tot}} & 0 & -\frac{1}{L_{tot}} \\ \frac{1}{C} & 0 & 0 & \omega_s \\ 0 & \frac{1}{C} & -\omega_s & 0 \end{bmatrix}, \\ \mathbf{B}_{TL,1} &= \begin{bmatrix} \frac{1}{L_{tot}} & 0 \\ 0 & \frac{1}{L_{tot}} \\ 0 & 0 \\ 0 & 0 \end{bmatrix}, \mathbf{B}_{TL,2} = \begin{bmatrix} -\frac{1}{L_{tot}} & 0 \\ 0 & -\frac{1}{L_{tot}} \\ 0 & 0 \\ 0 & 0 \end{bmatrix} \\ \mathbf{C}_{TL} &= \begin{bmatrix} 1 & 0 & 0 & 0 \\ 0 & 1 & 0 & 0 \end{bmatrix} \end{aligned}$$

The transfer function of a linear time-invariant system expressed in a state-space form having matrices $[\mathbf{A} \ \mathbf{B} \ \mathbf{C} \ \mathbf{D}]$ can be obtained using the equation $H(s) = \mathbf{C}(s\mathbf{I} - \mathbf{A})^{-1}\mathbf{B} + \mathbf{D}$. Taking into account that the series-compensated transmission line is a linear system where the terms of matrices in (4.3) are time-invariant, the transfer function for the transmission line can be expressed as

$$\mathbf{i}_t(s) = \mathbf{C}_{TL}(s\mathbf{I} - \mathbf{A}_{TL})^{-1} \mathbf{B}_{TL,1} \mathbf{v}_t(s) + \mathbf{C}_{TL}(s\mathbf{I} - \mathbf{A}_{TL})^{-1} \mathbf{B}_{TL,2} \mathbf{v}_b(s) \quad (4.4)$$

where

$$\mathbf{i}_t(s) = \begin{bmatrix} \dot{i}_{t,d}(s) \\ \dot{i}_{t,q}(s) \end{bmatrix}, \quad \mathbf{v}_t(s) = \begin{bmatrix} v_{t,d}(s) \\ v_{t,q}(s) \end{bmatrix}, \quad \mathbf{v}_b(s) = \begin{bmatrix} v_{b,d}(s) \\ v_{b,q}(s) \end{bmatrix}$$

The term “s” represents the Laplace variable. To extract the admittance relation of the transmission line looking into the grid, the transfer function matrix expressing the relation from $\mathbf{v}_t(s)$ to $\mathbf{i}_t(s)$ is considered as

$$\mathbf{i}_t(s) = \mathbf{Y}_{TL}(s) \mathbf{v}_t(s) \quad (4.5)$$

where

$$\mathbf{Y}_{TL}(s) = \begin{bmatrix} Y_{TL,dd}(s) & Y_{TL,dq}(s) \\ Y_{TL,qd}(s) & Y_{TL,qq}(s) \end{bmatrix} = \mathbf{C}_{TL}(s\mathbf{I} - \mathbf{A}_{TL})^{-1} \mathbf{B}_{TL,1} \mathbf{v}_t(s) \quad (4.6)$$

Further evaluating the terms for the matrix $\mathbf{Y}_{TL}(s)$, the series-compensated transmission line is a symmetric system with $Y_{TL,dd}(s) = Y_{TL,qq}(s)$ and $-Y_{TL,dq}(s) = Y_{TL,qd}(s)$ which can equivalently be described using complex transfer functions as [36]

$$\mathbf{Y}_{TL}(s) = Y_{TL,dd}(s) + jY_{TL,qd}(s) \quad (4.7)$$

To obtain the frequency response of the transfer function in (4.7), the variable “s” is replaced with $j\omega_n$ with ω_n representing the angular frequency range of interest. The resonance frequency for the transmission line based on $f_{res} = \sqrt{\frac{X_c}{X_{tot}}} f_s$ appears in the subsynchronous frequency range with f_s represents the synchronous frequency. In a dq frame that is rotating at the synchronous frequency, this would appear at $f_{res} - f_s$. As can be observed from Fig. 4.2 (left), showing the dq admittance of a series-compensated transmission line, the resonance appears at a negative frequency. This is to imply that a resonance in the subsynchronous frequency range appears as a negative sequence in the rotating dq -frame. However in the $\alpha\beta$ -frame, the response can be obtained through frequency shifting by substituting the variable “s” with $j(\omega - \omega_s)$ instead as in Fig. 4.2 (right)

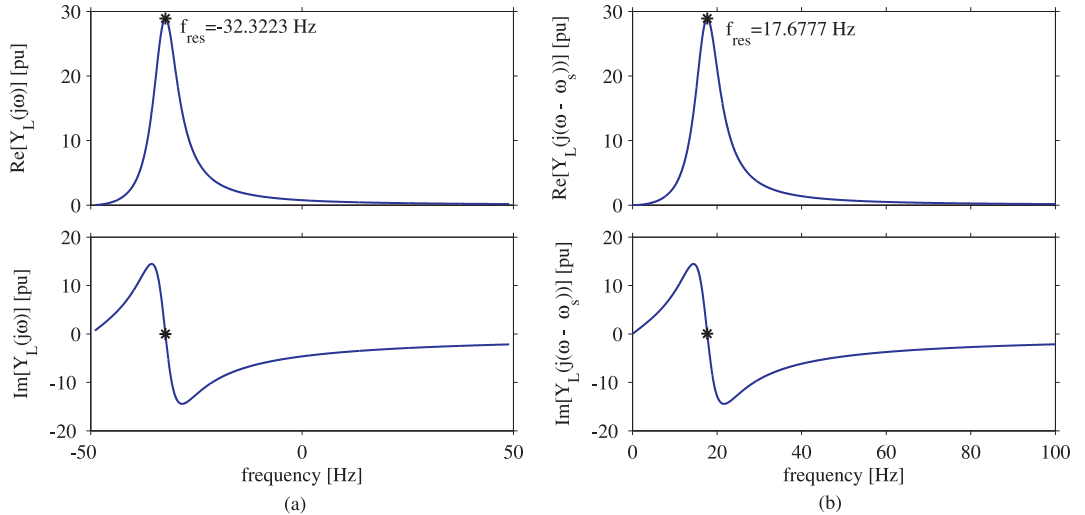


Fig. 4.2 Frequency response for dq admittance of a series compensation transmission line, 30% compensation (a) obtained substituting “s” with $j\omega$ (b) obtained substituting “s” with $j(\omega - \omega_s)$

4.4 DFIG admittance

The modeling approach consists of developing small subsystems which are connected to build the total system. The advantage with this approach is that, a complex system can be built through

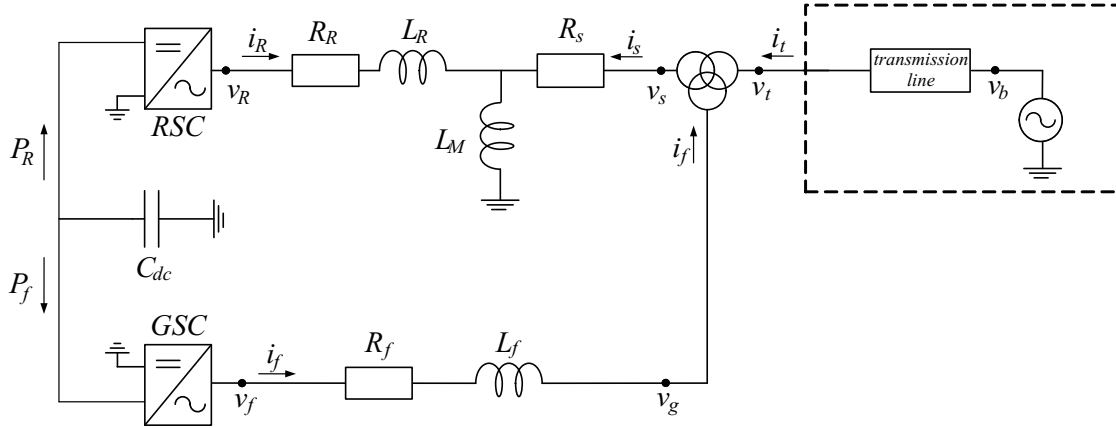


Fig. 4.3 Model of a DFIG turbine

a step-by-step interconnection of smaller subsystems. Moreover, the system is verified for each subsystem added which makes the debugging process less complicated. Another added advantage with this approach is the possibility of removing subsystems and analyzing the impact on the overall system. The DFIG is considered as an entire system built from smaller subsystems like the induction generator model, the RSC model, the GSC model and the dc-link dynamics model.

Fig. 4.3 shows the DFIG system to be modeled. In this section, the DFIG is considered to be connected to an infinite bus through a transmission line. The WRIG is represented in terms of resistances (R_s and R_R) and inductances (L_M and L_R). The ac-side of the RSC is connected directly to the rotor of WRIG whereas the dc-side is coupled to the dc-side of the GSC through the dc-link with a capacitance (C_{dc}). The ac-side of the GSC is coupled to the grid-side filter represented by a resistance (R_f) and an inductance (L_f).

First, the WRIG with the RSC current controller excluding the dc-link dynamics and the outer-loop controllers is derived. Next the subsystem consisting of the grid-side filter and the GSC current controller is developed. The two subsystems are cascaded to create a simplified model not including outer-loop controllers for the RSC and GSC is created. Following this, a subsystem comprising the outer power control loop for the RSC is developed. A final subsystem for the outer-loop controller for the GSC and the dc-link dynamics is derived. In the end, the two subsystems for the outer-loop controllers are cascaded with the simplified model to create the electrical model for the DFIG.

4.4.1 WRIG with rotor-side current controller

In this section, the WRIG together with the RSC current controller excluding outer-loop controllers and dc-link dynamics is derived. For the purpose of clarity, the stator and rotor voltage equations for the WRIG considering the Γ -representation in the dq -frame as described in (3.3) are repeated here.

$$\begin{aligned} \underline{v}_s^{(dq)} &= R_s \underline{i}_s^{(dq)} + \frac{d\underline{\Psi}_s^{(dq)}}{dt} + j\omega_s \underline{\Psi}_s^{(dq)} \\ \underline{v}_R^{(dq)} &= R_R \underline{i}_R^{(dq)} + \frac{d\underline{\Psi}_R^{(dq)}}{dt} + j\omega_2 \underline{\Psi}_R^{(dq)} \end{aligned} \quad (4.8)$$

Expressing the stator and rotor flux expressions using \underline{i}_s and \underline{i}_R , (4.8) is expressed as

$$\begin{aligned} \underline{v}_s^{(dq)} &= R_s \underline{i}_s^{(dq)} + L_M \frac{d\underline{i}_s^{(dq)}}{dt} + L_M \frac{d\underline{i}_R^{(dq)}}{dt} + j\omega_s L_M \underline{i}_s^{(dq)} + j\omega_s L_M \underline{i}_R^{(dq)} \\ \underline{v}_R^{(dq)} &= R_R \underline{i}_R^{(dq)} + L_M \frac{d\underline{i}_s^{(dq)}}{dt} + (L_M + L_R) \frac{d\underline{i}_R^{(dq)}}{dt} + j\omega_2 L_M \underline{i}_s^{(dq)} + j\omega_2 (L_M + L_R) \underline{i}_R^{(dq)} \end{aligned} \quad (4.9)$$

The above expression governing the WRIG can be expressed in the Laplace domain as

$$\begin{aligned} \underline{v}_s^{(dq)}(s) &= (R_s + sL_M + j\omega_s L_M) \underline{i}_s^{(dq)}(s) + (sL_M + j\omega_s L_M) \underline{i}_R^{(dq)}(s) \\ \underline{v}_R^{(dq)}(s) &= (sL_M + j\omega_2 L_M) \underline{i}_s^{(dq)}(s) + (R_R + s(L_M + L_R) + j\omega_2 (L_M + L_R)) \underline{i}_R^{(dq)}(s) \end{aligned} \quad (4.10)$$

Using (4.10), the WRIG can be expressed in a matrix form in terms of stator and rotor currents, input rotor voltage and input stator voltage as

$$\mathbf{M}_g \mathbf{i}_g = \mathbf{M}_R \mathbf{v}_R + \mathbf{M}_s \mathbf{v}_s \quad (4.11)$$

where

$$\begin{aligned} \mathbf{i}_g &= \begin{bmatrix} \mathbf{i}_s \\ \mathbf{i}_R \end{bmatrix}, \quad \mathbf{i}_s = \begin{bmatrix} i_{s,d}(s) \\ i_{s,q}(s) \end{bmatrix}, \quad \mathbf{i}_R = \begin{bmatrix} i_{R,d}(s) \\ i_{R,q}(s) \end{bmatrix}, \quad \mathbf{v}_R = \begin{bmatrix} v_{R,d}(s) \\ v_{R,q}(s) \end{bmatrix}, \quad \mathbf{v}_s = \begin{bmatrix} v_{s,d}(s) \\ v_{s,q}(s) \end{bmatrix} \\ \mathbf{M}_g &= \begin{bmatrix} R_s + sL_M & -\omega_s L_M & sL_M & -\omega_s L_M \\ \omega_s L_M & R_s + sL_M & \omega_s L_M & sL_M \\ sL_M & -\omega_2 L_M & R_R + s(L_M + L_R) & -\omega_2 (L_M + L_R) \\ \omega_2 L_M & sL_M & \omega_2 (L_M + L_R) & R_R + s(L_M + L_R) \end{bmatrix} \\ \mathbf{M}_R &= \begin{bmatrix} 0 & 0 \\ 0 & 0 \\ 1 & 0 \\ 0 & 1 \end{bmatrix}, \quad \mathbf{M}_s = \begin{bmatrix} 1 & 0 \\ 0 & 1 \\ 0 & 0 \\ 0 & 0 \end{bmatrix} \end{aligned}$$

In this chapter, variables with bold letter are used to represent both matrices and vectors. In Subsection 3.3.1, the derivation of the RSC current controller was presented. The reference rotor voltage generated by the RSC current controller shown in (3.24) is repeated here.

$$\underline{v}_R^{*(dq)}(s) = F_{cc,R}(s) \left(\underline{i}_R^{*(dq)}(s) - \underline{i}_R^{(dq)}(s) \right) + j\omega_2 L_R \underline{i}_R^{(dq)}(s) + H_{LP}(s) \underline{\hat{e}}_{emf}^{(dq)}(s) \quad (4.12)$$

Chapter 4. System Admittance Modeling

where the estimated back EMF term is $\hat{e}_{emf}^{(dq)}(s) = v_s(s) - \left(\frac{R_s}{L_M} + j\omega_r\right) \hat{\Psi}_s^{(dq)}$ and the low-pass filter term as $H_{LP}(s) = \frac{\alpha_{LP}}{s + \alpha_{LP}}$. The transfer function $F_{cc,R}(s)$ is a proportional controller with the term $k_{p,cc} = \alpha_{cc,R}L_R$. Under the assumption that the RSC converter is treated as a set of linear amplifiers and are able to generate the reference voltages with no delay, the rotor voltage vector \mathbf{v}_R in (4.11) can be expressed as

$$\mathbf{v}_R = \mathbf{v}_R^* \quad (4.13)$$

$$\mathbf{v}_R^* = \begin{bmatrix} v_{R,d}^*(s) \\ v_{R,q}^*(s) \end{bmatrix} = \mathbf{F}_{cc,R} \mathbf{i}_R^* + \mathbf{M}_{cc,R} \mathbf{i}_g + \mathbf{M}_{cc,v} \mathbf{v}_s$$

where

$$\mathbf{F}_{cc,R} = \begin{bmatrix} F_{cc,R}(s) & 0 \\ 0 & F_{cc,R}(s) \end{bmatrix}, \quad \mathbf{M}_{cc,v} = \begin{bmatrix} H_{LP}(s) & 0 \\ 0 & H_{LP}(s) \end{bmatrix}, \quad \mathbf{i}_R^* = \begin{bmatrix} i_{R,d}^*(s) \\ i_{R,q}^*(s) \end{bmatrix}$$

$$\mathbf{M}_{cc,R} = \begin{bmatrix} -R_s H_{LP}(s) & \omega_r L_M H_{LP}(s) & -F_{cc,R}(s) & -(\omega_2 L_R - \omega_r L_M H_{LP}(s)) \\ -\omega_r L_M H_{LP}(s) & -R_s H_{LP}(s) & (\omega_2 L_R - \omega_r L_M H_{LP}(s)) & -F_{cc,R}(s) \end{bmatrix}$$

In (4.11), a representation of a WRIG using the Γ -representation has been formulated in terms of input voltages, stator and rotor currents. Following this, taking the expression of voltage generated by the rotor-side converter (i.e. neglecting the outer-controllers), a representation for the rotor-side current controller is obtained as (4.13). As the output voltage from the rotor-side converter serves as an input to the WRIG rotor, combining (4.11) and (4.13) results in a system representation in terms of currents, reference values and input voltages as

$$\mathbf{M}_{gcc,i} \mathbf{i}_g = \mathbf{M}_{gcc,ref} \mathbf{i}_R^* + \mathbf{M}_{gcc,v} \mathbf{v}_s \quad (4.14)$$

with matrices $\mathbf{M}_{gcc,i}$, $\mathbf{M}_{gcc,ref}$ and $\mathbf{M}_{gcc,v}$ expressed as

$$\mathbf{M}_{gcc,i} = \mathbf{M}_g - \mathbf{M}_R \mathbf{M}_{cc,R}$$

$$\mathbf{M}_{gcc,ref} = \mathbf{M}_R \mathbf{F}_{cc,R}$$

$$\mathbf{M}_{gcc,v} = \mathbf{M}_R \mathbf{M}_{cc,v} + \mathbf{M}_s$$

The losses and phase shift due to the three-winding transformer (see Fig. 4.3) is assumed to be negligible and therefore not considered during the modeling. However, the transformation ratio between the different side is accounted for. As there is a one to one ratio between the stator-side and terminal-side of the DFIG, the stator voltage vector (\mathbf{v}_s) can be replaced by DFIG terminal voltage (\mathbf{v}_t) resulting in

$$\mathbf{M}_{gcc,i} \mathbf{i}_g = \mathbf{M}_{gcc,ref} \mathbf{i}_R^* + \mathbf{M}_{gcc,v} \mathbf{v}_t \quad (4.15)$$

At an early stage, the admittance of WRIG with the rotor current controller can be obtained by rearranging (4.15) into a form corresponding to

$$\mathbf{i}_g = \begin{bmatrix} \mathbf{i}_s \\ \mathbf{i}_R \end{bmatrix} = \begin{bmatrix} \mathbf{G}_{gccs,ref} \\ \mathbf{G}_{gccR,ref} \end{bmatrix} \mathbf{i}_R^* + \begin{bmatrix} \mathbf{Y}_{gcc} \\ \mathbf{Y}_{gccR} \end{bmatrix} \mathbf{v}_t \quad (4.16)$$

with

$$\begin{bmatrix} \mathbf{G}_{gccs,ref} \\ \mathbf{G}_{gccR,ref} \end{bmatrix} = [\mathbf{M}_{gcc,i}]^{-1} \mathbf{M}_{gcc,ref} \quad \text{and} \quad \begin{bmatrix} \mathbf{Y}_{gcc} \\ \mathbf{Y}_{gccR} \end{bmatrix} = [\mathbf{M}_{gcc,i}]^{-1} \mathbf{M}_{gcc,v}$$

$\mathbf{G}_{gccs,ref}$, $\mathbf{G}_{gccR,ref}$, \mathbf{Y}_{gcc} and \mathbf{Y}_{gccR} are 2×2 transfer function matrices. \mathbf{Y}_{gcc} expressing the relation from terminal voltage vector (\mathbf{v}_t) to stator current vector (\mathbf{i}_s) is considered as the admittance matrix which is expressed explicitly as

$$\begin{bmatrix} i_{s,d}(s) \\ i_{s,q}(s) \end{bmatrix} = \begin{bmatrix} \mathbf{Y}_{gcc}(1,1) & \mathbf{Y}_{gcc}(1,2) \\ \mathbf{Y}_{gcc}(2,1) & \mathbf{Y}_{gcc}(2,2) \end{bmatrix} \begin{bmatrix} v_{t,d}(s) \\ v_{t,q}(s) \end{bmatrix} \quad (4.17)$$

The combined system constituting the WRIG and the rotor-side current controller is symmetric in nature as the system is identical both along the d and q axis. Hence the admittance can equivalently be expressed using complex transfer function as [36]

$$\underline{Y}_{gcc}(s) = \mathbf{Y}_{gcc}(1,1) + j\mathbf{Y}_{gcc}(2,1) \quad (4.18)$$

The admittance of a WRIG with current controller in the subsynchronous frequency range obtained by evaluating the frequency response of (4.18) is depicted in Fig. 4.4. The admittance is normalized by the rated power and voltage for the DFIG. The admittance of a WRIG with the rotor circuit connected to a rotor-side current controller by itself does not give much insight into the behavior of the DFIG turbine but instead will serve as a building block for total DFIG admittance.

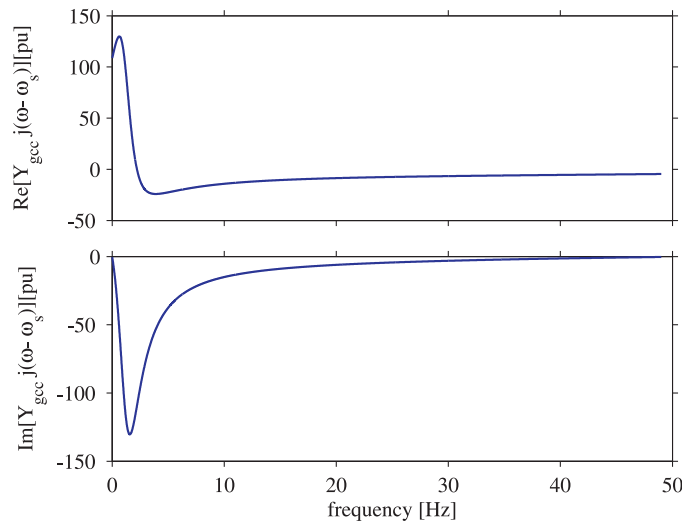


Fig. 4.4 Admittance of WRIG in series with the RSC connected to the rotor terminal only considering the inner-current controller, closed-loop current controller bandwidth of 1 pu

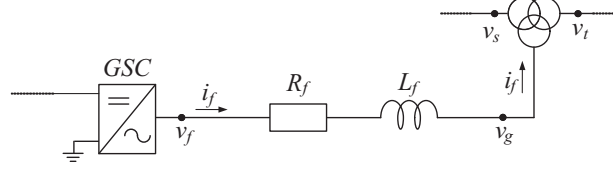


Fig. 4.5 Grid-side filter connected to GSC

4.4.2 Grid-side filter with GSC current controller

In this section, the grid-side filter together with the GSC current controller as a stand-alone shunt device is considered. Figure. 4.5 shows a portion of Fig. 4.3 with the grid-side filter connected to the GSC. The outer dc-link controller for the GSC is neglected in this subsection and will be connected as an added subsystem in the coming subsection.

In reference to Fig. 4.5, the voltage v_f at the terminal of the GSC in the Laplace domain can be expressed as

$$\underline{v}_f^{(dq)}(s) = (R_f + sL_f)\underline{i}_f^{(dq)}(s) + j\omega_s L_f \underline{i}_f^{(dq)}(s) + \underline{v}_g^{(dq)}(s) \quad (4.19)$$

The expression for the GSC current controller as described in (3.28) is repeated here.

$$\underline{v}_f^{*(dq)}(s) = F_{cc,f}(s) \left(\underline{i}_f^{*(dq)}(s) - \underline{i}_f^{(dq)}(s) \right) + j\omega_s L_f \underline{i}_f^{(dq)}(s) + H_{LP}(s) \underline{v}_g^{(dq)}(s) \quad (4.20)$$

$F_{cc,f}(s) = k_{pf,cc} + \frac{k_{if,cc}}{s}$ is a PI controller with $k_{pf,cc} = \alpha_{cc,f} L_f$ and $k_{if,cc} = \alpha_{cc,f} R_f$. Again assuming $\underline{v}_f^{(dq)} = \underline{v}_f^{*(dq)}$, (4.19) and (4.20) can be expressed as

$$\mathbf{M}_{fcc,i} \mathbf{i}_f = \mathbf{M}_{fcc,ref} \mathbf{i}_f^* + \mathbf{M}_{fcc,vg} \mathbf{v}_g \quad (4.21)$$

where

$$\mathbf{i}_f = \begin{bmatrix} i_{f,d}(s) \\ i_{f,q}(s) \end{bmatrix}, \mathbf{i}_f^* = \begin{bmatrix} i_{f,d}^*(s) \\ i_{f,q}^*(s) \end{bmatrix}, \mathbf{v}_g = \begin{bmatrix} v_{g,d}(s) \\ v_{g,q}(s) \end{bmatrix}$$

$$\mathbf{M}_{fcc,i} = \begin{bmatrix} R_f + sL_f + F_{cc,f}(s) & 0 \\ 0 & R_f + sL_f + F_{cc,f}(s) \end{bmatrix}$$

$$\mathbf{M}_{fcc,ref} = \begin{bmatrix} F_{cc,f}(s) & 0 \\ 0 & F_{cc,f}(s) \end{bmatrix}, \mathbf{M}_{fcc,vg} = \begin{bmatrix} H_{LP}(s) - 1 & 0 \\ 0 & H_{LP}(s) - 1 \end{bmatrix}$$

In the same manner as in the previous subsection, the losses and phase-shift due to the three-winding transformer is neglected. However considering the transformer's ratio (k_{tr}) between the grid-filter side and the generator terminal side (see Fig. 4.5), the voltage vector \mathbf{v}_g can be expressed as

$$\mathbf{v}_g = k_{tr} \mathbf{v}_t \quad (4.22)$$

Inserting (4.22) into (4.21), a subsystem representation of the grid-side filter connected to the GSC with a current controller in terms of the terminal input voltage, the actual and reference filter currents is given by

$$\mathbf{M}_{fcc,i}\mathbf{i}_f = \mathbf{M}_{fcc,ref}\mathbf{i}_f^* + \mathbf{M}_{fcc,v}\mathbf{v}_t \quad (4.23)$$

with

$$\mathbf{M}_{fcc,v} = k_{tr}\mathbf{M}_{fcc,vg}$$

4.4.3 Combined WRIG, RSC and GSC current controllers

In Subsections 4.4.1, the WRIG together with rotor-side current controller has been expressed as a single subsystem having terminal voltage (\mathbf{v}_t) and rotor current reference (\mathbf{i}_R^*) as input and currents as outputs (refer to equation (4.15)). Similarly, in Subsection 4.4.2, the grid-side filter along with the GSC current controller has been described using transfer function matrices having terminal voltage (\mathbf{v}_t) and filter current reference (\mathbf{i}_f^*) as input is shown in (4.23). Combining the two subsystems, a simplified DFIG model neglecting the outer-loop controllers both for the RSC and GSC can be obtained. Using (4.15) and (4.23), the cascaded system is expressed as

$$\mathbf{M}_{grcc,i}\mathbf{i} = \mathbf{M}_{grcc,ref}\mathbf{i}_{ref}^* + \mathbf{M}_{grcc,v}\mathbf{v}_t \quad (4.24)$$

with

$$\mathbf{M}_{grcc,i} = \begin{bmatrix} \mathbf{M}_{gcc,i} & \mathbf{P}_1 \\ \mathbf{P}_1^T & \mathbf{M}_{fcc,i} \end{bmatrix}, \quad \mathbf{M}_{grcc,ref} = \begin{bmatrix} \mathbf{M}_{gcc,ref} & \mathbf{P}_1 \\ \mathbf{P}_2 & \mathbf{M}_{fcc,ref} \end{bmatrix}$$

$$\mathbf{M}_{grcc,v} = \begin{bmatrix} \mathbf{M}_{gcc,v} \\ \mathbf{M}_{fcc,v} \end{bmatrix}, \quad \mathbf{i} = \begin{bmatrix} \mathbf{i}_g \\ \mathbf{i}_f \end{bmatrix} = \begin{bmatrix} \mathbf{i}_s \\ \mathbf{i}_R \\ \mathbf{i}_f \end{bmatrix}, \quad \mathbf{i}_{ref}^* = \begin{bmatrix} \mathbf{i}_R^* \\ \mathbf{i}_f^* \end{bmatrix}$$

$$\mathbf{P}_1 = \mathbf{zeros}[4 \times 2], \quad \mathbf{P}_2 = \mathbf{zeros}[2 \times 2]$$

In a similar manner, the expression in (4.24) can be rearranged to generate admittance and reference matrices as

$$\mathbf{i} = \mathbf{G}_{grcc}\mathbf{i}_{ref}^* + \mathbf{Y}_{grcc}\mathbf{v}_t \quad (4.25)$$

with matrices \mathbf{G}_{grcc} and \mathbf{Y}_{grcc} expressed as

$$\mathbf{G}_{grcc} = \mathbf{M}_{grcc,i}^{-1}\mathbf{M}_{grcc,ref} = \begin{bmatrix} \mathbf{G}_{grcc,is}^{iRref} & \mathbf{P}_2 \\ \mathbf{G}_{grcc,iR}^{iRref} & \mathbf{P}_2 \\ \mathbf{P}_2 & \mathbf{G}_{grcc,if}^{ifref} \end{bmatrix} \quad (4.26)$$

$$\mathbf{Y}_{grcc} = \mathbf{M}_{grcc,i}^{-1}\mathbf{M}_{grcc,v} = \begin{bmatrix} \mathbf{Y}_{grcc,is} \\ \mathbf{Y}_{grcc,iR} \\ \mathbf{Y}_{grcc,if} \end{bmatrix}$$

Chapter 4. System Admittance Modeling

$\mathbf{G}_{grcc, is}^{iRref}$ is a 2x2 transfer function matrix expressing the relation from $\underline{i}_R^{*(dq)}$ to $\underline{i}_s^{(dq)}$ where as $\mathbf{G}_{grcc, iR}^{iRref}$ is a transfer function matrix of the same size expressing the relation from $\underline{i}_R^{*(dq)}$ to $\underline{i}_R^{(dq)}$. $\mathbf{G}_{grcc, if}^{ifref}$ express the transfer function relation from $\underline{i}_f^{*(dq)}$ to $\underline{i}_f^{(dq)}$. $\mathbf{Y}_{grcc, is}$ represent the transfer function matrix from terminal voltage ($v_t^{(dq)}$) to stator current ($\underline{i}_s^{(dq)}$) whereas $\mathbf{Y}_{grcc, if}$ is the transfer function matrix from terminal voltage ($v_t^{(dq)}$) to filter current ($\underline{i}_f^{(dq)}$). Observing (4.25), the system with WRIG, RSC current controller and the GSC current controller is represented in a transfer function matrix form explicitly defined as matrices affecting the reference term and matrices affecting the admittance term. In the subsections that follow, the subsystems expressing the outer-loop controllers both for the RSC and GSC thereby incorporating the dc-link dynamics is derived. These are then cascaded to obtain the overall mathematical expression for the DFIG.

4.4.4 Active and reactive power controllers

In previous subsections, a simplified mathematical representation of the DFIG neglecting outer controller loops have been covered. In this subsection, the outer-loop controller for the RSC is derived. The outer control-loops as discussed in Chapter 3 is based on a PI controller which controls the terminal active and reactive power of the DFIG. For the convenience of the reader, the expression for the controller are repeated.

$$\begin{aligned} i_{R,d}^*(s) &= F_{Qc} (Q_{out}^* - H_{LP,Q} Q_{out}) \\ i_{R,q}^*(s) &= F_{Pc} (P_{out}^* - H_{LP,p} P_{out}) \end{aligned} \quad (4.27)$$

where

$$F_{Pc} = k_{p,p} \left(1 + \frac{1}{sT_{i,p}} \right), \quad F_{Qc} = k_{p,Q} \left(1 + \frac{1}{sT_{i,Q}} \right), \quad H_{LP,p} = H_{LP,Q} = \frac{\alpha_{LP,p}}{s + \alpha_{LP,p}}$$

The expression for the terminal powers, P_{out} and Q_{out} are

$$\begin{aligned} P_{out} &= 3 (-v_{s,d} i_{s,d} - v_{s,q} i_{s,q} + v_{g,d} i_{f,d} + v_{g,q} i_{f,q}) \\ Q_{out} &= 3 (v_{s,d} i_{s,q} - v_{s,q} i_{s,d} - v_{g,d} i_{f,q} + v_{g,q} i_{f,d}) \end{aligned} \quad (4.28)$$

It should be noted that the inclusion of the power controller caused the system to be non-linear as (4.28) is non-linear. Hence, (4.27) can be linearized as

$$\begin{aligned} \Delta i_{R,d}^* &= F_{Qc} (\Delta Q_{out}^* - H_{LP,Q} \Delta Q_{out}) \\ \Delta i_{R,q}^* &= F_{Pc} (\Delta P_{out}^* - H_{LP,p} \Delta P_{out}) \end{aligned} \quad (4.29)$$

here represented using transfer function matrices as

$$\begin{bmatrix} \Delta i_{R,d}^* \\ \Delta i_{R,q}^* \end{bmatrix} = \mathbf{F}_{PQc} \begin{bmatrix} \Delta P_{out}^* \\ \Delta Q_{out}^* \end{bmatrix} - \mathbf{F}_{PQc} H_{LP,p} \begin{bmatrix} \Delta P_{out} \\ \Delta Q_{out} \end{bmatrix} \quad (4.30)$$

with

$$\mathbf{F}_{PQc} = \begin{bmatrix} 0 & F_{Qc} \\ F_{Pc} & 0 \end{bmatrix}$$

Linearization of the power expression in (4.28) results in

$$\begin{aligned} \begin{bmatrix} \Delta P_{out} \\ \Delta Q_{out} \end{bmatrix} &= \underbrace{\begin{bmatrix} -3v_{s,d0} & -3v_{s,q0} \\ -3v_{s,q0} & 3v_{s,d0} \end{bmatrix}}_{\mathbf{M}_{PQ,is}} \begin{bmatrix} \Delta i_{s,d} \\ \Delta i_{s,q} \end{bmatrix} + \underbrace{\begin{bmatrix} 3v_{g,d0} & 3v_{g,q0} \\ 3v_{g,q0} & -3v_{g,d0} \end{bmatrix}}_{\mathbf{M}_{PQ,if}} \begin{bmatrix} \Delta i_{f,d} \\ \Delta i_{f,q} \end{bmatrix} \\ &+ \underbrace{\begin{bmatrix} -3i_{s,d0} & -3i_{s,q0} \\ 3i_{s,q0} & -3i_{s,d0} \end{bmatrix}}_{\mathbf{M}_{PQ,vs}} \begin{bmatrix} \Delta v_{s,d} \\ \Delta v_{s,q} \end{bmatrix} + \underbrace{\begin{bmatrix} 3i_{f,d0} & 3i_{f,q0} \\ -3i_{f,q0} & 3i_{f,d0} \end{bmatrix}}_{\mathbf{M}_{PQ,vg}} \begin{bmatrix} \Delta v_{g,d} \\ \Delta v_{g,q} \end{bmatrix} \quad (4.31) \\ \begin{bmatrix} \Delta P_{out} \\ \Delta Q_{out} \end{bmatrix} &= \mathbf{M}_{PQ,is} \begin{bmatrix} \Delta i_{s,d} \\ \Delta i_{s,q} \end{bmatrix} + \mathbf{M}_{PQ,if} \begin{bmatrix} \Delta i_{f,d} \\ \Delta i_{f,q} \end{bmatrix} + \mathbf{M}_{PQ,v} \begin{bmatrix} \Delta v_{t,d} \\ \Delta v_{t,q} \end{bmatrix} \end{aligned}$$

where

$$\mathbf{M}_{PQ,v} = \mathbf{M}_{PQ,vs} + k_{tr}\mathbf{M}_{PQ,vg}$$

The “0” in the subscript indicates initial conditions. Expression (4.31) can be conveniently expressed as

$$\begin{bmatrix} \Delta P_{out} \\ \Delta Q_{out} \end{bmatrix} = \underbrace{\begin{bmatrix} \mathbf{M}_{PQ,is} & \mathbf{P}_2 & \mathbf{M}_{PQ,if} \end{bmatrix}}_{\mathbf{M}_{PQ,i}} \Delta \mathbf{i} + \mathbf{M}_{PQ,v} \begin{bmatrix} \Delta v_{t,d} \\ \Delta v_{t,q} \end{bmatrix} \quad (4.32)$$

with

$$\Delta \mathbf{i} = \begin{bmatrix} \Delta i_{s,d} & \Delta i_{s,q} & \Delta i_{R,d} & \Delta i_{R,q} & \Delta i_{f,d} & \Delta i_{f,q} \end{bmatrix}^T$$

Equation (4.30) and (4.32) can be combined to generate the expression for the reference rotor currents $\begin{bmatrix} \Delta i_{R,d}^* \\ \Delta i_{R,q}^* \end{bmatrix}$ as

$$\begin{bmatrix} \Delta i_{R,d}^* \\ \Delta i_{R,q}^* \end{bmatrix} = \mathbf{F}_{PQc} \begin{bmatrix} \Delta P_{out}^* \\ \Delta Q_{out}^* \end{bmatrix} - \mathbf{F}_{PQc} H_{LP,p} \mathbf{M}_{PQ,i} \Delta \mathbf{i} - \mathbf{F}_{PQc} H_{LP,p} \mathbf{M}_{PQ,v} \begin{bmatrix} \Delta v_{t,d} \\ \Delta v_{t,q} \end{bmatrix} \quad (4.33)$$

Even with the numerous expression derived so far, the coupling between the subsystem constituting the WRIG and RSC, and the subsystem constituting the grid-side filter and GSC is not accomplished. The RSC and GSC are electrically coupled through the dc-link capacitor. Hence the incorporation of the dc-link dynamics together with the implemented dc-link voltage controller is a crucial step. The next subsection is delegated to generate a subsystem representing the dc-link dynamics and the dc-link voltage controller.

4.4.5 DC-link voltage controller

Recalling the dc-link voltage controller that acts on q -component of the filter current, the control equation in (3.39) can be rewritten as

$$i_{f,q}^* = F_{dc} (U_{dc}^{*2} - U_{dc}^2) + G_a U_{dc}^2 \quad (4.34)$$

with

$$F_{dc} = k_{p,dc} + \frac{k_{i,dc}}{s}$$

with $k_{p,dc}$ and $k_{i,dc}$ as described in (3.37). Linearization around a steady-state operating point leads to

$$\Delta i_{f,q}^* = 2U_{dc0}^* F_{dc} \Delta U_{dc}^* + 2U_{dc0} (G_a - F_{dc}) \Delta U_{dc} \quad (4.35)$$

To obtain the expression for ΔU_{dc} , the dynamics of the dc-link capacitor is considered. The dc-link capacitor dynamics as described in Chapter 3 can be expressed in terms of the active power exchange between the RSC and the GSC. Under the assumption that both the RSC and GSC converter are ideal meaning that the power on the dc-side is considered equivalent to the power on the ac-side, the expression for the dc-link capacitor can be written as

$$\frac{1}{2} C_{dc} \frac{dU_{dc}^2}{dt} = -P_f - P_R \quad (4.36)$$

Linearization of the above expression and transformation to Laplace domain results in

$$\Delta U_{dc} = \frac{-\Delta P_f - \Delta P_R}{C_{dc} U_{dc0} s} \quad (4.37)$$

The expression for $\Delta i_{f,q}^*$ in (4.35) can now be combined with (4.37) to obtain

$$\Delta i_{f,q}^* = m_{dcref} \Delta U_{dc}^* + m_p (\Delta P_f + \Delta P_R) \quad (4.38)$$

where

$$m_{dcref} = 2U_{dc0}^* F_{dc}, \quad m_p = \frac{2(F_{dc} - G_a)}{C_{dc} s}$$

To further expand (4.38), linearized expression for power flowing into RSC and GSC are required. The active power flow from the GSC, using small signal, can be expressed as

$$\Delta P_f = \begin{bmatrix} 3v_{f,d0} & 3v_{f,q0} \end{bmatrix} \begin{bmatrix} \Delta i_{f,d} \\ \Delta i_{f,q} \end{bmatrix} + \begin{bmatrix} 3i_{f,d0} & 3i_{f,q0} \end{bmatrix} \begin{bmatrix} \Delta v_{f,d} \\ \Delta v_{f,q} \end{bmatrix} \quad (4.39)$$

4.4. DFIG admittance

The expression for the voltage (v_f) at the terminal of the GSC (under the assumptions considered) can be extracted from (4.20) as

$$\begin{bmatrix} \Delta v_{f,d} \\ \Delta v_{f,q} \end{bmatrix} = \mathbf{M}_{fcc,ref} \begin{bmatrix} \Delta i_{f,d}^* \\ \Delta i_{f,q}^* \end{bmatrix} + \begin{bmatrix} -F_{cc,f} & -\omega_s L_f \\ \omega_s L_f & -F_{cc,f} \end{bmatrix} \Delta \mathbf{i}_f + \begin{bmatrix} k_{tr} H_{LP} & 0 \\ 0 & k_{tr} H_{LP} \end{bmatrix} \Delta \mathbf{v}_t \quad (4.40)$$

Combining (4.39) and (4.40), the linearized expression for ΔP_f can be rewritten as

$$\Delta P_f = \mathbf{M}_{Pfref} \begin{bmatrix} \Delta i_{f,d}^* \\ \Delta i_{f,q}^* \end{bmatrix} + \mathbf{M}_{Pfif} \Delta \mathbf{i}_f + \mathbf{M}_{Pfv} \Delta \mathbf{v}_t \quad (4.41)$$

where

$$\begin{aligned} \mathbf{M}_{Pfref} &= \begin{bmatrix} 3i_{f,d0} & 3i_{f,q0} \end{bmatrix} \mathbf{M}_{fcc,ref} \\ \mathbf{M}_{Pfif} &= \begin{bmatrix} 3v_{f,d0} & 3v_{f,q0} \end{bmatrix} + \begin{bmatrix} 3i_{f,d0} & 3i_{f,q0} \end{bmatrix} \begin{bmatrix} -F_{cc,f} & -\omega_s L_f \\ \omega_s L_f & -F_{cc,f} \end{bmatrix} \\ \mathbf{M}_{Pfv} &= \begin{bmatrix} 3i_{f,d0} & 3i_{f,q0} \end{bmatrix} \begin{bmatrix} k_{tr} H_{LP} & 0 \\ 0 & k_{tr} H_{LP} \end{bmatrix} \end{aligned}$$

The linearized expression for the power flowing out of the RSC can be expressed as

$$\Delta P_R = \begin{bmatrix} 3v_{R,d0} & 3v_{R,q0} \end{bmatrix} \begin{bmatrix} \Delta i_{R,d} \\ \Delta i_{R,q} \end{bmatrix} + \begin{bmatrix} 3i_{R,d0} & 3i_{R,q0} \end{bmatrix} \begin{bmatrix} \Delta v_{R,d} \\ \Delta v_{R,q} \end{bmatrix} \quad (4.42)$$

Since the expression for \mathbf{v}_R in (4.13) is linear, $\begin{bmatrix} \Delta v_{R,d} \\ \Delta v_{R,q} \end{bmatrix}$ can be obtained from the same expression as

$$\begin{bmatrix} \Delta v_{R,d} \\ \Delta v_{R,q} \end{bmatrix} = \mathbf{F}_{cc,R} \begin{bmatrix} \Delta i_{R,d}^* \\ \Delta i_{R,q}^* \end{bmatrix} + \mathbf{M}_{cc,R} \Delta \mathbf{i}_g + \mathbf{M}_{cc,v} \Delta \mathbf{v}_t \quad (4.43)$$

The combination of (4.42) and (4.43) results in

$$\Delta P_R = \mathbf{M}_{PRref} \begin{bmatrix} \Delta i_{R,d}^* \\ \Delta i_{R,q}^* \end{bmatrix} + \mathbf{M}_{PRig} \Delta \mathbf{i}_g + \mathbf{M}_{PRv} \Delta \mathbf{v}_t \quad (4.44)$$

where

$$\begin{aligned} \mathbf{M}_{PRref} &= \begin{bmatrix} 3i_{R,d0} & 3i_{R,q0} \end{bmatrix} \mathbf{F}_{cc,R} \\ \mathbf{M}_{PRig} &= \begin{bmatrix} 3i_{R,d0} & 3i_{R,q0} \end{bmatrix} \mathbf{M}_{cc,R} + \begin{bmatrix} 0 & 0 & 3v_{R,d0} & 3v_{R,q0} \end{bmatrix} \\ \mathbf{M}_{PRv} &= \begin{bmatrix} 3i_{R,d0} & 3i_{R,q0} \end{bmatrix} \mathbf{M}_{cc,v} \end{aligned}$$

The expression for ΔP_R in (4.44) in combination with the expression for $\begin{bmatrix} \Delta i_{R,d}^* \\ \Delta i_{R,q}^* \end{bmatrix}$ in (4.33) and ΔP_f in (4.41) can be manipulated to obtain

$$\Delta P_f + \Delta P_R = \mathbf{M}_{Pfref} \begin{bmatrix} \Delta i_{f,d}^* \\ \Delta i_{f,q}^* \end{bmatrix} + \mathbf{M}_{PRref} \mathbf{F}_{PQC} \begin{bmatrix} \Delta P_{out}^* \\ \Delta Q_{out}^* \end{bmatrix} + \mathbf{M}_{ifrefi} \Delta \mathbf{i} + \mathbf{M}_{ifrefv} \Delta \mathbf{v}_t \quad (4.45)$$

Chapter 4. System Admittance Modeling

where

$$\begin{aligned}\mathbf{M}_{ifrefi} &= [\mathbf{M}_{PRig} \quad \mathbf{M}_{Pfi}] - \mathbf{M}_{PRref} \mathbf{F}_{PQc} \mathbf{H}_{LP,p} \mathbf{M}_{PQ,i} \\ \mathbf{M}_{ifrefv} &= \mathbf{M}_{PRv} + \mathbf{M}_{Pfv} - \mathbf{M}_{PRref} \mathbf{F}_{PQc} \mathbf{H}_{LP,p} \mathbf{M}_{PQ,v}\end{aligned}$$

Inserting (4.45) into (4.38) results in

$$\begin{aligned}\Delta \mathbf{i}_{f,q}^* &= m_{dcref} \Delta U_{dc}^* + m_p \mathbf{M}_{Pfref} \begin{bmatrix} \Delta i_{f,d}^* \\ \Delta i_{f,q}^* \end{bmatrix} + m_p \mathbf{M}_{PRref} \mathbf{F}_{PQc} \begin{bmatrix} \Delta P_{out}^* \\ \Delta Q_{out}^* \end{bmatrix} \\ &+ m_p \mathbf{M}_{ifrefi} \Delta \mathbf{i} + m_p \mathbf{M}_{ifrefv} \Delta \mathbf{v}_t\end{aligned}\quad (4.46)$$

As it was presented in Chapter 3, the d -component of the filter current is controlled to zero by setting the reference value to zero. However for the ease of matrix manipulation, the expression for the reference d -component is here described as

$$\Delta i_{f,d}^* = \Delta i'_{f,d} \quad (4.47)$$

Combining (4.46) and (4.47) results in

$$\begin{aligned}\begin{bmatrix} \Delta i_{f,d}^* \\ \Delta i_{f,q}^* \end{bmatrix} &= \underbrace{\begin{bmatrix} 1 & 0 \\ 0 & m_{dcref} \end{bmatrix}}_{\mathbf{M}_{dcref}} \begin{bmatrix} \Delta i'_{f,d} \\ \Delta U_{dc}^* \end{bmatrix} + \underbrace{\begin{bmatrix} \mathbf{P}_3 \\ m_p \mathbf{M}_{Pfref} \end{bmatrix}}_{\mathbf{M}_{dcif}} \begin{bmatrix} \Delta i_{f,d}^* \\ \Delta i_{f,q}^* \end{bmatrix} \\ &+ \underbrace{\begin{bmatrix} \mathbf{P}_3 \\ m_p \mathbf{M}_{PRref} \mathbf{F}_{PQc} \end{bmatrix}}_{\mathbf{M}_{pdcref}} \begin{bmatrix} \Delta P_{out}^* \\ \Delta Q_{out}^* \end{bmatrix} + \underbrace{\begin{bmatrix} \mathbf{P}_4 \\ m_p \mathbf{M}_{ifrefi} \end{bmatrix}}_{\mathbf{M}_{dci}} \Delta \mathbf{i} + \underbrace{\begin{bmatrix} \mathbf{P}_3 \\ m_p \mathbf{M}_{ifrefv} \end{bmatrix}}_{\mathbf{M}_{dcv}} \Delta \mathbf{v}_t\end{aligned}\quad (4.48)$$

where \mathbf{P}_3 and \mathbf{P}_4 are vectors of zero with size corresponding to

$$\mathbf{P}_3 = \mathit{zeros}[1 \times 2], \quad \mathbf{P}_4 = \mathit{zeros}[1 \times 6]$$

Following some matrix manipulation, the reference filter current expression can be obtained as

$$\begin{bmatrix} \Delta i_{f,d}^* \\ \Delta i_{f,q}^* \end{bmatrix} = \mathbf{M}_{dc} \mathbf{M}_{dcref} \begin{bmatrix} \Delta i'_{f,d} \\ \Delta U_{dc}^* \end{bmatrix} + \mathbf{M}_{dc} \mathbf{M}_{pdcref} \begin{bmatrix} \Delta P_{out}^* \\ \Delta Q_{out}^* \end{bmatrix}\quad (4.49)$$

$$+ \mathbf{M}_{dc} \mathbf{M}_{dci} \Delta \mathbf{i} + \mathbf{M}_{dc} \mathbf{M}_{dcv} \Delta \mathbf{v}_t$$

with the matrix \mathbf{M}_{dc} defined as

$$\mathbf{M}_{dc} = [\mathbf{I} - \mathbf{M}_{dcif}]^{-1}$$

With \mathbf{I} representing a 2×2 identity matrix. Equation (4.49) gives the representation of the reference filter current ($\Delta \mathbf{i}_f^*$) in terms of input references (ΔP_{out}^* , ΔQ_{out}^* , $\Delta i'_{f,d}$ and ΔU_{dc}^*), input terminal voltage ($\Delta \mathbf{v}_t$) and currents (Δi_s , Δi_R and Δi_f). This expression is used in the next section where the various subsystems are combined to obtain the overall system.

4.4.6 Combined subsystems

In Subsection (4.4.3), a combined subsystem consisting of the WRIG, the RSC and GSC current controller has been generated leading to a structure defined in (4.25) that can be expressed in small-signal as

$$\Delta \mathbf{i} = \mathbf{G}_{grcc} \Delta \mathbf{i}_{ref}^* + \mathbf{Y}_{grcc} \Delta \mathbf{v}_t \quad (4.50)$$

where

$$\Delta \mathbf{i}_{ref}^* = \begin{bmatrix} \Delta i_{R,d}^* & \Delta i_{R,q}^* & \Delta i_{f,d}^* & \Delta i_{f,q}^* \end{bmatrix}^T$$

To incorporate the outer-controller loops using expressions derived in Sections 4.4.4 and 4.4.5, (4.33) and (4.49) are combined to obtain a representation for \mathbf{i}_{ref}^* as

$$\begin{aligned} \Delta \mathbf{i}_{ref}^* = & \begin{bmatrix} \mathbf{F}_{PQc} & \mathbf{P}_2 \\ \mathbf{M}_{dc} \mathbf{M}_{pdcref} & \mathbf{M}_{dc} \mathbf{M}_{dcref} \end{bmatrix} \begin{bmatrix} \Delta P_{out}^* \\ \Delta Q_{out}^* \\ \Delta i_{f,d}^* \\ \Delta U_{dc}^* \end{bmatrix} \\ & + \begin{bmatrix} -\mathbf{F}_{PQc} \mathbf{H}_{LP,p} \mathbf{M}_{PQ,i} \\ \mathbf{M}_{dc} \mathbf{M}_{dci} \end{bmatrix} \Delta \mathbf{i} + \begin{bmatrix} -\mathbf{F}_{PQc} \mathbf{H}_{LP,p} \mathbf{M}_{PQ,v} \\ \mathbf{M}_{dc} \mathbf{M}_{dcv} \end{bmatrix} \Delta \mathbf{v}_t \end{aligned} \quad (4.51)$$

Inserting (4.51) into (4.50) and following some matrix manipulation

$$\Delta \mathbf{i} = \mathbf{G}_{tot} \begin{bmatrix} \Delta P_{out}^* \\ \Delta Q_{out}^* \\ \Delta i_{f,d}^* \\ \Delta U_{dc}^* \end{bmatrix} + \mathbf{Y}_{tot} \Delta \mathbf{v}_t \quad (4.52)$$

with

$$\begin{aligned} \mathbf{G}_{tot} &= \mathbf{G}_I \left\{ \mathbf{G}_{grcc} \begin{bmatrix} \mathbf{F}_{PQc} \mathbf{H}_{LP,p} & \mathbf{P}_2 \\ \mathbf{M}_{dc} \mathbf{M}_{pdcref} & \mathbf{M}_{dc} \mathbf{M}_{dcref} \end{bmatrix} \right\} \\ \mathbf{Y}_{tot} &= \mathbf{G}_I \left\{ \mathbf{G}_{grcc} \begin{bmatrix} -\mathbf{F}_{PQc} \mathbf{H}_{LP,p} \mathbf{M}_{PQ,v} \\ \mathbf{M}_{dc} \mathbf{M}_{dcv} \end{bmatrix} + \mathbf{Y}_{grcc} \right\} \\ \mathbf{G}_I &= \left\{ \mathbf{I}_{6 \times 6} - \mathbf{G}_{grcc} \begin{bmatrix} -\mathbf{F}_{PQc} \mathbf{H}_{LP,p} \mathbf{M}_{PQ,i} \\ \mathbf{M}_{dc} \mathbf{M}_{dci} \end{bmatrix} \right\}^{-1} \end{aligned}$$

The admittance transfer function matrix (\mathbf{Y}_{tot}) is a 6x2 transfer function matrix constituting the relation from terminal voltage \mathbf{v}_t to i_s , i_R and i_f . The matrix \mathbf{G}_{tot} is a 6x4 transfer function matrix showing the relation from reference input to currents i_s , i_R and i_f . The various transfer functions from matrices \mathbf{G}_{tot} and \mathbf{Y}_{tot} can be used to define new transfer functions matrices for the individual currents as

$$\begin{bmatrix} \Delta i_{s,d} \\ \Delta i_{s,q} \end{bmatrix} = \mathbf{G}_{tot, is} \begin{bmatrix} \Delta P_{out}^* \\ \Delta Q_{out}^* \\ \Delta i_{f,d}^* \\ \Delta U_{dc}^* \end{bmatrix} + \mathbf{Y}_{tot, is} \begin{bmatrix} \Delta v_{t,d} \\ \Delta v_{t,q} \end{bmatrix} \quad (4.53)$$

$$\begin{bmatrix} \Delta i_{R,d} \\ \Delta i_{R,q} \end{bmatrix} = \mathbf{G}_{\text{tot,iR}} \begin{bmatrix} \Delta P_{out}^* \\ \Delta Q_{out}^* \\ \Delta i_{f,d}^* \\ \Delta U_{dc}^* \end{bmatrix} + \mathbf{Y}_{\text{tot,iR}} \begin{bmatrix} \Delta v_{t,d} \\ \Delta v_{t,q} \end{bmatrix} \quad (4.54)$$

$$\begin{bmatrix} \Delta i_{f,d} \\ \Delta i_{f,q} \end{bmatrix} = \mathbf{G}_{\text{tot,if}} \begin{bmatrix} \Delta P_{out}^* \\ \Delta Q_{out}^* \\ \Delta i_{f,d}^* \\ \Delta U_{dc}^* \end{bmatrix} + \mathbf{Y}_{\text{tot,if}} \begin{bmatrix} \Delta v_{t,d} \\ \Delta v_{t,q} \end{bmatrix} \quad (4.55)$$

with

$$\mathbf{G}_{\text{tot}} = \begin{bmatrix} \mathbf{G}_{\text{tot,is}} \\ \mathbf{G}_{\text{tot,iR}} \\ \mathbf{G}_{\text{tot,if}} \end{bmatrix}, \quad \mathbf{Y}_{\text{tot}} = \begin{bmatrix} \mathbf{Y}_{\text{tot,is}} \\ \mathbf{Y}_{\text{tot,iR}} \\ \mathbf{Y}_{\text{tot,if}} \end{bmatrix}$$

Observing (4.53), the transfer function matrix ($\mathbf{Y}_{\text{tot,is}}$) represents the admittance viewed from the DFIG terminal into the generator stator where as the transfer function matrix ($\mathbf{Y}_{\text{tot,if}}$) in (4.55) represents the admittance matrix as viewed from the terminal into the grid-side filter. From the terminal of the DFIG, this two admittances appear to be connected in parallel. Hence, through parallel connection of the two admittances ($\mathbf{Y}_{\text{tot,is}}$ and $\mathbf{Y}_{\text{tot,if}}$), the admittance transfer function matrix for the DFIG as viewed from the terminal into the generator can be obtained as

$$\mathbf{Y}_{\text{DFIG}} = \mathbf{Y}_{\text{tot,is}} - \mathbf{Y}'_{\text{tot,if}} = \begin{bmatrix} \mathbf{Y}_{\text{DFIG,dd}} & \mathbf{Y}_{\text{DFIG,dd}} \\ \mathbf{Y}_{\text{DFIG,qd}} & \mathbf{Y}_{\text{DFIG,qq}} \end{bmatrix} \quad (4.56)$$

where $\mathbf{Y}'_{\text{tot,if}}$ is the transfer function $\mathbf{Y}_{\text{tot,if}}$ transformed to the high voltage-side of the three-winding transformer. The admittance transfer function matrix \mathbf{Y}_{DFIG} , unlike the matrices we have dealt with so far, is non-symmetric. This is to mean that the representation of transfer function matrix using complex transfer function (as done in 4.18) no longer holds. To obtain the phase transfer function in the $\alpha\beta$ frame from the dq transfer function matrix, an approach described in [26] is adopted. According to [26], the phase transfer function in the $\alpha\beta$ frame, through averaging, can be obtained from the dq axes as

$$\begin{aligned} \mathbf{Y}_{\text{DFIG}}(s) = \frac{1}{2} & \left[\mathbf{Y}_{\text{DFIG,dd}}(s - j\omega_s) + \mathbf{Y}_{\text{DFIG,qq}}(s - j\omega_s) \right] + \\ & j\frac{1}{2} \left[\mathbf{Y}_{\text{DFIG,qd}}(s - j\omega_s) - \mathbf{Y}_{\text{DFIG,dq}}(s - j\omega_s) \right] \end{aligned} \quad (4.57)$$

It should be noted that the above expression is valid only for positive sequence admittance. However when dealing with SSR, the interest of frequency range lies in the subsynchronous

frequency range which justifies the use of this approach. The frequency response for the DFIG can be obtained by substituting “s” with “ $j\omega$ ” resulting in an admittance curve shown in Fig. 4.6

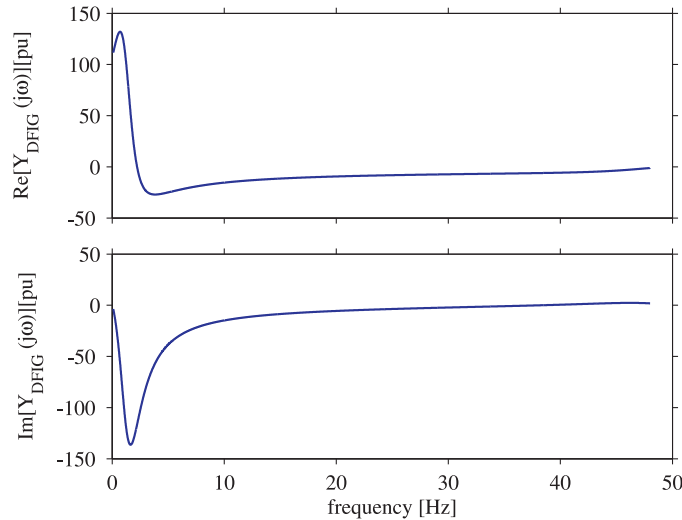


Fig. 4.6 Admittance of a single DFIG wind turbine in the subsynchronous frequency range. $P_{out}=0.72$ pu, $Q_{out}=0$ pu, $\alpha_{cc,R} = \alpha_{cc,f} = 1$ pu, $\alpha_{dc} = 0.1$ pu

4.4.7 Model verification

To validate the derived linearized model of the DFIG, a full switching model of a DFIG in PSCAD/EMTDC having the same parameter and control structure has been utilized. The utilized DFIG model in PSCAD is a generic model developed for voltage-dip analysis and shown to exhibit similar electrical dynamic behavior to an actual wind turbine that is installed at Tvååker, Sweden [42]. However, for the validation purpose at hand, the Advanced Grid Operation (AGO) and the Fault-Ride Through (FRT) capabilities has been disabled

A frequency sweep is performed by injecting a balanced three phase voltage at the terminal having a fundamental frequency component and a harmonic frequency component with a pre-determined amplitude (2% of the fundamental). For every frequency sweep, the superimposed harmonic frequency is varied between 1 Hz and 48 Hz in steps of 1 Hz. When steady-state is reached, the injected voltage and current response are measured. From the measurements the harmonic voltage and current components are extracted to obtain an average phase impedance/admittance.

The validation was performed for various operating point and controller parameters. However, as a demonstration, two output power levels are presented: $P_{out} = 0.72$ pu and $P_{out} = 0.25$ pu. Depending on the selected reference power, the operating speed both for the mathematical model and the PSCAD simulation is determined using a look-up tables and is assumed to be constant during the perturbation. The power level $P_{out} = 0.72$ pu corresponding to supersynchronous speed range where power flows out both from the stator and from the rotor. In this range of operation, the GSC operates as an inverter feeding the power from the rotor into the grid. Fig. 4.7

Chapter 4. System Admittance Modeling

shows a comparison for the real and imaginary part of the admittance obtained using the linearized model and the PSCAD model.

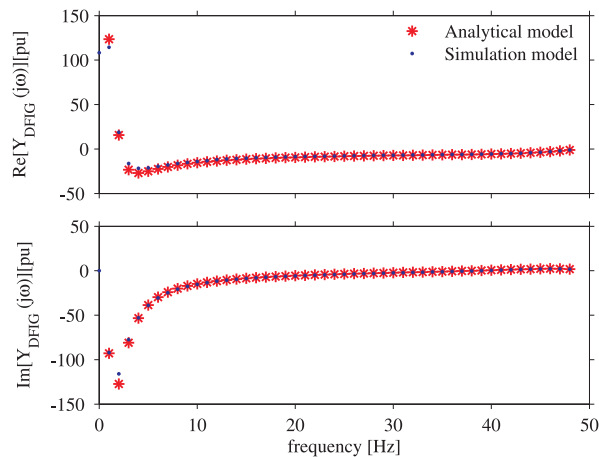


Fig. 4.7 DFIG mathematical model validation. $P_{out}=0.72$ pu, $Q_{out}=0$ pu, $\alpha_{CC}=1$ pu and $\alpha_{dc}=0.1$ pu

The power level $P_{out} = 0.25$ pu corresponding to subsynchronous speed range where power is fed into the rotor from the grid via the BTB converter. Here the GSC operates as a rectifier. The model verification for this power range showing the real and imaginary part of the admittance is depicted in Fig. 4.8

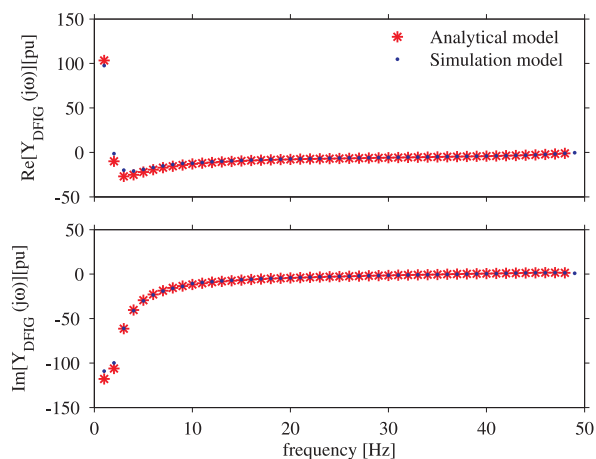


Fig. 4.8 DFIG mathematical model validation. $P_{out}=0.25$ pu, $Q_{out}=0$ pu, $\alpha_{CC}=1$ pu and $\alpha_{dc}=0.1$ pu

The frequency sweep performer in PSCAD showed a good match to the frequency sweep obtained using the linearized model. The DFIG is shown to exhibit a zero-crossing on the imaginary part of its admittance in the frequency range (36 Hz - 38 Hz).

4.5 Conclusion

In this chapter, the development of an admittance model for the investigated system has been presented. A state-space approach has been adopted in building the admittance model for the transmission grid system. The admittance model development for wind turbine adopted a modular approach that break the turbine into small subsystems that can be interfaced with each other. This subsystems were then merged to develop the overall turbine admittance. The obtained admittance plot has been validated against an equivalent wind turbine model in PSCAD/EMTDC.

Chapter 4. System Admittance Modeling

Chapter 5

Frequency domain stability analysis and verification

The system investigated in this thesis has been presented in Chapter 4. In the same chapter, the system has been divided into subsystems, comprising of the wind turbine and the transmission subsystem. A model representation for a single wind turbine has been derived, which in pu will be utilized to represent the aggregate wind farm model. Fig. 5.1(a) shows a single-line diagram of the system expressed in terms of wind farm impedance and grid admittance. The system at hand, can be represented as a SISO using small-signal analysis as shown in Fig. 5.1(b). The wind farm model utilized for this investigation is operated in power control mode. Depending on wind speed, the corresponding maximum power point level is extracted from a look-up table which serves as a reference input to the power controller of the DFIG. In Fig. 5.1(b), the input (Δi^*) is a current reference proportional to the reference active power (P_{out}^*) for the wind farm. A constant wind speed distribution through out the farm is assumed, resulting in a single power reference level. The term $Z_{DFIG}(s)$ is the impedance representation of the DFIG farm which can be represented as a controllable frequency-dependent impedance. The variation in PCC voltage (Δv_t) serves as input to transmission grid admittance $Y_L(s)$. For the variation in Δv_t , the grid response through the line current Δi_t closes the loop.

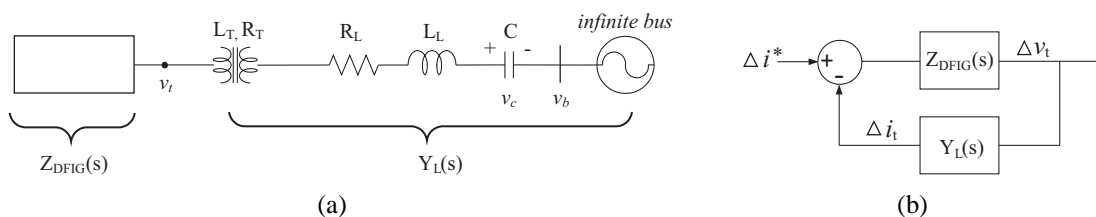


Fig. 5.1 (a) Single line diagram representation for investigated system, (b) SISO representation of the investigated system.

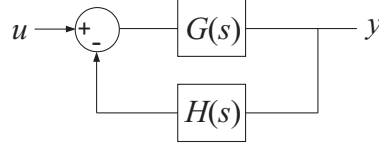


Fig. 5.2 Block diagram representation of a SISO with negative feedback

5.1 Frequency domain stability analysis approach

For the system shown in Fig. 5.2, the stability of the system can be evaluated by analyzing the poles of the closed-loop system $F(s)$ expressed in (5.1) or by applying Nyquist criterion to the open-loop transfer function, $G(s)H(s)$.

$$F(s) = \frac{G(s)H(s)}{1 + G(s)H(s)} \quad (5.1)$$

The frequency domain representation for the individual functions $G(s)$ and $H(s)$ can be expressed as [50]

$$G(j\omega) = G_r(\omega) + jG_i(\omega) \quad (5.2)$$

$$\frac{1}{H(j\omega)} = H'_r(\omega) + jH'_i(\omega)$$

A method using complex torque coefficients is introduced in [51] and [52] for the analysis of the risk of subsynchronous torsional interaction for a steam turbine generator system. In the analysis, the transfer function $G(s)$ represented the mechanical damping torque whereas $H(s)$ is the transfer function for the electrical damping torque. The damping coefficients ($G_r(\omega)$ and $H'_r(\omega)$) and the spring constants ($G_i(\omega)$ and $H'_i(\omega)$) are then employed to derive a net damping criterion, which states that for each closed-loop resonance ω , if (5.3) holds, there exists no risk of torsional interaction

$$D(\omega) = G_r(\omega) + H'_r(\omega) > 0 \quad (5.3)$$

However, it was in [50] that, both proof and modification for the above analysis was provided. Using the Nyquist criterion, it has been shown that the above criterion should be applied for the open-loop resonance and not for the closed loop resonance as well as for low frequencies where the loop gain does not exceed unity. The above analysis can be extended to assess the stability of an impedance/ admittance based interconnected system expressed as a SISO. Here, instead of using damping coefficients, the frequency-dependent impedance and admittance characteristics of the individual subsystems can be used to generate a similar relation. Replacing the Laplace variable “s” with $j\omega$, the open-loop relation can be expressed as

$$\begin{aligned}
 G(j\omega)H(j\omega) &= \frac{G_r(\omega) + jG_i(\omega)}{H'_r(\omega) + jH'_i(\omega)} \\
 &= \underbrace{\frac{G_r(\omega)H'_r(\omega) + G_i(\omega)H'_i(\omega)}{H'_r(\omega)^2 + H'_i(\omega)^2}}_{\text{Re}[G(j\omega)H(j\omega)]} + j \underbrace{\frac{G_i(\omega)H'_r(\omega) - G_r(\omega)H'_i(\omega)}{H'_r(\omega)^2 + H'_i(\omega)^2}}_{\text{Im}[G(j\omega)H(j\omega)]} \quad (5.4)
 \end{aligned}$$

Based on the Nyquist criterion, if the individual subsystems are stable (meaning have no poles in the right-hand plane), the closed-loop system, $F(s)$ will also be stable; provided that the open-loop transfer function $G(s)H(s)$ does not encircle the -1. By applying the classical Nyquist criterion to the expression of (5.4), non encloser of -1 is guaranteed if:

$$\text{Re}[G(j\omega_N)H(j\omega_N)] > -1 \xrightarrow{\text{for } \omega_N} \text{Im}[G(j\omega_N)H(j\omega_N)] = 0 \quad (5.5)$$

Therefore, the stability of the closed-loop system $F(s)$ is guaranteed if $\text{Re}[G(j\omega_N)H(j\omega_N)] > -1$ holds for ω_N that satisfies $\text{Im}[G(j\omega_N)H(j\omega_N)] = 0$. Replacing $G(j\omega)$ with frequency-dependent DFIG impedance, $Z_{DFIG}(j\omega)$, and $H(j\omega)$ to represent the admittance of the transmission grid, $Y_L(j\omega)$, the relation provided in (5.5) can be used to evaluate the stability of the closed-loop system shown in Fig.5.1(b). In this thesis, the criteria in (5.5) is referred to as impedance-based Nyquist criterion. Here it should be noted that ω_N represents the open-loop resonance, not the closed-loop resonance of the system.

Before proceeding to utilize the impedance based Nyquist stability analysis to assess the stability of the interconnected system shown in Fig. 5.1(a), frequency-domain analysis for the individual subsystem can be evaluated. This helps to gain insights into the various controller parameters and system conditions that could impact the impedance/admittance behavior of the subsystem. The obtained result serves as a guidance for identifying system conditions and parameter variations that potentially affect the system's overall stability.

5.2 Frequency domain analysis for DFIG system

In Chapter 4, the admittance modeling for the overall DFIG turbine has been presented. The method has been proven to be an efficient approach for obtaining the frequency domain admittance, (in the subsynchronous frequency range) which can further be used to obtain the frequency domain impedance.

The DFIG mainly comprises of an induction generator with converters. Its behavior is therefore influenced by the behaviors of the induction generator and converters collectively. To just evaluate individually the various subsystem to arrive at a viable conclusion is not feasible. However the same approach can be used to identify system parameters and conditions that affect the various subsystem. To start off, the influence due to the induction generator is evaluated from an impedance point of view.

5.2.1 Influence of induction generator

As a baseline for evaluating the influence of the induction generator, the impedance plot of the induction generator used for the modeling is considered. Observe that the presented plots are related to the induction generator only and that the converters here are not considered. The induction generator is a WRIG however, in this section, the rotors are short-circuited hence acting as a squirrel cage induction generator. This is a justified simplification as the aim is to alienate the effect of the induction generator from that of the converter. The mechanical drive train of the induction generator is not taken into account throughout this analysis. Fig. 5.3 shows the impedance plot for the induction generator that has a rotor electrical speed corresponding to $\omega_r = 1.1\omega_s$ where ω_s is the fundamental angular frequency.

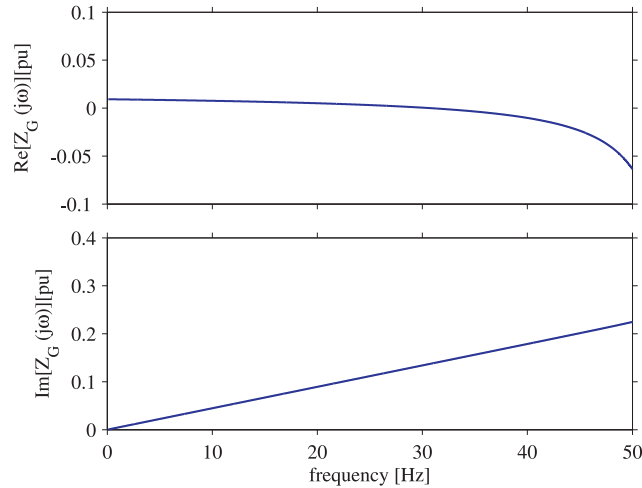


Fig. 5.3 Frequency domain impedance of induction generator. $\omega_r = 1.1$ pu

The induction generator has a negative resistance for a range of frequencies below the synchronous frequency. This indicates that the induction generator has a negative influence on the system's ability to dissipate power. To further elaborate this, the steady-state circuit representation of an induction generator shown in Fig. 5.4 is considered. The term v_R is the rotor voltage (in the Γ representation) which in this analysis is set to zero (short circuited). The term s' indicates the slip term due to the slip associated with the rotor speed of rotation. This term can be expressed in Laplace domain as

$$s' = \frac{s - j\omega_r}{s} \quad (5.6)$$

where ω_r is the rotor electrical angular frequency. From the equivalent circuit (see Fig. 5.4), the impedance for the induction generator can be written (in the s -domain) as

$$Z_G(s) = R_s + \left(\frac{R_R}{s'} + sL_R \right) // sL_M \quad (5.7)$$

5.2. Frequency domain analysis for DFIG system

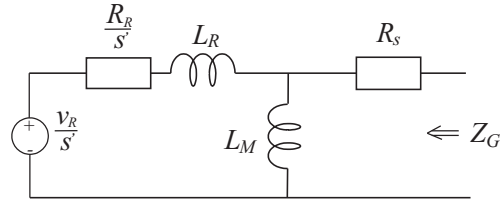


Fig. 5.4 Steady-state equivalent circuit diagram of an induction generator

As the magnetization inductance of the machine is much larger ($L_M \gg L_R$), the above expression can be further simplified as

$$Z_G(s) = R_s + sL_R + \frac{R_R}{s'} \quad (5.8)$$

Evaluating the relation in (5.8), there exists a term R_s that under the given assumptions, is frequency independent. The second term sL_R results in a positive-complex impedance that contributes to the imaginary part of the induction generator impedance. The third term, constituting of the ratio of the rotor resistance R_R and s' is the one attributing to the observed negative resistance. The R_R is individually frequency independent, however, the contribution of s' for frequency range below the rotor angular frequency is negative as a result of $\omega < \omega_r$. This causes the ratio to be negative in the frequency range below the angular-rotor frequency.

For a fixed rotor speed, the negative resistance increases as the frequency approaches the rotational frequency. This can also be observed in Fig. 5.3, where the resistive impedance is positive up to a 30 Hz indicating that $\frac{R_R}{s'}$ value does not exceed R_s . However, after this frequency, the resistive impedance becomes negative.

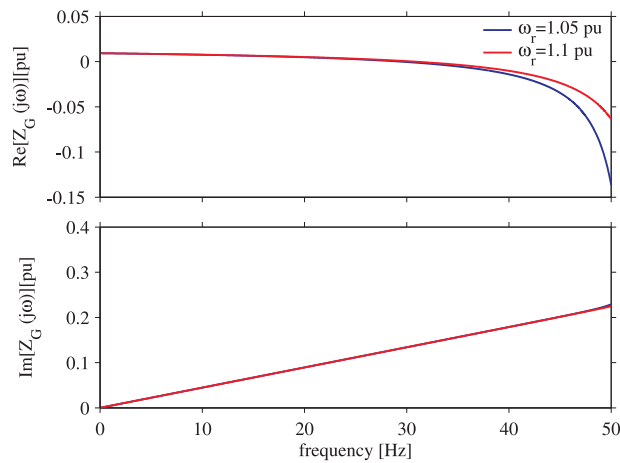


Fig. 5.5 Frequency domain impedance of an induction generator for varied rotor speed. $\omega_r=1.05$ pu (blue curve) and $\omega_r=1.1$ pu (red curve)

To observe the influence of the rotor speed, the impedance of the generator for two different rotor speeds is plotted in Fig. 5.5. It can be observed that the curve with a higher rotor speed

exhibits a lower negative resistance. This is associated with the fact that as the rotor speed increases, the term $|s'|$ get larger resulting in lower values of $\frac{R_R}{s'}$.

Another aspect to be evaluated is the impact of the generator parameters. Here, the influence of rotor resistance R_R in combination with the slip term serves as a good starting point. Fig. 5.6 shows the impedance plot for a constant rotor speed of 1.1 pu with a 10% increase and decrease of the rotor resistance. As can be speculated from (5.8), increase in rotor resistance will contribute to an overall higher negative resistance and the opposite applies for a lower rotor resistance (see Fig. 5.6). However, it should be noted that the influence of the rotor resistance on the impedance even for a high deviation of 10 % is not still substantial.

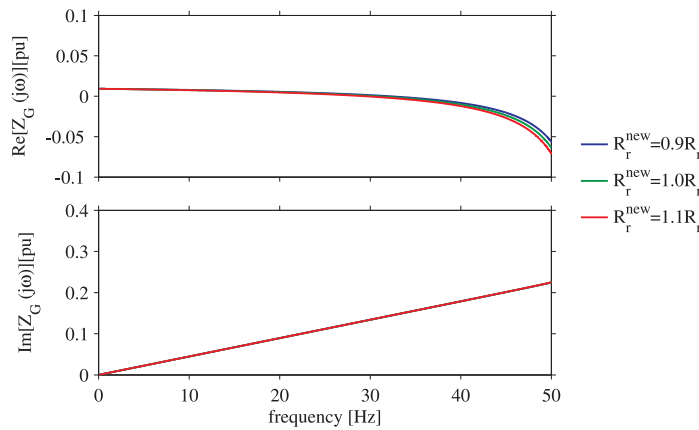


Fig. 5.6 Frequency domain impedance of induction generator for varied rotor resistance. $\omega_r=1.1$ pu

5.2.2 Influence of rotor-side converter

In the previous subsection, the behavior of an induction generator in the subsynchronous frequency range has been discussed. To further create an understanding, the impact of the RSC on the DFIG impedance characteristics is evaluated in this subsection. The impact of the rotor-side converter to the risk of SSCI has been reported in a number of literature [14] [9] [12, 53–55] The RSC modeled in terms of its control structure has a cascaded controller with an inner current controller and an outer power controller. The WRIG with a current controller as derived in Subsection 4.4.1 has been considered. Here, the preliminary assumption are:

- The rotor reference current that serves as an input to the RSC current controller are known with good accuracy.
- The RSC is considered to be a linear amplifier, meaning, any higher order harmonics due to switching are neglected. In addition, the converter is considered lossless.

The impedance plot for the WRIG, having current controller connected to the rotor side is obtained from the admittance relation derived in (4.18) is shown in Fig. 5.7. The system shows a negative resistive part throughout the subsynchronous frequency range with a bending inductive

5.2. Frequency domain analysis for DFIG system

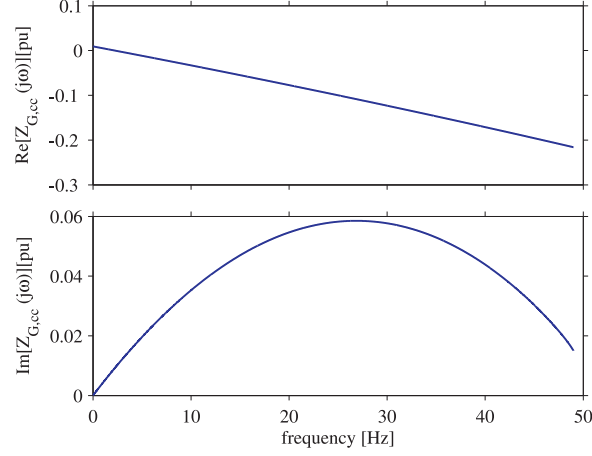


Fig. 5.7 Frequency domain impedance of an induction generator with a current controller based voltage source attached to the rotor. Closed-loop bandwidth for the current controller, $\alpha_{cc}=1.0$ pu. $\omega_r=1.1$ pu

reactance. Comparing the result with the plots obtained from considering the induction generator alone (see Fig. 5.3), it can be observed that a higher negative resistance occurs with the inclusion of the RSC current controller.

Consider the rotor voltage equation generated by the current controller presented in (4.12)

$$\underline{v}_R^{*(dq)}(s) = F_{cc,R}(s) \left(\underline{i}_R^{*(dq)}(s) - \underline{i}_R^{(dq)}(s) \right) + j\omega_2 L_R \underline{i}_R^{(dq)}(s) + H_{LP}(s) \hat{\underline{e}}_{emf}^{(dq)}(s) \quad (5.9)$$

For ease of analysis, the feed-forward term involving the back-EMF is neglected. Assuming $\underline{v}_R^{(dq)} = \underline{v}_R^{*(dq)}$, the expression (5.9) results in

$$\underline{v}_R^{(dq)}(s) = F_{cc,R}(s) \underline{i}_R^{*(dq)}(s) - [F_{cc,R}(s) - jM_{dq}] \underline{i}_R^{(dq)}(s) \quad (5.10)$$

where jM_{dq} is the controller decoupling term. Moving the analysis to the stationary reference frame, the above expression can be rewritten as

$$\underline{v}_R(s) = F_{cc,R}(s - j\omega_s) \underline{i}_R^*(s) - [F_{cc,R}(s - j\omega_s) - jM_{dq}] \underline{i}_R(s) \quad (5.11)$$

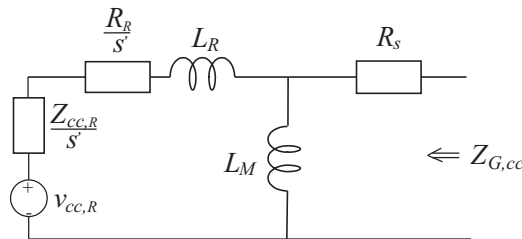


Fig. 5.8 Equivalent circuit diagram of an induction generator with current controller based voltage source connected to the rotor

From (5.11), the current controller can be expressed (taking the positive sequence) by a voltage source $v_{cc,R} = F_{cc,R}(s - j\omega_s) \underline{i}_R^*$ behind an impedance $Z_{cc,R}(s) = [F_{cc,R}(s - j\omega_s) - jM_{dq}]$.

Fig. 5.8 shows the steady-state equivalent circuit representation of an induction generator with a rotor-side current controller. From an equivalent circuit point of view, the inclusion of the rotor-side current controller results in a frequency dependent complex impedance in series with a voltage source. Therefore, comparing Fig. 5.3 and Fig. 5.7, the consequences of having a current controller can be associated with a pronounced frequency dependent negative resistance and a much lower inductive reactance. In addition, according to (5.11), the complex impedance ($Z_{cc,R}$) is influenced by parameters of the controller.

Variation in rotor-side current controller bandwidth

Recalling that the RSC current controller is a proportional controller with gain, $k_{p,cc} = \alpha_{cc,R}L_R$, its impact can be evaluated by considering the closed-loop current controller bandwidth $\alpha_{cc,R}$. As the aim is to evaluate the weight of this parameter on the impedance behavior of the DFIG subsystem, the overall impedance model of the DFIG is considered for the analysis. Frequency scan, in the subsynchronous frequency range, using the linearized mathematical model derived in Chapter 4. Fig. 5.9 shows the DFIG input impedance for different values of $\alpha_{cc,R}$. Here, a constant output power corresponding to $P_{out} = 0.72$ pu and $Q_{out} = 0$ pu is assumed. The closed-loop current controller bandwidth for the GSC is set to $\alpha_{cc,f} = 1$ pu. The outer power controller gain was held at $k_{p,p} = 5$ pu with an integrator time constant corresponding to $T_{i,p} = 0.2$ sec. The bandwidth for the dc-link voltage controller was maintained at $\alpha_{dc} = 0.1$ pu.

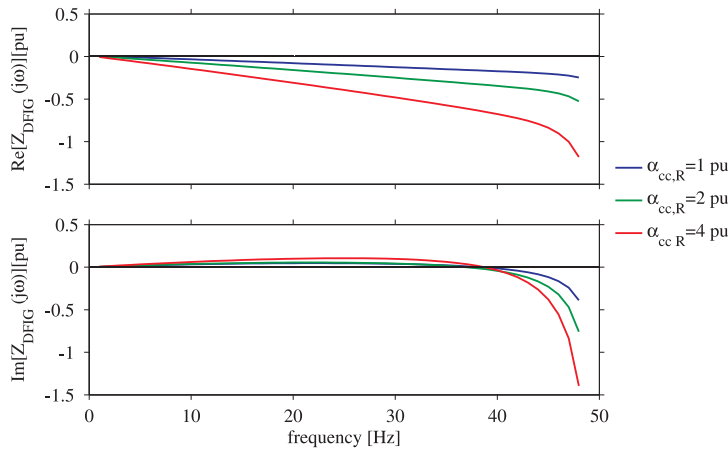


Fig. 5.9 DFIG impedance for varied RSC current controller bandwidth. α_{CC} varied from 1 pu to 4 pu

From Fig. 5.9, the DFIG impedance by itself is shown to exhibit a zero-crossing for the imaginary part (here denoted as “resonance”) that varies with the current controller bandwidth. As can be observed from the lower plot, the impact of the variation in $\alpha_{cc,R}$ is a small shift on the zero crossing associated with the DFIG reactance. The variation also affects the resistive impedance presented by the DFIG. Referring to the upper plot of Fig. 5.9, increase in the current controller bandwidth results in a substantial increased of negative resistance over a wide subsynchronous frequency range. This is due to the fast action of the RSC current controller that effectively produces a higher rotor resistance. However, due to the negative slip associated with

5.2. Frequency domain analysis for DFIG system

the machine, this resistance appears as a negative resistance as seen from the stator terminals. The above result is in sync with the analysis drawn earlier with regards to the impact of the RSC current controller.

Variation in power controller parameters

To account for the influence of the outer-loop power controller, a similar procedure of impedance evaluation is adopted by varying the controller gain ($k_{p,P}$)¹ and integrator time-constant ($T_{i,P}$). To start, a frequency scan has been utilized to evaluate the impact of varied power controller gain ($k_{p,P}$) on the impedance character of the DFIG. A constant output power corresponding to $P_{out} = 0.72$ pu and $Q_{out} = 0$ pu is considered. Both the RSC and GSC closed-loop current controller bandwidths are set to 1 pu. The outer power controller gain $k_{p,P}$ is varied for four different values whereas the integrator time-constant is held constant at $T_{i,P} = 0.2$ sec. The closed-loop bandwidth for the outer dc-link voltage controller has been set at $\alpha_{dc} = 0.1$ pu. The obtained result is shown in Fig. 5.10

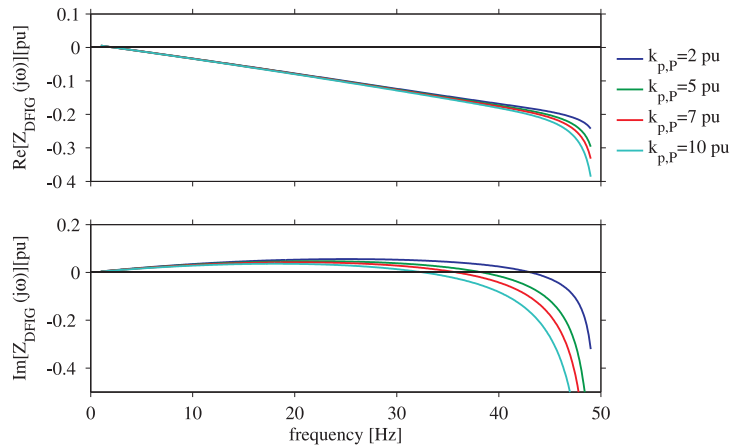


Fig. 5.10 DFIG turbine impedance for varied RSC outer controller loop parameters. $k_{p,P}$ varied from 2 pu to 10 pu

As it can be observed from Fig. 5.10 (upper plot), $k_{p,P}$ is shown to affect the resistive part of the DFIG impedance mainly in the frequency range, 37 - 50 Hz. The higher negative resistance is associated with a higher $k_{p,P}$ gain value. On the other hand, in the lower plot of Fig. 5.10, the power controller gain clearly affects the resonance of the DFIG impedance resulting in a lower resonance frequency for an increase in $k_{p,P}$ gain. Proceeding to evaluation of the influence of the integral term in the outer-loop power controller, frequency scan under similar conditions with the exception that $k_{p,P}$ is set to 5 pu and the integrator time constant $T_{i,P}$, is varied for three different values, is shown in Fig. 5.11.

¹Both the active and reactive outer power controller gain are varied. i.e. $k_{p,P} = k_{p,Q}$. For the sake of clarity, $k_{p,P}$ is mentioned through out the text

Chapter 5. Frequency domain stability analysis and verification

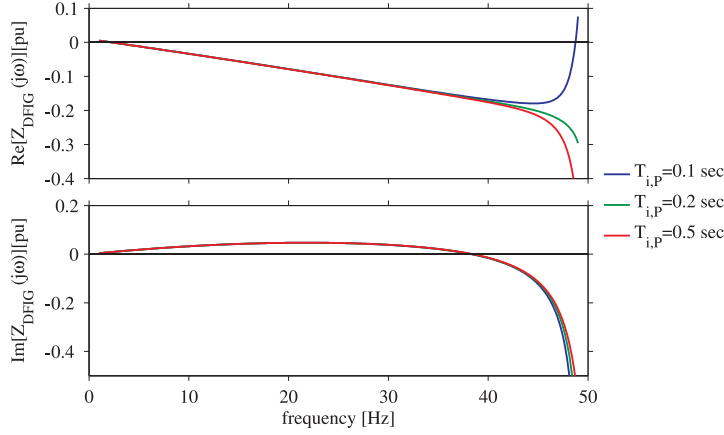


Fig. 5.11 DFIG turbine impedance for varied RSC outer controller loop parameters. Integrator time constant, $T_{i,p}$ varied from 0.1 sec to 0.5 sec. $k_{p,p}=5$ pu.

Evaluating Fig. 5.11, the resistive component of the DFIG (upper plot) for a $T_{i,p}$ of 0.1 sec, presents a negative resistance at lower frequencies and a negative minimum resistance is produced around 45 Hz. This builds to a positive resistance for a short frequency range close to the fundamental. However, for values of $T_{i,p}$ higher than 0.2 sec, the resistance preserves a negative value for the whole subsynchronous frequency range; with higher negative values associated to higher $T_{i,p}$ value. It can be noted that, for all values of $T_{i,p}$, the variation on the resistive part is negligible for the frequencies ranges below 35 Hz. When it comes to the resonance of the DFIG (lower plot of Fig. 5.11), the impact of $T_{i,p}$ is shown to be almost insignificant.

To obtain analytical representation, consider the generator expression presented in Section (4.11) of the previous chapter, expressed here as

$$\mathbf{M}_g \mathbf{i}_g = \mathbf{M}_R \mathbf{v}_R + \mathbf{M}_s \mathbf{v}_s \quad (5.12)$$

Again for analysis purposes, considering a simplified expression for the current controller given in (5.10) and expressing it in matrix form as

$$\mathbf{v}_R = \underbrace{\begin{bmatrix} F_{cc,R} & 0 \\ 0 & F_{cc,R} \end{bmatrix}}_{\mathbf{F}_{cc,R}} \mathbf{i}_R^* + \underbrace{\begin{bmatrix} 0 & 0 & -F_{cc,R} & -M_{dq} \\ 0 & 0 & M_{dq} & -F_{cc,R} \end{bmatrix}}_{\mathbf{M}'_{cc,R}} \mathbf{i}_g \quad (5.13)$$

where

$$\mathbf{v}_R = \begin{bmatrix} v_{R,d} & v_{R,q} \end{bmatrix}, \quad \mathbf{i}_R^* = \begin{bmatrix} i_{R,d}^* & i_{R,q}^* \end{bmatrix},$$

and \mathbf{i}_g is as described in (4.11). The analysis is moved into small-signal as the incorporation of the outer-loop controller causes the system to be non-linear. The GSC is neglected and P_{out} is considered equivalent to P_s^2 . This is a valid assumption as the aim here is to evaluate the impact

²Similarly under the assumption that the GSC is removed, the following also holds $Q_{out} = Q_s$, $i_t = i_s$ and $v_t = v_s$

5.2. Frequency domain analysis for DFIG system

of the RSC outer-loop controller. Taking the expression of the power controller given in (4.27) followed by simple modification, the expression for \mathbf{i}_R^* is obtained as

$$\begin{bmatrix} \Delta i_{R,d}^* \\ \Delta i_{R,q}^* \end{bmatrix} = \mathbf{F}_{Pc} \begin{bmatrix} \Delta P_s^* \\ \Delta Q_s^* \end{bmatrix} - \mathbf{F}_{Pc} \mathbf{H}_{LP,p} \begin{bmatrix} \Delta P_s \\ \Delta Q_s \end{bmatrix} \quad (5.14)$$

let us express the stator active and reactive power as

$$\begin{bmatrix} \Delta P_s \\ \Delta Q_s \end{bmatrix} = \begin{bmatrix} -3v_{s,d0} & -3v_{s,q0} \\ -3v_{s,q0} & 3v_{s,d0} \end{bmatrix} \begin{bmatrix} \Delta i_{s,d} \\ \Delta i_{s,q} \end{bmatrix} + \begin{bmatrix} -3i_{s,d0} & -3i_{s,q0} \\ 3i_{s,q0} & -3i_{s,d0} \end{bmatrix} \begin{bmatrix} \Delta v_{s,d} \\ \Delta v_{s,q} \end{bmatrix} \quad (5.15)$$

Inserting (5.15) in (5.14) and combining the resulting expression with the small-signal expression of (5.13), results in

$$\mathbf{K}_i \Delta \mathbf{i}_g = \mathbf{K}_{ref} \begin{bmatrix} \Delta P_s^* \\ \Delta Q_s^* \end{bmatrix} + \mathbf{K}_{Y,rsc} \Delta \mathbf{v}_s \quad (5.16)$$

where the matrices are described as

$$\begin{aligned} \mathbf{K}_i &= \mathbf{M}_g - \mathbf{M}_R \left\{ \mathbf{M}'_{cc,R} - \mathbf{F}_{cc,R} \mathbf{F}_{Pc} \mathbf{H}_{LP,p} \mathbf{M}_{PQ, is} \right\} \\ \mathbf{K}_{ref} &= \mathbf{M}_R \mathbf{F}_{cc,R} \mathbf{F}_{Pc} \\ \mathbf{K}_{Y,rsc} &= \mathbf{F}_{cc,R} \mathbf{F}_{Pc} \mathbf{H}_{LP,p} \mathbf{M}_{PQ, v} + \mathbf{M}_s \end{aligned}$$

The characteristics polynomial for the admittance matrix can be obtained from the $\mathbf{K}_i^{-1} \mathbf{K}_{Y,rsc}$ which results in a fourth-order polynomial that can be represented as

$$c_4 s^4 + c_3 s^3 + c_2 s^2 + c_1 s + c = 0 \quad (5.17)$$

with

$$\begin{aligned} c &= F_{cc,R}^2 R_s^2 + M_{dq}^2 R_s^2 + 2F_{cc,R} R_R R_s^2 + R_R^2 R_s^2 + F_{cc,R}^2 L_M^2 \omega_s^2 + L_M^2 M_{dq}^2 \omega_s^2 + 2F_{cc,R} L_M^2 R_R \omega_s^2 + \\ & L_M^2 R_R^2 \omega_s^2 - 9F_{cc,R}^2 F_{pc}^2 H_{LP,p}^2 L_M^2 v_{s,d0}^2 \omega_s^2 - 9F_{cc,R}^2 F_{pc}^2 H_{LP,p}^2 L_M^2 v_{s,q0}^2 \omega_s^2 - 2L_M M_{dq} R_s^2 \omega_2 - \\ & 2L_R M_{dq} R_s^2 \omega_2 + 2F_{cc,R} L_M^2 R_s \omega_s \omega_2 + 2L_M^2 R_R R_s \omega_s \omega_2 - 2L_M^2 L_R M_{dq} \omega_s^2 \omega_2 + L_M^2 R_s^2 \omega_2^2 + \\ & 2L_M L_R R_s^2 \omega_2^2 + L_R^2 R_s^2 \omega_2^2 + L_M^2 L_R^2 \omega_s^2 \omega_2^2 \\ c_1 &= 2F_{cc,R}^2 L_M R_s + 2L_M M_{dq}^2 R_s + 4F_{cc,R} L_M R_R R_s + 2L_M R_R^2 R_s + 2F_{cc,R} L_M R_s^2 + 2F_{cc,R} L_s G R_s^2 + \\ & 2L_M R_R R_s^2 + 2L_R R_R R_s^2 + 2L_M^2 M_{dq} R_s \omega_s + 2F_{cc,R} L_M^2 L_R \omega_s^2 + 2L_M^2 L_R R_R \omega_s^2 - 2L_M^2 M_{dq} R_s \omega_2 - \\ & 4L_M L_R M_{dq} R_s \omega_2 + 2L_M^2 L_R R_s \omega_2^2 + 2L_M L_R^2 R_s \omega_2^2 \\ c_2 &= F_{cc,R} L_M^2 + L_M^2 M_{dq}^2 + 2F_{cc,R} L_M^2 R_R + L_M^2 R_R^2 + 2F_{cc,R} L_M^2 R_s + 4F_{cc,R} L_M L_R R_s + 2L_M^2 R_R R_s + \\ & 4L_M L_R R_R R_s + L_M^2 R_s^2 + 2L_M L_R R_s^2 + L_R^2 R_s^2 - 9F_{cc,R}^2 F_{pc}^2 H_{LP,p}^2 L_M^2 v_{s,d0}^2 - 9F_{cc,R}^2 F_{pc}^2 H_{LP,p}^2 L_M^2 v_{s,q0}^2 \\ & + L_M^2 L_s^2 \omega_s^2 - 2L_M^2 L_R M_{dq} \omega_2 + L_M^2 L_R^2 \omega_2^2 \\ c_3 &= 2F_{cc,R} L_M^2 L_R + 2L_M^2 L_R R_R + 2L_M^2 L_R R_s + 2L_M L_R^2 R_s \\ c_4 &= L_M^2 L_R^2 \end{aligned}$$

The analytical expression obtained in (5.17), is a quadratic equation. According to [33], a general formula exist for obtaining poles of a cubic expression³. However the practical expression obtained remains too complex to extract analytical relation between the individual parameters and the respective system poles, that indirectly influence the system behaviour.

5.2.3 Influence of grid-side converter

In the previous subsection, the influence of the RSC with regard to controller parameter variation on the impedance characteristics of the total DFIG has been addressed. It has also been shown that the inner current controller parameter influences the negative resistance behavior strongly whereas the outer controller parameters affects the resonance point and noticeably in the frequency ranges closer to the fundamental frequency. In this subsection, the influence of the GSC on the impedance characteristics of the DFIG is covered. In a similar fashion, the evaluation starts with assessing the impact of the grid-side current controller and moves to include the impact of the dc-link voltage controller parameters.

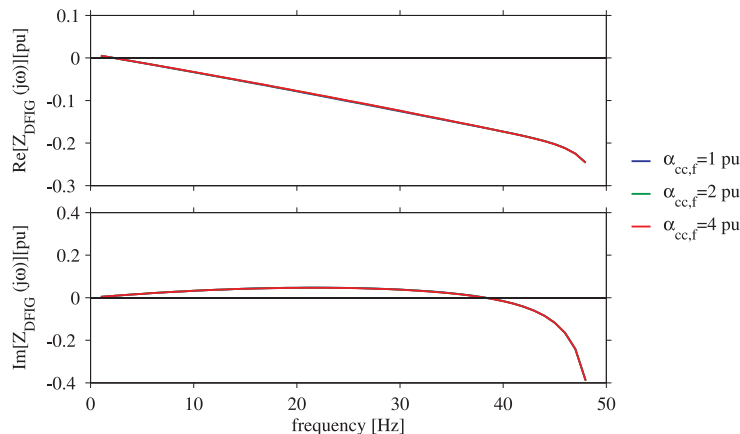


Fig. 5.12 DFIG impedance for varied grid-side current controller bandwidth. $\alpha_{cc,f}$ varied between 1 pu to 4 pu.

Variation in grid-side current controller bandwidth

The GSC, as described in Chapter 3, is a PI based current controller with a proportional gain $k_{pf,cc} = \alpha_{cc,f}L_f$ and an integral gain $k_{if,cc} = \alpha_{cc,f}R_f$, where $\alpha_{cc,f}$ is the closed-loop current controller bandwidth, and R_f and L_f are the resistive and inductive losses of the grid-side filter, respectively. Similar to the RSC, the GSC closed-loop current controller bandwidth is selected as a variable. Fig. 5.12 shows the frequency sweep of the total DFIG input impedance considering three different values of $\alpha_{cc,f}$. A constant output power of $P_{out} = 0.72$ pu and $Q_{out} = 0$ pu are assumed. The closed-loop current controller bandwidth for the RSC is held constant at $\alpha_{cc,R} = 1$ pu whereas the closed-loop bandwidth of the GSC is varied between 1 pu and 4 pu.

³The full expression for obtaining the roots of a quadratic equation is too large to be presented here. However the interested reader can refer to [33] [56] for further details

5.2. Frequency domain analysis for DFIG system

The RSC outer power controller gain is held at $k_{p,P} = 5$ pu with the integrator time-constant corresponding to $T_{i,P} = 0.2$ sec. The closed-loop bandwidth of the dc-link voltage controller is set to $\alpha_{dc} = 0.1$ pu.

The frequency sweep of Fig. 5.12 shows minimal influence, both on the resistive and reactive impedance of DFIG characteristics, in the subsynchronous frequency range. This implies that the parameter of the GSC current controller does not influence the impedance behavior of the DFIG.

Variation in dc-link voltage controller parameters

The final step in evaluating the effects of the controller parameters on the DFIG impedance is to see the impacts of the dc-link voltage controller parameters as described in Chapter 3, Section 3.3.2

To investigate the impacts of the dc-link voltage controller, a frequency sweep of the DFIG input impedance with varied α_{dc} is depicted in Fig. 5.13. Similar to previous considerations, $P_{out} = 0.72$ pu and $Q_{out} = 0$ pu is considered. Both the RSC and GSC current controller bandwidth are held constant at $\alpha_{cc,R} = \alpha_{cc,f} = 1$ pu. RSC power controller parameters are $k_{p,P} = 5$ pu and $T_{i,P} = 0.2$ sec.

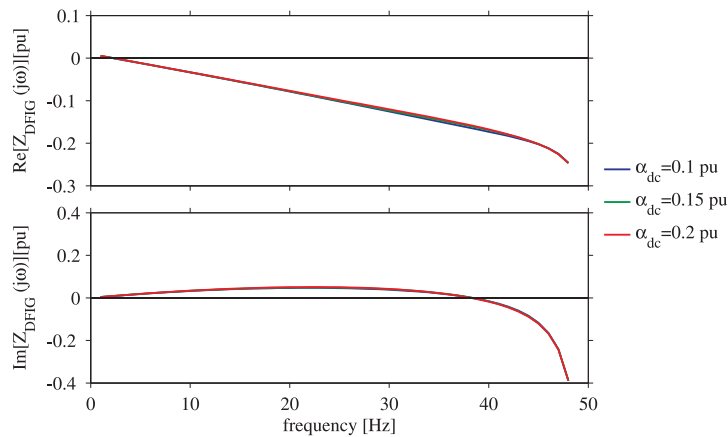


Fig. 5.13 DFIG impedance for varied dc-link controller bandwidth. $\alpha_{dc} = 0.1$ pu (blue), $\alpha_{dc} = 0.15$ pu (green), and $\alpha_{dc} = 0.2$ pu (red)

According to Fig. 5.13, a very small variation is observed in the resistive term of the DFIG impedance (in the frequency range, 20-40 Hz) as a higher α_{dc} value results in a less negative resistance value. However it should be noted that as compared to the RSC current controller bandwidth, the impact of the dc-link voltage controller is insignificant. Besides what is presented here, it has been reported in [29] that the impact of dc-link voltage controller on the admittance of the converter is dependent on whether the converter is operated as a rectifier or as an inverter. The author shows that in the rectifier mode of operation (that can correspond to the case when the DFIG is operated in the subsynchronous speed range) the converter presents a negative admittance for the subsynchronous frequency range. Based on this fact, the impact

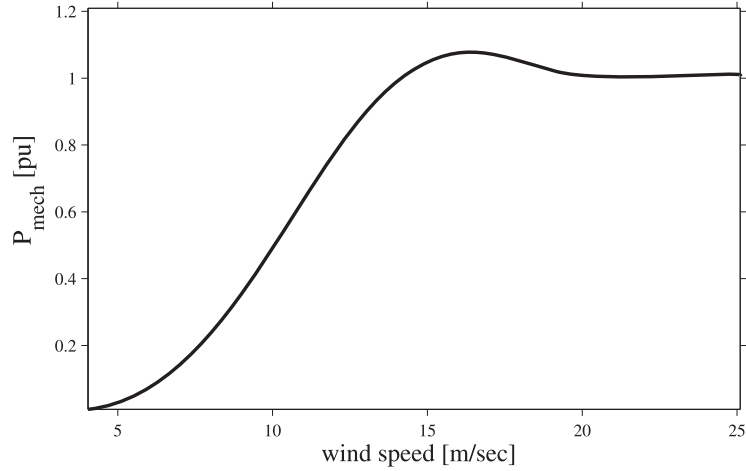


Fig. 5.14 Mechanical power verse wind speed at rated rotor speed

of the dc-link controller when the DFIG is operated in the subsynchronous frequency range will be evaluated in the next subsection dealing with the influence of operating condition.

5.2.4 Influence of operating condition

Energy harnessed from wind generation units varies through time due to the variable nature of the available wind speed. Therefore the power generated from wind also varies in a somewhat proportional manner with the available wind speed. The advantages of employing variable speed wind turbine are mainly for the purposes of harnessing this energy over a wider range of wind-speed. In case of DFIG based wind turbine, this is accomplished by regulating the speed to the turbine by injecting variable frequency voltage in the rotor circuits through the means of the BTB converter. At a lower wind-speed range, when the turbine rotational speed (electrical speed) is below ω_s (here referred to as subsynchronous speed range), the GSC operates as a rectifier supplying power from the grid into the rotor. On the other hand, at a higher wind speed, when the turbine electrical rotational speed is above ω_s (supersynchronous speed range), the GSC operates as an inverter pushing power into the grid. In the results presented in previous sections, the analysis were performed under the assumption that the turbine is operated in the supersynchronous speed range. In this section, results dealing with subsynchronous speed range are presented. According to [41], the impact of the wind speed can be directly related to the input mechanical power as

$$P_{mech} = \frac{1}{2} \rho A_r C_p (\lambda, \beta) w^3 \quad (5.18)$$

$$\lambda = \frac{\omega_r r_r}{w}$$

where C_p is the coefficient of performance, β is the pitch angle, λ is the tip-speed ratio and w is the wind speed. ω_r represents the rotor speed on the low speed side and r_r is the plane rotor radius. ρ is the density of the air and A_r represents the area swept by the rotor. Detailed

5.2. Frequency domain analysis for DFIG system

description of (5.18), is beyond the scope of this work. However, as shown in [41] a sketch is used to illustrate the relationship between the input mechanical power and the wind speed (shown in Fig. 5.14). As can be observed, the input to the wind turbine has a fairly linear relation up to a certain wind speed limit, beyond this limit the pitch of blades are controlled to limit the input power at rated value. As a result, a constant power is harnessed even for higher wind speed.

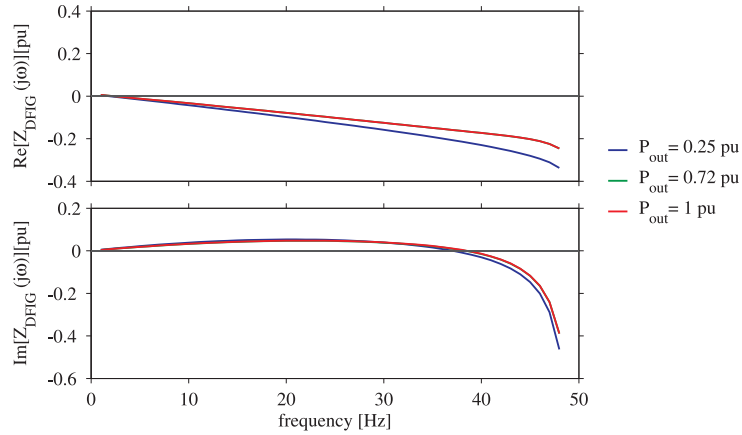


Fig. 5.15 DFIG impedance for various output power. $P_{out} = 0.25$ pu (blue), $P_{out} = 0.72$ pu (green), and $P_{out} = 1.0$ pu (red)

Returning to the analysis at hand, the impact of the variation of wind speed (here represented through the variation of output power, P_{out}), on the input impedance of the DFIG is shown in Fig. 5.15. The reactive power Q_{out} is controlled to 0 pu. Both the RSC and GSC current controller bandwidth are set to $\alpha_{cc,R} = \alpha_{cc,R} = 1$ pu. The outer power controller parameters $k_{p,P} = 5$ pu and $T_{i,P} = 0.2$ sec are considered. The dc-link voltage controller closed-loop bandwidth is set to $\alpha_{dc} = 0.1$ pu. Both the upper and lower plot of Fig. 5.15, for $P_{out} = 1$ pu and $P_{out} = 0.72$ pu show minimal variation on the resistive and inductive impedance of the DFIG. It can be noted that $P_{out} = 1$ pu and $P_{out} = 0.72$ pu correspond to operation at supersynchronous speed range where the variation in the rotor speed of ω_r between the two output power is 0.01 pu. The result is justifiable, as this variation (although insignificant) can be associated to the frequency dependent slip term. When it comes to $P_{out} = 0.25$ pu, corresponding to operations in the subsynchronous speed range, the impedance presents a significantly higher negative resistance accompanied by a shift in the resonance of the DFIG itself. This can be attributed to the operation in subsynchronous speed range associated with a lower value of ω_r that affects the slip term. In addition to the slip term, operation in the subsynchronous speed range (as mentioned in the previous subsection) corresponds to the operation of the GSC as a rectifier. Based on the results presented in [29], it has been hinted that the GSC operated as a rectifier presents a negative admittance for the subsynchronous frequency range that is dependent on α_{dc} .

To further evaluate the impact of the GSC dc-link voltage closed-loop controller bandwidth in the subsynchronous speed range, a frequency sweep of the DFIG impedance for output power corresponding to $P_{out} = 0.25$ pu and $Q_{out} = 0$ pu has been performed. All other parameters are maintained as in Fig. 5.13. The result is depicted in Fig. 5.16. It can be observed that,

the impact of α_{dc} on the impedance is small as in Fig. 5.13. However, in case of subsynchronous speed range (GSC operated as a rectifier), a higher bandwidth of the controller results in a relatively higher negative resistance. The contrary has been observed for operation in the supersynchronous speed range (see Fig. 5.13)

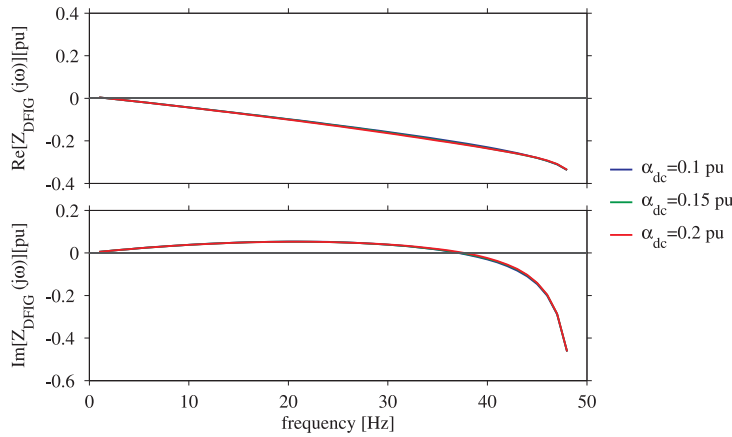


Fig. 5.16 DFIG impedance for varied dc-link controller bandwidth for subsynchronous speed range. $\omega_r = 0.9$ pu. $\alpha_{dc} = 0.1$ pu (blue), $\alpha_{dc} = 0.15$ pu (green), and $\alpha_{dc} = 0.2$ pu (red)

5.3 Frequency domain analysis for transmission line

In Chapter 4, Section 4.3, the derivation for the grid admittance of a radial series-compensated transmission line has been presented. In the same section, calculation of the grid resonance frequency based on impedance and level of series compensation has been addressed. In this section, the variation of admittance characteristics for different grid configurations and the impact of compensation level is covered.

In a radial configuration, compensation level affects the resonance point of the grid in accordance to

$$f_{res} = f_s \sqrt{\frac{1}{L_{tot}C}} \quad (5.19)$$

where $L_{tot} = L_L + L_T$ with L_L and L_T are the inductance of the transmission line and grid transformer, respectively. C is the value of the selected series compensation. Using frequency sweep, the admittance behavior of a series compensated transmission for various compensation level is depicted in Fig. 5.17. In support to (5.19), a higher level of series compensation is observed to a shift of the resonance point further to the right (i.e. closer to the synchronous frequency of the system).

5.3. Frequency domain analysis for transmission line

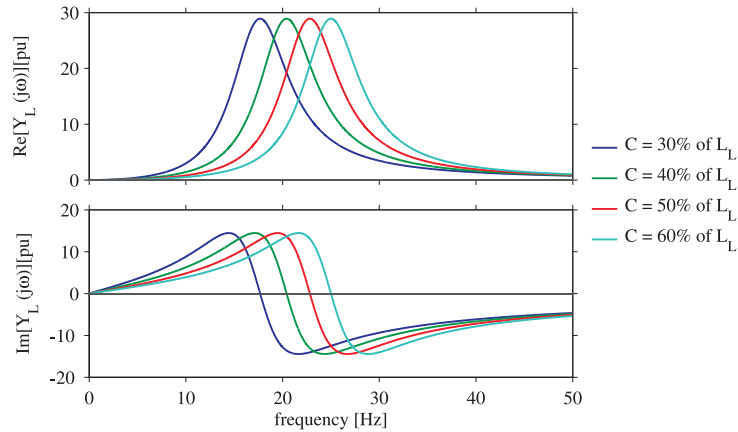


Fig. 5.17 Transmission line admittance, radial configuration, for varied compensation level. C= 30% (purple), C=40% (green), C=50% (red) and C=60% (blue)

To assess the impacts of a different grid configuration, the admittance behavior of a transmission line, based on IEEE SBM with parameters adopted to accommodate the wind farm, is investigated. Fig. 5.18 shows the grid configuration with two parallel transmission line, where one of the lines is series compensated (parameters values found in Appendix B). In a similar manner, the admittance plot for a single compensation level of 50% is shown in Fig. 5.19. The admittance behavior is different as compared with the radial system with a lower and wider resonance pick. At lower frequencies (although this is of less interest), a high conductance is presented as compared to the radial system. In addition, there exist no zero crossing for the imaginary part. The effect of varying the level of series compensation has the same consequences as in the radial system and therefore is not shown here.

With regards to classical SSR problem involving TI, the knowledge of the grid resonance point goes a long way. As the modes of the turbine generator units are known with good accuracy, the resonance in the grid can be modified to avoid these natural mode hence reducing the risk of TI. This eventually simplifying the mitigation process. However, when it comes to SSCI, the behavior of the DFIG varies with the controller parameters and system conditions thereby adding constraint both on the identification and mitigation processes.

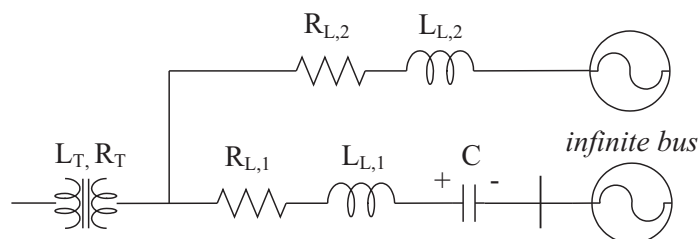


Fig. 5.18 Single-line diagram of transmission line, parallel configuration

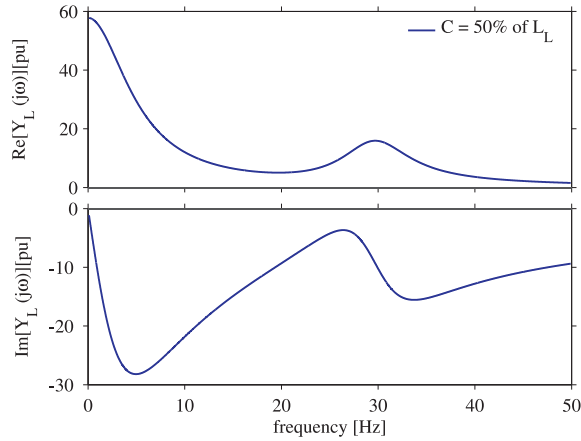


Fig. 5.19 Transmission line admittance, parallel configuration, for C=50%

5.4 Frequency domain stability analysis for interconnected system

In this section the frequency domain stability approach explained in Section 5.1 is applied to the aggregate DFIG generator subsystem and the transmission line subsystem to assess the risk of SSCI. The closed-loop system is expressed as a SISO system, as in Fig. 5.2, in terms of the $Z_{DFIG}(s)$ and $Y_L(s)$. The various detrimental controller parameters and system conditions are assessed to reach on a viable conclusion about the overall system stability.

To verify the obtained frequency-domain analysis, time-domain simulations in PSCAD /EMTDC by employing the system conditions are performed. Fig.5.20 shows the single line representation of the investigated system. For each simulation the output power of the wind farm is ramped up from zero to a preselected value. When steady-state is reached, the circuit breaker in line 2 is opened causing the wind farm to be radially connected to the series compensated transmission line (thus, replicating the Texas-events). The obtained results are presented as system verification.

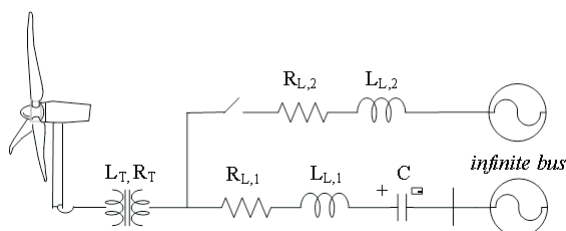


Fig. 5.20 Single-line diagram of the schematic used for time-domain simulation in PSCAD/EMTDC

5.4. Frequency domain stability analysis for interconnected system

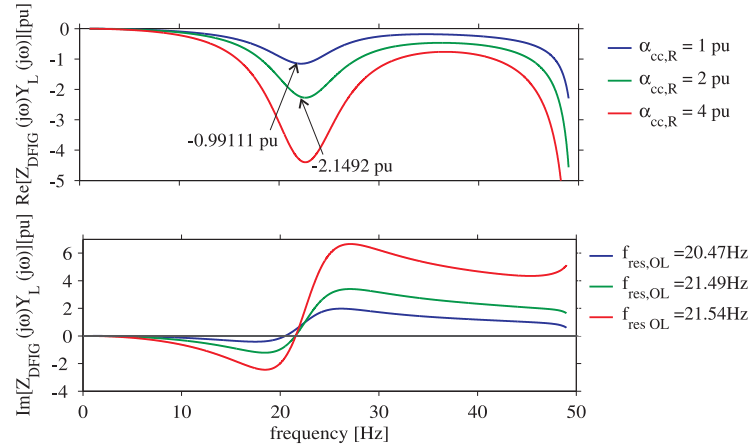


Fig. 5.21 Stability analysis using impedance based Nyquist criterion for varied RSC closed-loop current controller bandwidth. $\alpha_{cc,R} = 1$ pu (blue), $\alpha_{cc,R} = 1$ pu (green), and $\alpha_{cc,R} = 1$ pu (red).

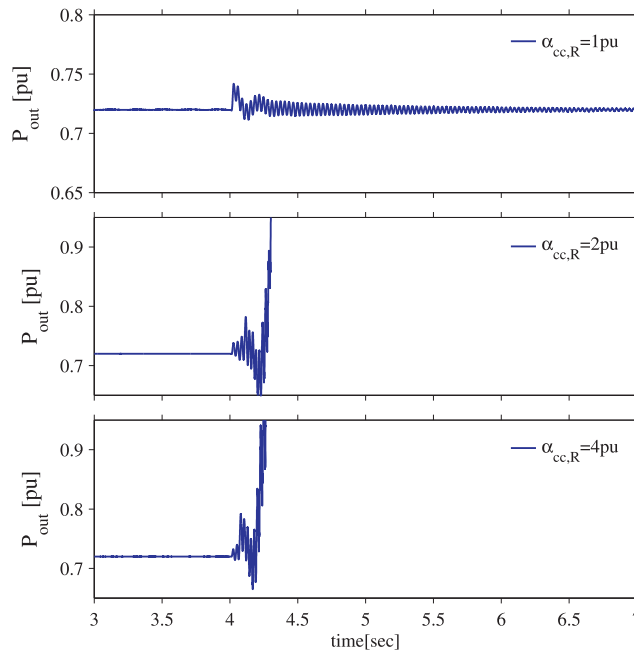


Fig. 5.22 Time-domain simulation of Aggregate DFIG wind farm radially connected to a series compensated transmission for varied RSC current controller bandwidth $\alpha_{cc,R}$. $\alpha_{cc,R} = 1$ pu (upper plot), $\alpha_{cc,R} = 2$ pu (middle plot) and $\alpha_{cc,R} = 4$ pu (lower plot)

5.4.1 Influence of controller parameters on system stability

In subsection 5.2.2, the influence of the RSC parameters where the impact of both the outer power controller and inner current controller over the DFIG impedance have been evaluated in an individual manner. It has been shown that variation in closed-loop current controller bandwidth ($\alpha_{cc,R}$) affects the resistive term over a wide frequency range where the DFIG presents a higher negative resistance for increased value of $\alpha_{cc,R}$. A slight variation on the resonance

Chapter 5. Frequency domain stability analysis and verification

frequency for the DFIG has also been observed with a frequency shift to the right associated with increased value of $\alpha_{cc,R}$. Based on this data, the impedance based Nyquist criterion (see Section 5.1) is applied to the interconnected aggregate DFIG transmission line model (radial configuration) for various $\alpha_{cc,R}$ values at a compensation level of 50%. A compensation level of 50% is chosen as a critical level for most of the results, as the full system experience growing oscillation beyond this level of compensation for the selected controller parameters and system conditions. Fig. 5.21 shows the result for $P_{out} = 0.72$ pu and $Q_{out} = 0$ pu. For this set of results, $\alpha_{cc,F} = 1$ pu whereas $\alpha_{cc,R}$ is varied. Also, $\alpha_{dc} = 0.1$ pu and outer power controller gain and integrator time-constant of $k_{i,P} = 5$ pu and $T_{i,P} = 2$ sec, respectively have been considered.

In reference to Fig. 5.21, a significant impact of the RSC current controller on the overall stability of the system is observed. For an open-loop resonance that varies from 20.47 Hz to 21.54 Hz, $\text{Re}[Z_{DFIG}(j\omega_N)Y_L(j\omega_N)]$ falls below -1 for $\alpha_{cc,R} > 1$ pu. This is a clear indication that the open-loop system encircles -1, implying that the closed-loop system is unstable for the corresponding controller parameters and system conditions. However for $\alpha_{cc,R} = 1$ pu, $\text{Re}[Z_{DFIG}(j\omega_N)Y_L(j\omega_N)] = -0.9911$ pu, i.e, it is very close to -1. To verify the obtained results, a time-domain simulation in PSCAD is performed. The circuit breaker is opened at $t = 4$ sec. The obtained results for $\alpha_{cc,R}$ 1pu, 2pu and 4 pu are depicted in Fig. 5.22. For $\alpha_{cc,R} = 1$ pu, the subsynchronous oscillation dies out slowly, however, for $\alpha_{cc,R} = 2$ pu and $\alpha_{cc,R} = 4$ pu, the system experiences growing oscillation denoting system instability.

For a system resonance of frequency f_N , the current that flows contains two components I_f at the fundamental frequency, f_s and I_{sub} at the subsynchronous frequency f_N . The corresponding rotor current will has components $I_{r,f}$ at $f_s - f_m$ and $I_{r,sub}$ at $f_N - f_m$. Interactions between the various current components result in an additional torque component (i.e in addition to the actual torque) at a frequency $f_s - f_N$ that appears as a complement of the resonance frequency. To further asses this, an Fast Fourier Transformer (FFT) is performed for $\alpha_{cc,R} = 1$ pu to obtain the resonance frequency of the closed-loop system which was found to be $f_{res} = 30.625$ Hz. This is electrical close to the $f_{res,OL} = 20.47$ that has a complementary frequency corresponding to 29.53 Hz. Again, it should be noted that $f_{res,OL}$ is the open-loop resonance and in no terms should be considered as the closed-loop resonance. However, it could be used to determine the vicinity of the system resonance which can be employed for further system assessment.

5.4. Frequency domain stability analysis for interconnected system

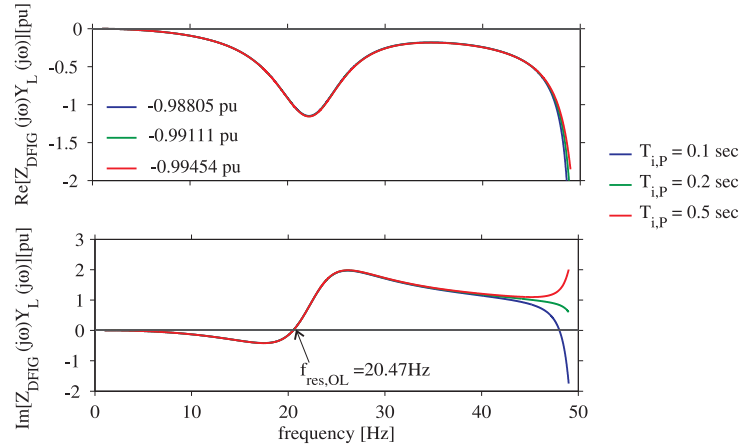


Fig. 5.23 Stability analysis using impedance based Nyquist criterion for varied RSC power controller integrator time-constant. $T_{i,P} = 0.1$ sec (blue), $T_{i,P} = 0.2$ sec (green), and $T_{i,P} = 0.5$ sec (red).

Referring back to Section 5.2.2, another RSC controller parameter that caught attention is the integrator time-constant, $T_{i,P}$. In Fig. 5.11, it has been shown that, variation in $T_{i,P}$, for a value below 0.2 sec, significantly affected the resistive term of the DF IG impedance for the frequency range closer to the synchronous frequency. Based on this result, the impedance based Nyquist criterion has been employed for the same system conditions of the DF IG as well as a series compensation level corresponding to 50%. Fig. 5.23 shows the obtained results. The overall system stability criteria show a very small variation for varied $T_{i,P}$ value. This is also supported as the variation in DF IG impedance (due to $T_{i,P}$) occurs at a higher frequency, which is further away from the system open-loop resonance frequency. In summary, although the integrator time-constant affects the impedance behavior of the DF IG itself, its impact on the overall system stability is minimal.

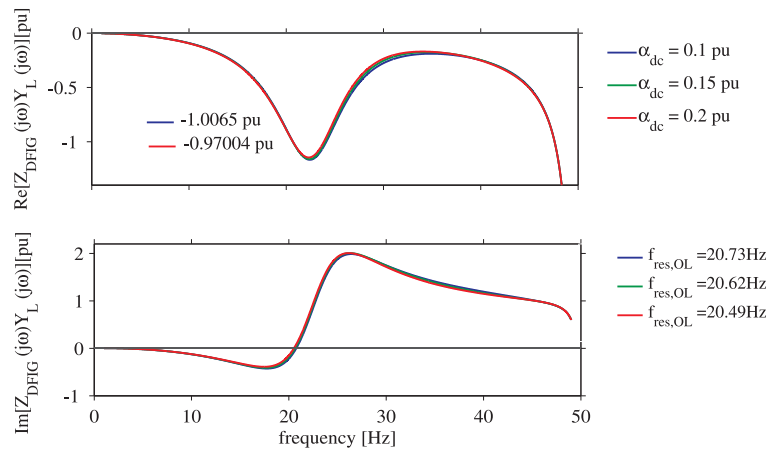


Fig. 5.24 Stability analysis using impedance based Nyquist criterion for varied dc-link voltage controller bandwidth operating in supersynchronous speed range. $\alpha_{dc} = 0.1$ pu (blue), $\alpha_{dc} = 0.15$ pu (green), and $\alpha_{dc} = 0.2$ pu (red).

Moving with the analysis of the GSC, the impact of the GSC closed-loop current controller

Chapter 5. Frequency domain stability analysis and verification

bandwidth, $\alpha_{cc,F}$ has been shown to have less influence on the DFIG impedance (see Section 5.2.3). A similar result is obtained for the overall system stability and therefore, is not discussed further in this thesis. However, in the same section and Section 5.2.4, the impact of dc-link controller, although not significant, showed variation based on whether the GSC is operated as a rectifier or as an inverter.

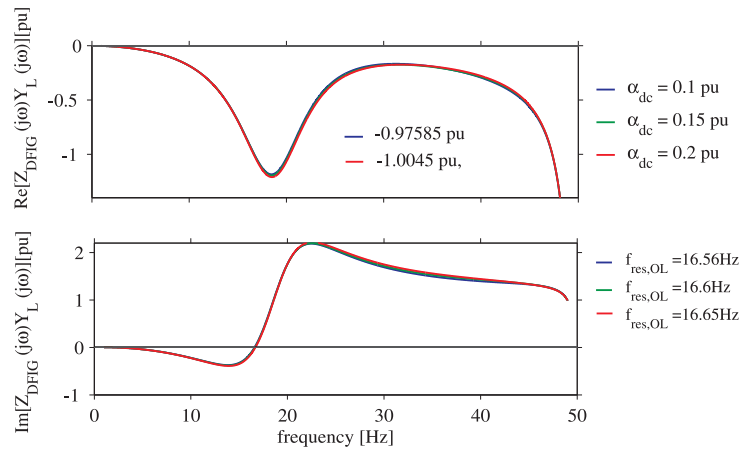


Fig. 5.25 Stability analysis using impedance based Nyquist criterion for varied dc-link voltage controller bandwidth operating in subsynchronous speed range. $\alpha_{dc} = 0.1$ pu (blue), $\alpha_{dc} = 0.15$ pu (green), and $\alpha_{dc} = 0.2$ pu (red).

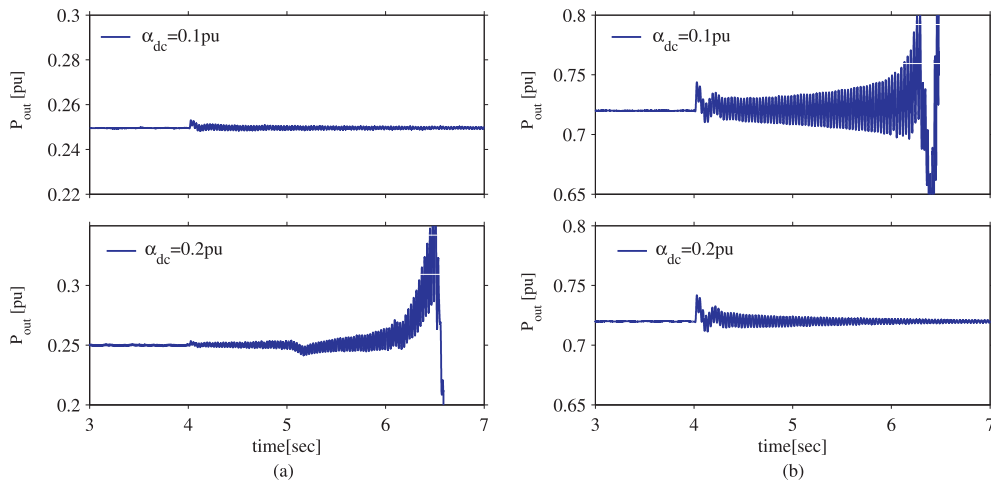


Fig. 5.26 Time-domain simulation of Aggregate DFIG wind farm radially connected to a series compensated transmission for varied dc-link voltage controller bandwidth α_{dc} . *left figure* : $P_{out} = 0.25$ pu and 35% compensation, *right figure* : $P_{out} = 0.72$ pu and 51% compensation, $\alpha_{dc} = 0.1$ pu (*upper plots*), and $\alpha_{dc} = 0.2$ pu (*lower plots*)

Fig. 5.24 and Fig. 5.25 show the results for the impedance based stability analysis for supersynchronous and subsynchronous speed ranges, respectively. A critical compensation level of 35% and 51% are selected for subsynchronous and supersynchronous speed ranges. For supersynchronous speed ranges, a higher α_{dc} value moves the curve towards the stable region whereas

5.4. Frequency domain stability analysis for interconnected system

the opposite holds for subsynchronous speed ranges. However it should be noted that the above results hold only around the critical compensation level and not for higher compensation level. This is in harmony with earlier results as the dc-link voltage controller parameter is shown to have a small impact on the DFIG impedance.

Verification using time-domain simulation is shown in Fig. 5.26. The figure on the left-hand side (marked (a)) shows the results for subsynchronous speed of $\omega_r = 0.9$ pu at a compensation level of 35% while the right-side figure (marked (b)) shows results for super synchronous speed of $\omega_r = 1.1$ pu at 51% of series compensation. The time domain results obtained collaborate the obtained analytical conclusion.

5.4.2 Influence of operating condition on overall system stability

The effect of operating conditions with respect to wind speed (i.e. related to P_{out}) on the impedance of the DFIG has been presented in Section 5.2.4. Here, the impact of these operation speeds on the overall system stability is evaluated. Fig. 5.27 shows the result for two speeds, $\omega_r = 1.1$ pu ($P_{out} = 0.72$ pu) and $\omega_r = 0.9$ pu ($P_{out} = 0.25$ pu). Both RSC and GSC closed-loop current controller bandwidths have been set to 1 pu whereas $k_{i,P} = 5$ pu, $T_{i,P} = 0.2$ sec and $\alpha_{dc} = 0.1$ pu have been considered.

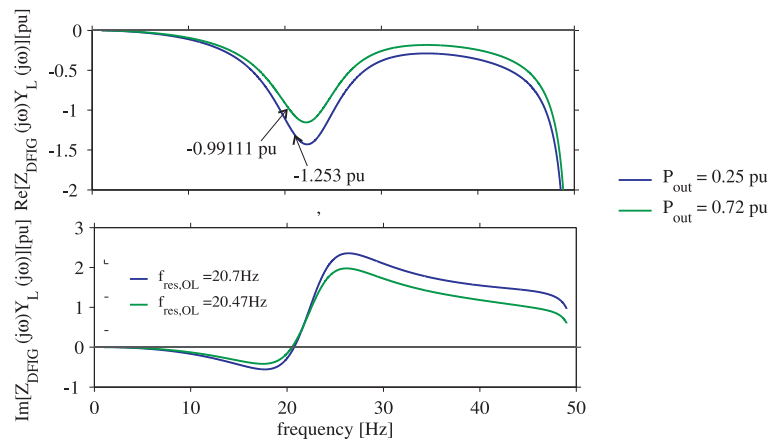


Fig. 5.27 Stability analysis using impedance based Nyquist criterion for different output power at 50% compensation. $P_{out} = 0.25$ pu (blue), $P_{out} = 0.72$ pu (green).

As expected, a higher wind speed (operating in supersynchronous speed) leads to a more stable system as compared to lower wind speed. The impedance behavior of the DFIG has also been shown to be affected (see Fig. 5.15) by both the subsynchronous slip, whose magnitude increases with decreasing value of ω_r , and the impedance of GSC when operated as a rectifier. As the admittance of the transmission line is not varied (for Fig. 5.27), the aforementioned attributes can be extended to explain the overall system stability. Time domain simulation collaborating these results are shown in Fig.5.28

Chapter 5. Frequency domain stability analysis and verification

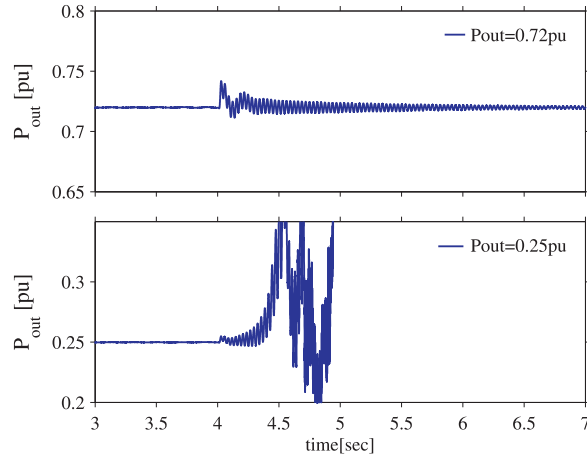


Fig. 5.28 Time-domain simulation of Aggregate DFIG wind farm radially connected to a series compensated transmission for varied output power P_{out} . $P_{out} = 0.72$ pu (upper plot), and $P_{out} = 0.25$ pu (lower plot)

Finally, in Section 5.3, the influence of compensation level on a radial configuration has been evaluated. Fig. 5.29 shows the obtained results for different levels of series compensation.

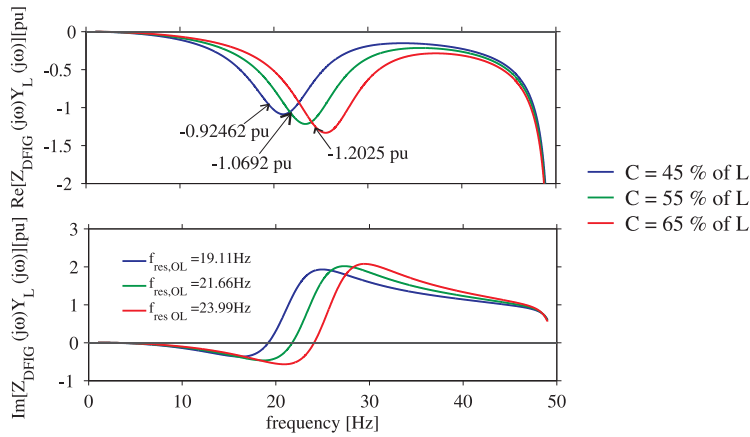


Fig. 5.29 Stability analysis using impedance based Nyquist criterion for various level of series compensation (radial configuration). $C = 45\%$ (blue), $C = 55\%$ pu (green) and $C = 65\%$ (red).

The effect of the compensation level on the overall stability curve is to shift the open-loop resonance to the right and at the same time cause a deeper dip on the $\text{Re}[Z_{DFIG}(j\omega_N)Y_L(j\omega_N)]$ curve. Therefore, a high compensation level increases the risk of system instability as the open-loop gain can exceed -1 at the open-loop resonance frequency, as shown in Fig. 5.29. To incorporate the frequency-domain analysis, time-domain simulation results replicating this system condition are presented in Fig. 5.30. As anticipated from the frequency-domain stability analysis, is stable system for a compensation level of 45%, whereas the system becomes unstable for compensation level of 55% and 65%. The frequency of the resulting oscillation are 31.98 Hz, 30.1526 Hz and 27.92 Hz for 45%, 55% and 65% at complementary frequency of 18.02 Hz, 19.8474 and 22.08 Hz, respectively.

5.4. Frequency domain stability analysis for interconnected system

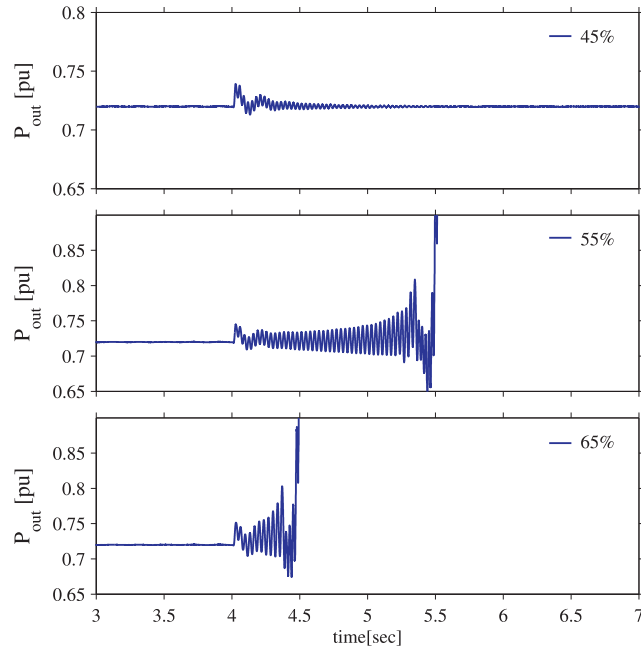


Fig. 5.30 Time-domain simulation of Aggregate DFIG wind farm radially connected to a series compensated transmission for varied level of series compensation. 45% (*upper plot*), 55% (*middle plot*) and 60% (*lower plot*)

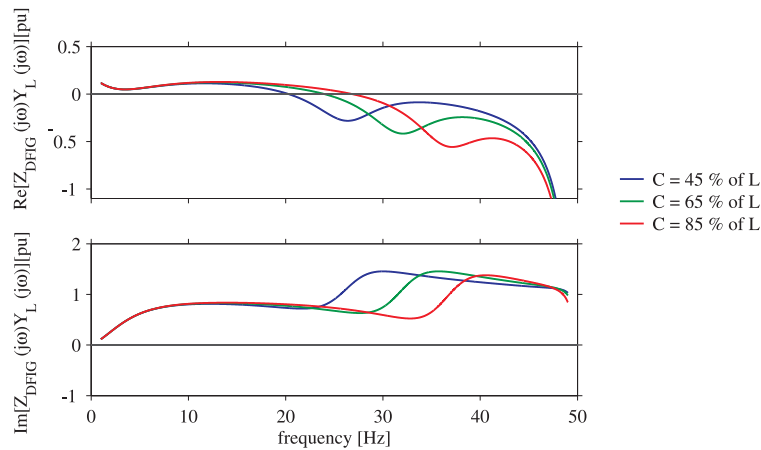


Fig. 5.31 Stability analysis using impedance based Nyquist criterion for various level of series compensation - parallel configuration. $C = 45\%$ (blue), $C = 65\%$ pu (green) and $C = 85\%$ (red).

At last, the impact of the grid configuration based on the stability analysis of a parallel configuration is presented in Fig. 5.31. The result show no risk of open-loop resonance for sub-synchronous frequencies that can be attributed to admittance characteristics of the transmission line. In actual terms, the parallel configuration eliminated the direct energy exchange that could have occurred between the control system of the wind turbine and the capacitance on the series compensation transmission line, as part of this energy is directed through the parallel connected transmission line.

5.5 Conclusion

In this chapter, the risk of SSCI in a DFIG based wind farm connected to a series compensated transmission line has been investigated using an impedance-based frequency domain approach. The system has been modeled as a SISO feedback system, where two subsystems have been defined: an aggregate DFIG and a transmission line on series compensation. The DFIG subsystem has been expressed in terms of its impedance transfer function, $Z_{DFIG}(s)$, whereas the transmission line is given in terms its admittance transmission function, $Y_L(s)$. Frequency-domain impedance/ admittance behaviors of the individual subsystems have been investigated with respect to various parameters and system conditions. In the subsynchronous frequency range, the DFIG impedance is shown to present a negative resistance for the entire subsynchronous frequency range. The DFIG also exhibits an inherent resonance that occurs in the frequency range 35 - 40 Hz, which varies with respect to control parameters and system conditions. From the analysis, it has been drawn that the following conditions influence the impedance behavior of the DFIG subsystem

1. The closed-loop bandwidth of RSC current controller. The higher the RSC closed-loop current controller bandwidth, the higher the negative resistance presented by the DFIG. A slight shift of the DFIG resonance frequency is shown with lower resonance frequency associated to higher $\alpha_{cc,R}$
2. The outer-loop power controller parameter. The higher the controller gain the higher the DFIG resonance frequency. A lower resistance is observed for a higher gain for a narrow frequency range between 45 - 50 Hz. The integrator time-constant, for a frequency range 40 -50 Hz is shown to affect the DFIG resistance significantly.
3. The amount of active power generated by the DFIG. The more power is produced by the DFIG, the less negative the DFIG resistance. A slightly higher resonance frequency is exhibited for higher output power.
4. The closed-loop bandwidth of dc-link voltage controller. The impact varies whether the GSC converter is operated as a rectifier or as an inverter. For inverter operation, the higher the α_{dc} , the less negative the DFIG resistance. For rectifier operation, the opposite holds. However the variation is very small.

The admittance property of the transmission line considering two configurations, has been evaluated. For a radial system, the level of series compensation is shown to affect the resonance frequency of the transmission line. This is associated with the higher compensation level. Variation in grid configuration is also shown to have an impact on both the conductance and resonance frequency for the transmission line subsystem. In comparison to the radial configuration, the parallel grid configuration has been shown to have a lower conductance.

The overall system stability has been evaluated using an impedance-based Nyquist criterion, where the open-loop system stability is used to assess the risk for SSCI. It has been concluded that, the higher the RSC current controller bandwidth, the higher the risk of SSCI even at a

5.5. Conclusion

reasonable level of series compensation. It has been shown that, the dc-link voltage closed-loop controller bandwidth has an impact about the critical level of series compensation where a higher α_{dc} values improves stability in rectifier operation of the GSC and a lower α_{dc} value improves the stability in inverter operation of the GSC. Based on the above conclusions, the RSC controller parameter, specifically $\alpha_{cc,R}$, plays a major role in shaping the DFIG impedance in order to eliminate the risk of SSCI for the investigated system.

It should be noted that, the stability analysis performed has been for a particular grid configuration and control parameter. However, the method is not restricted to the configurations presented in this chapter but rather can be extended to include complex grid configuration or alternate DFIG controller configuration.

Chapter 5. Frequency domain stability analysis and verification

Chapter 6

Utilization of DFIG Controller for SSR Mitigation

6.1 Introduction

In an attempt to minimize the impact caused by SSCI, mitigation for this kind of interaction has become the focus of research in recent years. Some of the reported mitigation techniques involve the installation of Static Synchronous Compensator (STATCOM) [57] [58], Static Var Compensator (SVC) [59] and other external devices like Gate-Controlled Series Capacitor (GCSC) [60] and Thyristor Controlled Series Capacitors (TCSC) [61] [62]. Other SSCI mitigation techniques involve the modification of the DFIG controller. A damping controller, described in [63], uses the measured current and voltage to act on the RSC controller. The damping controller parameters are determined by using the state-space model of the turbine. Another type of damping controller, proposed in [64], involves a derivative current controller loop, a second order low-pass filter and a lead-lag compensator that is implemented on the RSC.

A different approach is proposed in [65], that involves the addition of a virtual impedance in series with the PI controller of the RSC current controller loop. An impedance-based stability approach is used to evaluate the impact of the proposed damping approach. The author also proposes the addition of a parallel virtual impedance through the GSC. However, results that support this are not reported in the paper. The work presented in [66] [67], proposes the use of subsynchronous suppression filters in the DFIG controller. The approach involves the addition of a notch filter to the RSC current-controller loop. The filter is utilized to filter out the SSR mode thereby eliminating the possible interaction that could occur, hence, stabilizing the SSCI.

When it comes to mitigation techniques, which improves the DFIG's or the network's behavior making it more passive towards the interaction (passive techniques), the work presented in [68] suggests bypassing the series capacitors or adjusting the DFIG control parameters [68] [69] [70], especially the gain of the RSC current controller, in events of an SSCI.

This chapter presents possible mitigation techniques that can be employed to the DFIG wind turbine. Both frequency-domain analysis and time-domain simulation will be used to evaluate

the effectiveness of the proposed methods.

6.2 DFIG turbine modification for SSR mitigation

In previous chapters, it has been established that the problem with SSCI in DFIG based wind farms is due to the energy interaction that occurs between the wind farm control system and the resonance conditions in the series compensated transmission grid. Using an impedance-based approach, factors affecting this interaction have been evaluated from the perspectives of the DFIG turbine impedance and as well as operating conditions of the system.

In this section, SSCI mitigation through variation of the DFIG system impedance is proposed. Here, two approaches are considered: the first involves the variation of the DFIG controller parameters to modify the DFIG input impedance (here referred to as passive mitigation), while the second approach involves the introduction of a proportional damping controller to the DFIG control system to enhance the system damping for the desired frequency range (referred to as active mitigation).

6.2.1 Controller parameter variation for SSR mitigation - Passive mitigation

When SSR is triggered, unless and otherwise SSR mitigation devices are installed in the network, the only counteraction that can be taken by the wind farm operator is to disconnect the generation plant, in order to prevent further damage due to the uncontrolled energy exchange between the farm and the grid. In order to keep the wind farm in service, it would be necessary to vary either the DFIG impedance or the impedance of the grid seen from the point of common coupling, to guarantee that the overall system is passive at the system resonance.

Based on the frequency-domain analysis performed in Chapter 5, the following conclusions have been drawn:

- The RSC closed-loop current controller bandwidth α_{cc} has a major impact on the negative resistance of the DFIG with a lower α_{cc} value contributing to a less negative resistance
- The impact of the dc-link closed-loop current controller bandwidth α_{dc} varied whether the generator is operated in subsynchronous or supersynchronous speed range.
- A lower output power level corresponding to operation in subsynchronous speed range leads to a higher negative resistance.

Expanding on this, the variation in DFIG input resistance at the zero crossing of its reactance (here referred to as the DFIG's resonant point) and the shifting of this resonance point for different values of α_{cc} and α_{dc} is presented in Fig. 6.1. Operating condition at supersynchronous speed range has been considered. As can be observed from the left plot, minimal negative resistance around the DFIG resonance point is observed at $\alpha_{cc} = 0.5$ pu and $\alpha_{dc} = 0.2$ pu. Fig. 6.2

6.2. DFIG turbine modification for SSR mitigation

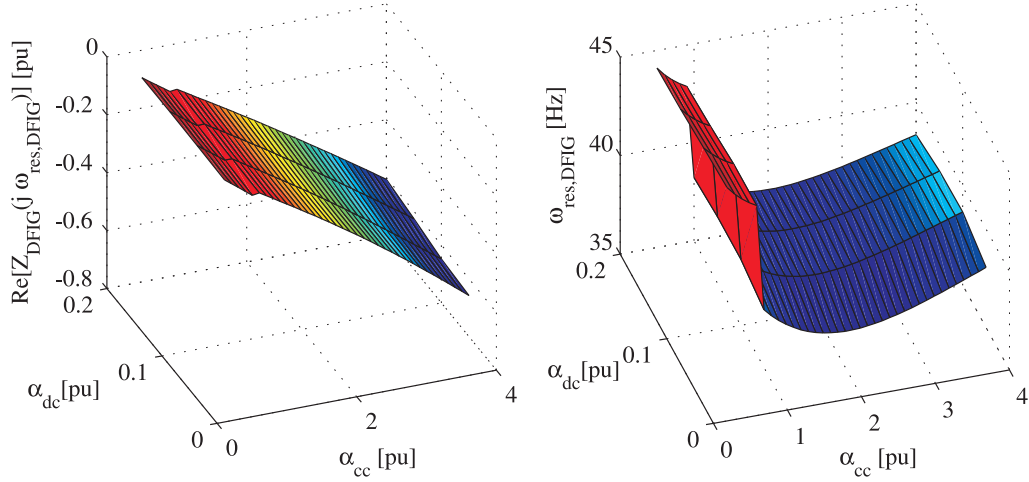


Fig. 6.1 Evaluation of parameter influence on DFIG resistance at DFIG resonance frequency. α_{cc} and α_{dc} varied. $P_{out} = 0.72$ pu, $Q_{out} = 0$ pu

shows a similar plot for operating condition in the subsynchronous speed range. In the result presented, $\alpha_{cc} = 0.5$ pu and $\alpha_{dc} = 0.05$ pu appear to show the minimal negative resistance. When observing the right plots of Fig. 6.1 and Fig. 6.2, a significant variation in DFIG resonance frequency is observed for $\alpha_{cc} < 1$ pu with the resonance frequency shifting further to the right (closer to the synchronous frequency). Based on the results shown, lowering the RSC closed-loop current controller bandwidth serves as a good criterion for shaping the input impedance of the DFIG turbine both in the subsynchronous and supersynchronous speed range. From the figures, it can also be observed that variation in α_{dc} , has very small impact on the $\text{Re} [Z_{DFIG} (j\omega_{res,DFIG})]$

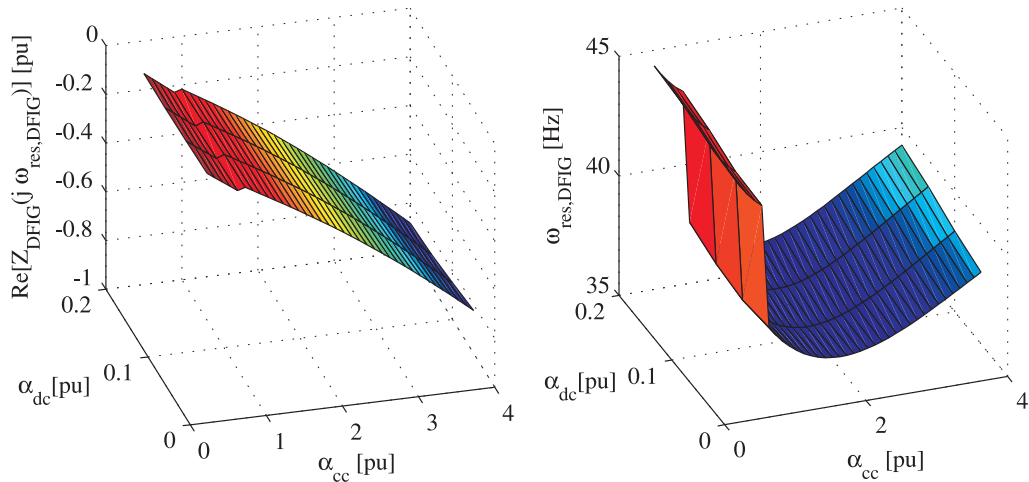


Fig. 6.2 Evaluation of parameter influence on DFIG resistance at DFIG resonance frequency. α_{cc} and α_{dc} varied. $P_{out} = 0.25$ pu, $Q_{out} = 0$ pu

6.2.2 SSR mitigation using controller variation - Active SSR mitigation

Controller modification based countermeasures have the advantage of being cheap as it does not require the installation of expensive additional mitigation devices and can easily be implemented within the DFIG controller. For a DFIG based wind turbine, there exist two alternatives: one considering the GSC controller and the other considering the RSC controller. In [71], the author investigates the potential of the GSC controller for SSR mitigation using residual-based analysis and time-domain simulations in Matlab. An auxiliary proportional damping controller implemented on the GSC utilizing the series capacitor voltage has been demonstrated to have effective damping effect. However, in [63], comparison of the GSC and RSC controller loops for SSCI mitigation by adding a supplementary damping controller utilizing multiple input signal has demonstrated that the supplementary controller utilizing the GSC showed good results around the normal level of series compensation, but failed for higher level of series compensation. On the other hand, the RSC based supplementary controller showed good performance even for high level of series compensation. The work presented in [72], that evaluates the optimal location for a proportional based supplementary damping controller, also identifies various controller input signals for the proposed damping controller, based on residual analysis and root-locus method. It has been concluded that the capacitor voltage is the ideal signal and the GSC is the ideal location. However in the author's recent work [4], it is clearly pointed out that the RSC inner current controller loop is the best location for inserting the damping controller.

Returning to the analytical results presented in the previous chapters (see Section 5.2.3), the impact of the GSC controller on the impedance behavior has been demonstrated to be minimal, which hinders the use of this controller for mitigation purposes. However, the RSC controller (especially the RSC current controller) has been shown to have a significant impact on the frequency response of the DFIG in the subsynchronous frequency range. Therefore, in this subsection, modification of RSC controller for SSCI damping has been considered.

6.2.3 Proposed SSR mitigation

The proposed active mitigation technique for SSCI consists of two stages: an estimation stage and damping controller stage. The estimation stage consists of an estimation algorithm used to extract the subsynchronous component from the measured signal. This serves as an input to the damping controller stage. The purpose of the damping controller stage is to enhance the damping of the system for the particular frequencies of interest. The proposed method has been implemented as part of the RSC current controller loop.

Estimation Method

The estimation algorithm (EA) is used to estimate the subsynchronous component in the measured power of the DFIG. Due to the terminal voltage v_g containing a subsynchronous component, the terminal power P_{out} will have an average component and an oscillatory component as

6.2. DFIG turbine modification for SSR mitigation

$$P_{out}(t) = P_{out,av}(t) + P_{out,osc}(t) \quad (6.1)$$

The terminal power can be expressed in terms of its average and a complex phasor $\underline{P}_{out,osc} e^{j\theta_{osc}(t)}$ where $\theta_{osc}(t) = \omega_{osc}(t)t$ is the oscillation angle. The expression (6.1) can be rewritten as

$$P_{out}(t) = P_{out,av}(t) + \frac{1}{2}\underline{P}_{out,osc}(t)e^{j\theta_{osc}(t)} + \frac{1}{2}\underline{P}_{out,osc}^*(t)e^{-j\theta_{osc}(t)} \quad (6.2)$$

From the above expression, it can be deduced that the terminal power is partitioned into three frequency components having frequencies at 0, ω_{osc} and $-\omega_{osc}$. According to [73], by rearranging (6.2) and by applying low-pass filtering, the oscillator term $\tilde{P}_{out,osc}$ and the average $\tilde{P}_{out,av}$ can be estimated from the input signal as

$$\begin{aligned} \tilde{P}_{out,av}(t) &= H_{av} [P_{out}(t) - \tilde{P}_{out,osc}(t)] \\ \tilde{P}_{out,osc}(t) &= H_{osc} \left[\left\{ 2P_{out}(t) - 2\tilde{P}_{out,av}(t) - \tilde{P}_{out,osc}^* e^{-j\theta_{osc}(t)} \right\} e^{-j\theta_{osc}(t)} \right] \\ \tilde{P}_{out,osc}(t) &= \frac{1}{2}\tilde{P}_{out,osc}(t)e^{j\theta_{osc}(t)} + \frac{1}{2}\tilde{P}_{out,osc}^*(t)e^{-j\theta_{osc}(t)} \end{aligned} \quad (6.3)$$

where H_{av} and H_{osc} are the transfer function of the low-pass filters for the average and the oscillatory component, respectively. Here, a first order low-pass filter having cutoff frequency of α_{LPF} as in (6.4) has been considered for the filters.

$$H_{av}(s) = H_{osc}(s) = \frac{\alpha_{LPF}}{s + \alpha_{LPF}} \quad (6.4)$$

Fig. 6.3 shows the block-diagram representation of the implemented estimation algorithm. The algorithm shown in Fig. 6.3 can be expressed in state-space form as [73]

$$\frac{d}{dt} \begin{bmatrix} \tilde{P}_{out,av} \\ \tilde{P}_{out,osc} \\ \tilde{P}_{out,B} \end{bmatrix} = \begin{bmatrix} -\alpha_{LPF} & -\alpha_{LPF} & 0 \\ -2\alpha_{LPF} & -2\alpha_{LPF} & -\omega_{osc} \\ 0 & \omega_{osc} & 0 \end{bmatrix} \begin{bmatrix} \tilde{P}_{out,av} \\ \tilde{P}_{out,osc} \\ \tilde{P}_{out,B} \end{bmatrix} + \begin{bmatrix} \alpha_{LPF} \\ 2\alpha_{LPF} \\ 0 \end{bmatrix} P_{out}(t) \quad (6.5)$$

Using the state-space, the frequency response for the Low-Pass Filter based Estimation Algorithm (LPF-EA) can be evaluated. The response of the system from the input $P_{out}(t)$ to the oscillator component $\tilde{P}_{out,osc}$ and the average components $\tilde{P}_{out,av}$ are presented in Fig. 6.4. The measured signal is assumed to contain a 35 Hz oscillatory frequency and a 1 Hz cutoff frequency is considered for the EA.

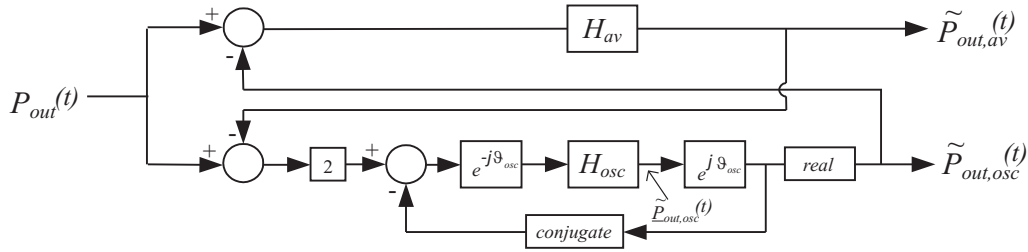


Fig. 6.3 Block diagram of LPF-based estimation algorithm

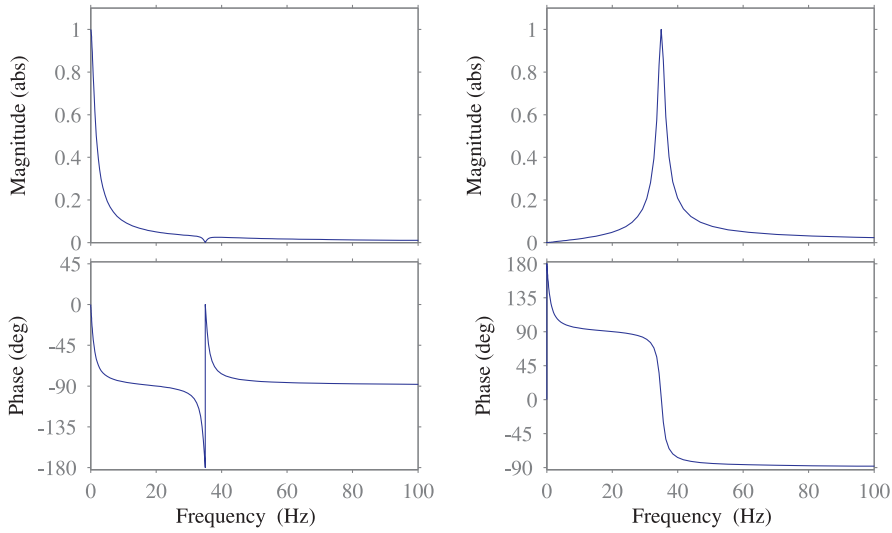


Fig. 6.4 Frequency response of low-pass filter based estimation algorithm from $P_{out}(t)$ to $\tilde{P}_{out,av}$ (left figure) and $\tilde{P}_{out,osc}$ (right figure). A cutoff frequency of 1 Hz for first order filter

From Fig. 6.4, it can be observed that the LPF-EA has the property of a resonant filter having a center frequency ω_{osc} . As can be noted, the algorithm presents a 1 pu gain and 0 phase shift at the oscillatory frequency ω_{osc} (see Fig. 6.4, right plot). Although not visible, it also presents a notch at the average frequency of 0 Hz. The algorithm for the average component presents a 1 pu and 0 phase shift at 0 Hz and a notch at the oscillatory frequency of ω_{osc} (see Fig. 6.4, left plot). According to the analysis performed in [27], the selection of bandwidth for the estimator is a tradeoff between speed of response and the damping of the system. It is recommended in [74] to set the cutoff frequency of the filter to be one decade smaller than the frequency of the signal to be estimated.

Subsynchronous damping controller

The proposed subsynchronous damping controller utilizes the estimated subsynchronous power component as an input. For the controller at hand, the following assumptions have been considered

6.2. DFIG turbine modification for SSR mitigation

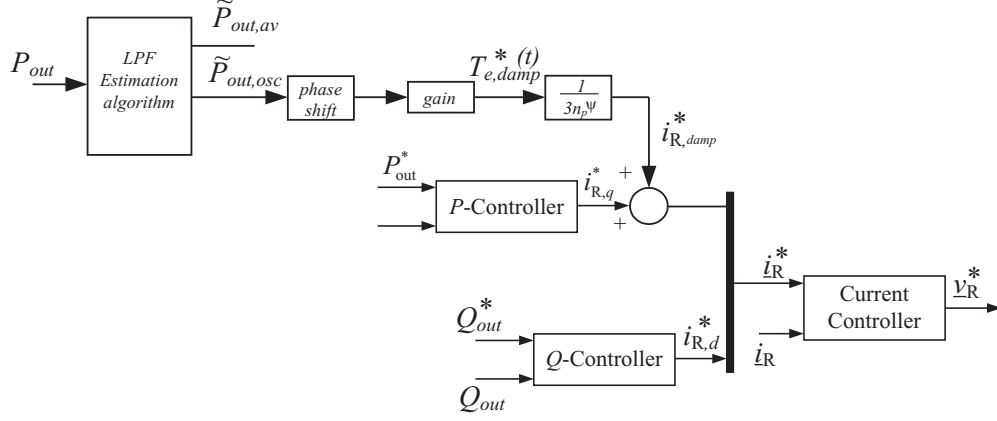


Fig. 6.5 Block diagram representation of subsynchronous damping controller implemented on RSC current controller

- The network presents a positive damping for the supersynchronous component [26]. Therefore supersynchronous components are not considered.
- The subsynchronous oscillatory frequency is known with good accuracy. This is not true in case of SSCI as the oscillatory frequency varies depending on the controller parameters and operating condition

So as to obtain a damping torque reference around the oscillator frequency, a phase shift of 90° is introduced on the estimated subsynchronous power component. Here, extra care should be taken as phase shift other than 90° degree would result in an introduction of a synchronization torque that would instead enhance the subsynchronous oscillation. The generated reference is then multiplied by a gain thereby creating the required damping torque reference for the RSC controller. Fig. 6.5 shows the block-diagram representation of the implemented damping controller. To obtain the damping torque reference current ($i_{R,damp}^*$), the torque equation of (6.6) has been used.

$$T_e = 3n_p \Psi_{s,d} i_{R,q} \quad (6.6)$$

To evaluate the impact of the implemented damping controller on the frequency impedance of the DFIG turbine, a steady-state representation of the estimation algorithm with the proportional damping controller has been included in the mathematical model. The frequency-domain impedance obtained using the mathematical model is here presented in Fig. 6.6. Operating condition corresponding to $P_{out} = 0.72$ pu, $Q_{out} = 0$ pu, $\alpha_{cc} = 1$ pu and $\alpha_{dc} = 0.2$ pu have been used. The cut-off frequency of $\alpha_{LPF} = 0.02$ pu has been set for the low-pass filters and the estimator is centered at 15 Hz. As can be seen from the figure, the inclusion of the damping controller results in a lower negative resistance in the frequency of interest, thereby improving the negative resistance presented by the DFIG turbine.

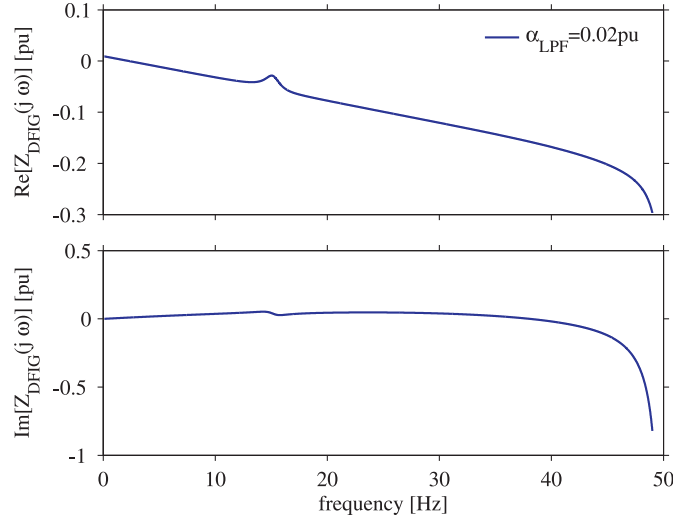


Fig. 6.6 Impedance of a DFIG turbine with a proportional damping controller

6.3 Frequency domain stability analysis for modified system

In Chapter 5, frequency-domain analysis has been used to evaluate the impact of various controller parameters and operating conditions on the behavior of the DFIG turbine. An impedance based stability criterion has also been introduced to measure the risk of instability based on the impedance and admittance behavior of the DFIG farm and the series-compensated transmission line. In this section, similar approach will be applied to inspect the effect of the proposed mitigation techniques on the stability of the overall system. Section 6.3.1 presents the evaluation for passive mitigation technique, while the evaluation for the active mitigation technique is presented in Section 6.3.2

6.3.1 Passive mitigation

The analysis is performed in steady-state conditions. Evaluating the results depicted in Fig. 6.7, when the generator is operated in supersynchronous speed (high-wind speed), a RSC closed-loop current controller bandwidth of 0.5 pu and a closed-loop dc-link voltage controller bandwidth of $\alpha_{dc} = 0.2$ pu showed the highest stability margin. With the increase of the RSC closed-loop current controller bandwidth, the $\text{Re} [Z_{DFIG}(j\omega_{res,OL}) Y_L(j\omega_{res,OL})]$ falls below the -1, clearly indicating the risk for instability.

6.3. Frequency domain stability analysis for modified system

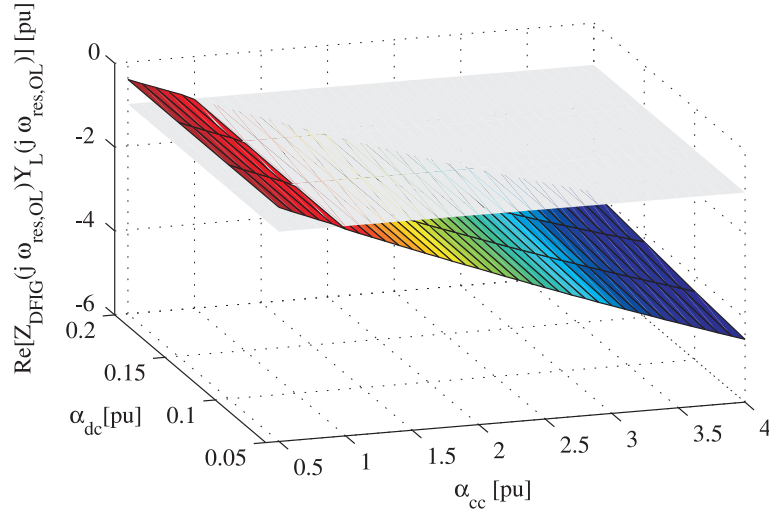


Fig. 6.7 Evaluation of parameter influence on stability using impedance based Nyquist criterion. α_{cc} and α_{dc} varied. $P_{out} = 0.72$ pu, $Q_{out} = 0$ pu and 55% compensation,

To measure the impact of the operating point, the impedance-based Nyquist criterion has been employed to evaluate system stability through variation of P_{out} and α_{cc} . Fig. 6.8 shows the obtained results. As can be seen, for lower output power corresponding to low wind speed, a low closed-loop current controller bandwidth of $\alpha_{cc} = 0.5$ pu ensures system stability whereas values between 0.5-0.85 pu ensures stability for higher output power levels. This is partially related to the higher negative resistance associated with a higher negative slip at low wind speed. A slower current controller contributes to a lower virtual resistance thereby lowering the negative resistance presented by the DFIG turbine.

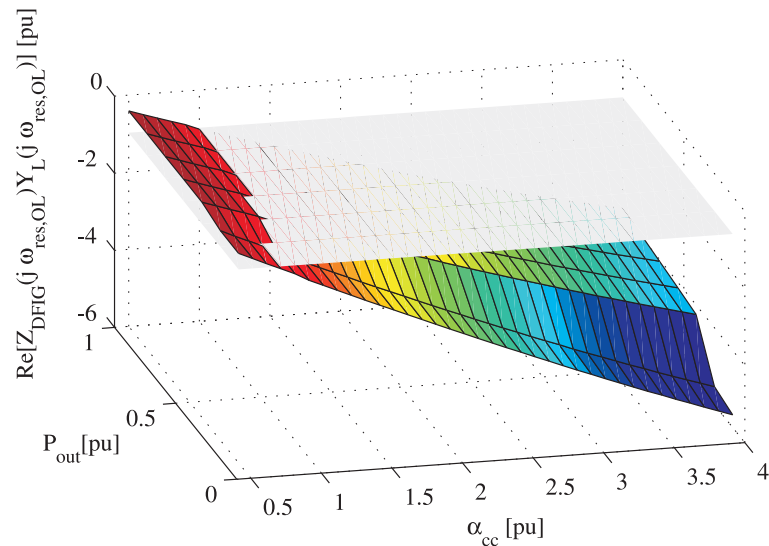


Fig. 6.8 Evaluation of parameter and operating point influence on stability using impedance based Nyquist criterion. α_{cc} and P_{out} varied. $\alpha_{dc} = 0.2$ pu, $Q_{out} = 0$ pu and 55% compensation,

6.3.2 Active mitigation

In this section, the stability analysis for the system using the proposed damping controller explained in Section 6.2.3 will be presented. Here accurate knowledge of system parameter and SSR oscillatory frequency ω_{osc} is assumed. The impedance based Nyquist stability criterion explained in Section 5.1 is used for the analysis. A cut-off frequency of $\alpha_{LPF} = 0.02$ pu is considered. Fig. 6.9 shows the result for compensation level corresponding to 55%. have been set. The dashed line indicates the result for normal operation without the implementation of the damping controller. The solid lines shows the result for a system with damping controller implemented. As can be observed from the figure, the inclusion of the damping controller boosts the $\text{Re}[Z_{DFIG}(j\omega)Y_L(j\omega)]$ thereby avoiding the -1 margin. A variation in the open-loop resonance frequency is also observed due to the inclusion of the damping controller.

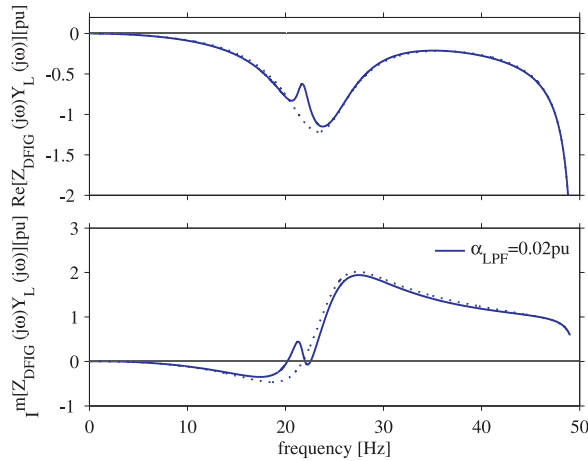


Fig. 6.9 Comparison of Impedance based Nyquist criterion for DFIG wind farm with and without damping controller when connected to series compensated transmission line. No damping controller (*dashed line*), with damping controller (*solid line*). $P_{out} = 0.72$ pu, $\alpha_{cc} = 1$ pu, $\alpha_{LPF} = 0.02$ pu and 55% compensation level.

Improved estimation algorithm for active mitigation

In the above analysis, the oscillatory frequency of the subsynchronous component is assumed to be known with good accuracy. However, in SSCI this assumption is not valid as the oscillatory frequency is dependent both on the operating conditions and the controller parameters considered. Therefore, an improved estimation algorithm with frequency adaptation is here proposed. Fig. 6.10 shows the block diagram of the proposed estimation algorithm.

6.4. Time domain based simulation verification

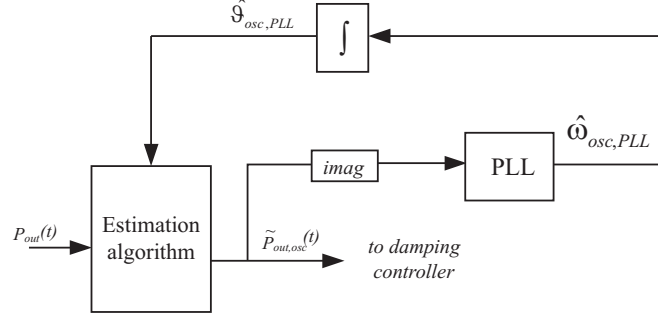


Fig. 6.10 Block diagram representation of estimation algorithm with frequency adaptation features

At the output of the estimation algorithm, a Frequency-Locked Loop (FLL) has been placed to estimate the frequency of the estimated subsynchronous component. The output from the FLL is the estimate of the angular frequency for the subsynchronous component. To ensure proper estimation, the angular frequency is integrated to obtain the estimated phase angle ($\hat{\theta}_{osc,PLL}$), which is then fed-back to the estimation algorithm. As a result, the estimation algorithm will involve frequency adaptation. The equation governing the FLL is given by

$$\hat{\omega}_{osc,PLL} = k_1 \varepsilon(t) \quad (6.7)$$

where $\varepsilon(t)$ is the error signal set to $\text{Im}[\hat{P}_{out,osc}(t)]$ where as k_1 is set to α_{PLL}^2 in accordance to [75]

6.4 Time domain based simulation verification

In the previous section, the effectiveness of the proposed passive and active mitigation for SSCI has been shown through impedance based frequency analysis. Here time-domain simulation results for the proposed techniques will be presented. The simulations have been carried out using the simulation program PSCAD/EMTDC and the controller for the DFIG is implemented using Fortran 90 language. A sampling frequency equal to $f_s = 5$ kHz has been used. Similar to the single-line diagram representation shown in Fig. 5.20, a parallel line is connected at the PCC to ensure stable operation, especially during system startup. Figure. 6.11 shows the result for the passive mitigation technique. Initially the wind farm is operated at $\alpha_{cc} = 1$ pu pushing $P_{out} = 0.72$ pu and $Q_{out} = 0$ pu into the grid that is on 55% series compensation. At time=4 sec, the circuit breaker in Fig. 5.20 is opened, causing the aggregated DFIG model to be radially connected to the series-compensated transmission line. In accordance to Fig. 6.11, a growing oscillation due to SSCI starts to build up. Once the estimated subsynchronous power exceeds the preset threshold, the bandwidth is lower immediately to avoid loss of controllability. The upper plot in Fig. 6.11 shows the results when α_{cc} is lowered to 0.5 pu and the middle plot for α_{cc} is lowered to 0.75 pu. Once the action is taken, for $\alpha_{cc} = 0.5$ pu, the subsynchronous component in the measured power dies very fast; however, the controller takes longer time to

Chapter 6. Utilization of DFIG Controller for SSR Mitigation

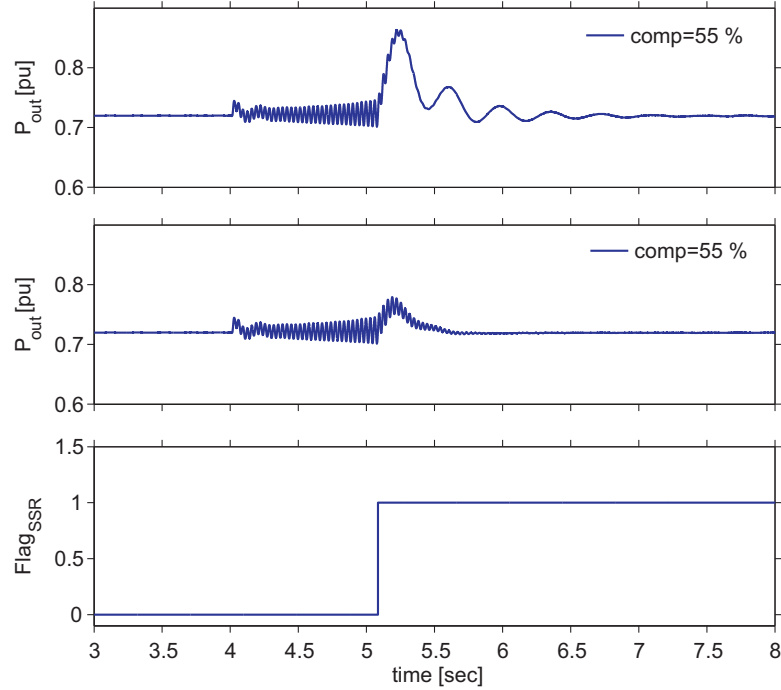


Fig. 6.11 Output power of a DFIG wind farm connected to a series compensated transmission line. *Upper plot*: Operation with passive controller, α_{cc} lowered to 0.5 pu when $Flag_{SSR}$ is enabled. *middle plot*: Operation with passive controller, α_{cc} lowered to 0.75 pu when $Flag_{SSR}$ is enabled. $P_{out} = 0.72$ pu, $Q_{out} = 0$ pu, $\alpha_{cc} = 1$ pu, $\alpha_{dc} = 0.2$ pu and 55% compensation level

bring the system back to the reference values. On the other hand, for $\alpha_{cc} = 0.75$ pu (Fig. 6.11, *middle plot*), the subsynchronous component in the power dies at a slower rate but at the same time the response of the controller is faster.

Presenting the results for subsynchronous speed range, Fig. 6.12 shows the results for $P_{out} = 0.25$ pu at 55% compensation. As can be observed from the figure, lowering α_{cc} to 0.5 pu, brings the system to stability whereas for $\alpha_{cc} = 0.75$ pu, the approach fails to ride-through the SSCI condition. From the result, it is evident that for lower wind speed (low P_{out}), lowering α_{cc} to 0.75 pu is insufficient to ensure passivity of the DFIG.

To summarize, lowering α_{cc} to 0.5 pu guarantees passivity for the investigated system.

To evaluate the proposed active mitigation technique (explained in Section 6.2.3) using time-domain simulation, an LPF-EA and a damping controller have been implemented in the RSC current controller loop. In the simulation model, the same steps are taken to open the breaker thereby creating a radial connection of the DFIG wind farm with the series-compensated transmission line. Parameter setting of $\alpha_{PF} = 0.02$ pu has been considered. Operating points corresponding to $P_{out} = 0.72$ pu and $Q_{out} = 0$ pu with $\alpha_{cc} = 1$ pu and $\alpha_{dc} = 0.2$ pu have been set. Fig. 6.13 shows the obtained simulation results for a transmission line operated at 55% series compensation. The upper plot shows the result when the controller takes no action to mitigate the SSCI condition whereas results in the lower plot shows the output power when the active damping controller is active. A closed-loop bandwidth of $\alpha_{LPF} = 0.02$ pu has been considered.

6.4. Time domain based simulation verification

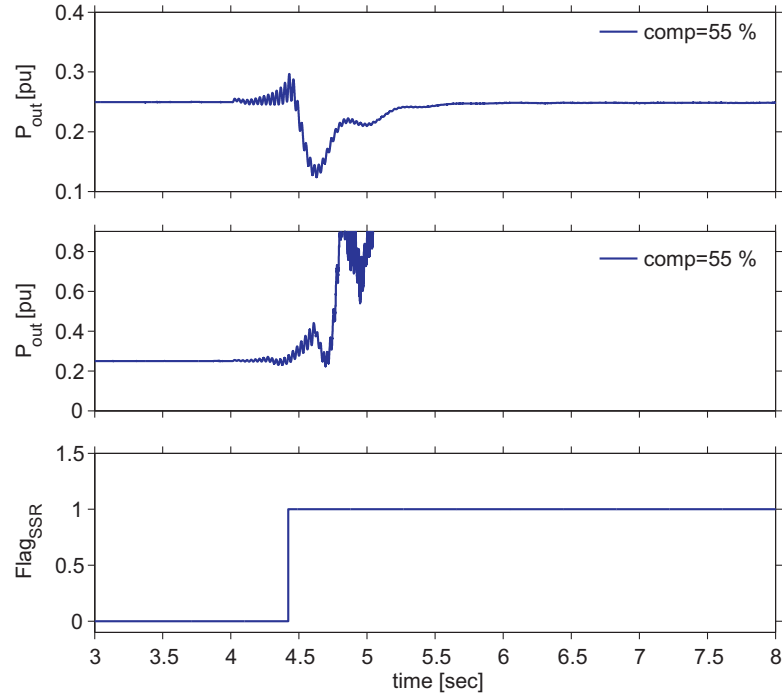


Fig. 6.12 Output power of a DFIG wind farm connected to a series compensated transmission line. *Upper plot*: Operation with passive controller, α_{cc} lowered to 0.5 pu when $Flag_{SSR}$ is enabled. *middle plot*: Operation with passive controller, α_{cc} lowered to 0.75 pu when $Flag_{SSR}$ is enabled. $P_{out} = 0.25$ pu, $Q_{out} = 0$ pu, $\alpha_{cc} = 1$ pu, $\alpha_{dc} = 0.2$ pu and 55% compensation level

From the result, it is evident that the damping controller is able to control the SSCI in this situation. Further results when the level of series compensation is increased is shown in Fig. 6.14.

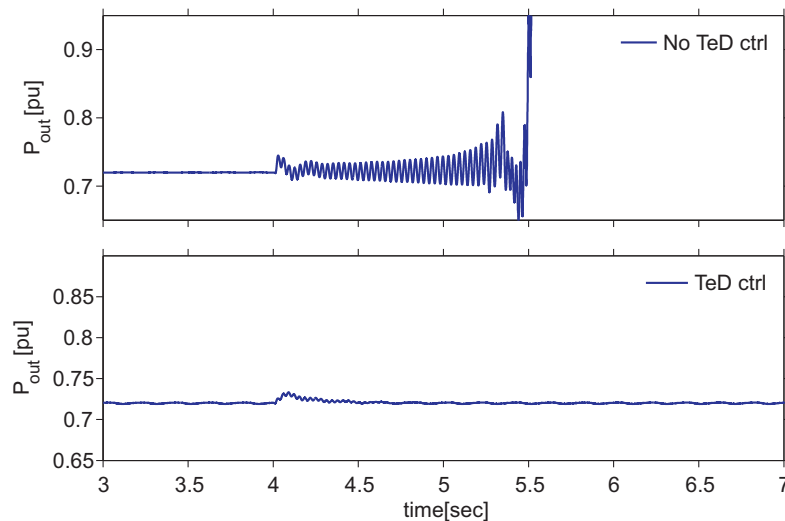


Fig. 6.13 Output power of a DFIG wind farm connected to a series compensated transmission line. *Upper plot*: Normal operation without damping controller. *Lower plot*: Operation with damping controller implemented. $P_{out} = 0.72$ pu, $Q_{out} = 0$ pu, $\alpha_{cc} = 1$ pu, $\alpha_{dc} = 0.2$ pu and 55% compensation level

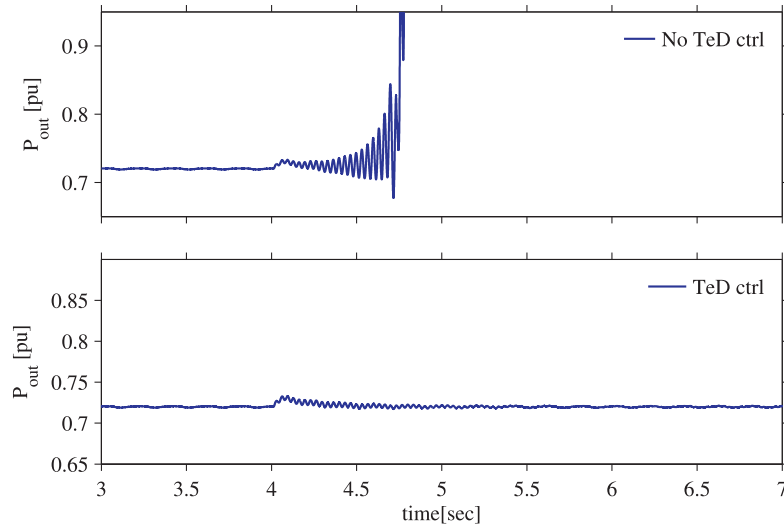


Fig. 6.14 Output power of a DFIG wind farm connected to a series compensated transmission line. *Upper plot*: Normal operation without damping controller. *Lower plot*: Operation with damping controller implemented. $P_{out} = 0.72$ pu, $Q_{out} = 0$ pu, $\alpha_{cc} = 1$ pu, $\alpha_{dc} = 0.2$ pu and 65% compensation level

6.5 Conclusion

This Chapter has presented the mitigation techniques for SSCI in DFIG based wind farms. First a passive mitigation technique that involved the shaping of the DFIG input impedance through variation of controller parameters has been presented. Following that an active mitigation technique employing an estimation algorithm and a proportional damping controller has been used to shape the input impedance of the DFIG. The impact of the investigated method on the DFIG impedance has been investigated. The passive mitigation technique shapes the impedance characteristics for the entire subsynchronous range while the active mitigation is specific to the frequency of interest. To further improve the active mitigation technique, frequency adaptation has been introduced to the estimation algorithms, in order to accurately estimate the subsynchronous oscillatory frequency.

The effectiveness of the proposed methods have been evaluated using impedance-based Nyquist criterion. The results have been further verified through time-domain simulation using PSCAD /EMTDC

Chapter 7

Conclusions and future work

7.1 Conclusions

This thesis has dealt with SubSynchronous Resonance (SSR) in wind farms connected to a series-compensated transmission line. In particular, the focus of this work has been on DFIG-based wind farms.

First, the risk of SSR in fixed-speed wind turbine has been investigated. It has been shown that for this turbine topology, SSR is mainly due to self excitation as a results of IGE. This is mainly due to the inherent negative resistance of the induction generator when operated under negative slip. Through frequency analysis, it has been shown that a FSIIG connected to a series-compensated transmission line presents an overall negative resistance at the systems resonance frequency. Hence, the system might be unable to dissipate energy at the resonance, leading to growing energy exchange and thereby instabilities.

To identify and analyze the risk for SSR in case of DFIG wind turbines, the development of proper mathematical models to understand the frequency behavior of the turbine becomes vital. Chapter 3 has been dedicated to shade an overview of the considered DFIG wind turbine model and its control structure. Thus, a linearized mathematical model has been derived (Chapter 4). In reference to the control structure presented in Chapter 3, the derived mathematical model has been verified against a full-switching model implemented in EMTDC/PSCAD. A mathematical model for the series-compensated transmission line has also been developed.

In Chapter 5 analytical evaluation using frequency dependent impedance has been used to identify the behavior of the DFIG model. The influence of the various components such as the induction generator, the RSC and the GSC control system on the overall DFIG impedance characteristics has been addressed. The impact of the induction generator is associated to the negative slip, which is directly affected by the operating point of the generator. However, the influence of the variation of the generator's rotor parameter on the DFIG resistance has been shown to be minimal. The RSC current controller loop bandwidth has a direct impact on the negative resistance presented by the DFIG, with higher bandwidth leading to a more negative resistance over a wide range of frequencies below the rated one. The outer active power control loop has instead

its main impact on the zero crossing of the DFIG reactance. On the contrary, the closed-loop inner current-controller bandwidth of the GSC is shown to have minimal influence on the DFIG impedance. The impact of the dc-link voltage control loop bandwidth is shown to be minimal; an impact is instead noticeable based on the system operating conditions, particularly depending on if the GSC is operated as an inverter or as a rectifier. In the same chapter, an aggregated DFIG based wind farm connected to a series-compensated transmission line has been modeled as a SISO feedback system where the wind farm impedance transfer function $Z_{DFIG}(s)$ and the transmission line transfer function $Y_L(s)$ have been defined. Here, an impedance-based Nyquist criterion has been utilized to evaluate the stability of the closed-loop system. Based on the obtained results, it has been shown that SSR in DFIG-based wind farms is mainly the result of SSCI, with the RSC closed-loop current control bandwidth playing a major role in the dynamic behavior of the system. The operating point, particularly whether the wind turbine is operated at subsynchronous or supersynchronous speed range, also greatly influences this phenomenon.

Based on the frequency-domain analysis performed in Chapter 5, mitigation techniques utilizing the DFIG turbine control have been suggested. Two approaches have been proposed. The first approach, referred to as passive mitigation approach, implies the online variation of the RSC current control loop bandwidth in the event of SSCI, in order to modify the DFIG input impedance and thereby making the generator system passive to SSCI. It has been shown that a lowered bandwidth $\alpha_{cc,R}$ of the RSC current control loop improves the passivity of the generator system, thereby minimizing the risk for SSCI. The operation of the wind turbine under reduced bandwidth must be limited from the detection up until the clearing of the SSCI condition. The second approach suggests the modification to the DFIG control system, aiming at enhancing the system damping at a frequency of interest by introducing a proportional damping controller in the RSC current controller loop. Both frequency-domain analysis and time-domain simulation have been used to assess the effectiveness of the investigated method. To estimate the subsynchronous component in the output power, an estimator based on a combination of low-pass filters has been employed. Since the resonance frequency of the system is highly determined by the operating condition and the control parameter, a modification for the active damping approach involving Frequency-Locked Loop (FLL) to track the oscillatory frequency of the SSCI has also been proposed in Chapter 6. Simulation results have proven the effectiveness of the suggested approach in mitigating subsynchronous resonances for the investigated systems.

7.2 Future work

The investigation of resonant conditions in complex systems with high penetration of power electronic devices is a complex task. In this thesis, the investigation has been carried out under the assumption that the entire wind farm can be represented by a single aggregate wind turbine model, scaled up to the wind farm ratings. While this approach helps in understanding the mechanisms that lead to an unstable condition and the parameters that most contribute to it, it might not properly resemble the behavior of an actual wind farm and thereby lead to unrealistic results. The wind farm layout as well as the different operating conditions of the various wind turbines will have an impact on the frequency response of the overall system. For this reason,

7.2. Future work

a natural next step in the investigation is to establish an effective method to properly model the entire wind farm, accounting for the impact of multiple power electronic components and the frequency characteristic of the collection grid. In addition, it has been shown that by equipping the control system of the rotor-side converter with a dedicated SSR damping controller, unstable conditions can be avoided; it will be of interest to investigate the impact of such a controller on the DFIG VSC ratings.

The focus of this thesis has been on DFIG-based wind farms. Investigation relating to the risk of SSR in full power converter type wind turbines has not been here addressed. Although there exists no reported incidents related to SSR in this type of wind turbines, investigation to rule out the risk of SSCI between the control system of the BTB converter and the series-compensated transmission line is of high interest.

Finally, it has been shown that by varying the control system parameters or through the use of damping controllers, it is possible to overcome the risk for SSR. However, this solution might be insufficient under some circumstances or when considering a more realistic wind farm model. In such cases, external power electronic controllers, such as STATCOMs connected to the point of common coupling with the grid, might be necessary to mitigate unstable conditions. However, due to the variable nature of the frequency characteristic of the wind turbines, the control of such devices is not trivial and needs a deep investigation.

Chapter 7. Conclusions and future work

References

- [1] IEEE SSR Working Group, “Terms, Definitions and Symbols for Subsynchronous Oscillations,” *IEEE Transaction*, vol. PAS-104, June 1985.
- [2] P. Anderson and R. Farmer, *Series Compensation of Power Systems*. United States of America: PBLSH, 1991.
- [3] “Concept of SSR.” [Online]. Available: <http://www.ercot.com/calendar/2013/9/9/32814>
- [4] H. A. Mohammadpour and E. Santi, “Analysis of Subsynchronous Control Interactions in DFIG-based Wind Farms: ERCOT case study,” in *2015 IEEE Energy Conversion Congress and Exposition (ECCE)*, Sept 2015, pp. 500–505.
- [5] R. K. Varma, S. Auddy, and Y. Semsedini, “Mitigation of Subsynchronous Resonance in a Series-Compensated Wind Farm using FACTS Controllers,” *IEEE Transactions on Power Delivery*, vol. 23, no. 3, pp. 1645–1654, July 2008.
- [6] P. Pourbeik, R. Koessler, D. Dickmader, and W. Wong, “Integration of Large Wind Farms into Utility Grids (Part 2-Performance Issues),” in *Power Engineering Society General Meeting, 2003, IEEE*, vol. 3. IEEE, 2003.
- [7] A. Tabesh and R. Iravani, “Small-Signal Model and Dynamic Analysis of Variable Speed Induction Machine Wind Farms,” *Renewable Power Generation, IET*, vol. 2, no. 4, pp. 215–227, December 2008.
- [8] H. Xie, B. Li, C. Heyman, M. de Oliveira, and M. Monge, “Subsynchronous Resonance Characteristics in Presence of Doubly-Fed Induction Generator and Series Compensation and Mitigation of Subsynchronous Resonance by Proper Control of Series Capacitor,” *Renewable Power Generation, IET*, vol. 8, no. 4, pp. 411–421, May 2014.
- [9] L. Fan, R. Kavasseri, Z. L. Miao, and C. Zhu, “Modeling of DFIG-based Wind Farms for SSR Analysis,” *IEEE Transactions on Power Delivery*, vol. 25, no. 4, pp. 2073–2082, Oct 2010.
- [10] A. Ostadi, A. Yazdani, and R. K. Varma, “Modeling and Stability Analysis of a DFIG-based Wind-Power Generator Interfaced With a Series-Compensated Line,” *IEEE Transactions on Power Delivery*, vol. 24, no. 3, pp. 1504–1514, July 2009.

References

- [11] C. Zhu, M. Hu, and Z. Wu, "Parameters impact on the performance of a double-fed induction generator-based wind turbine for subsynchronous resonance control," *IET Renewable Power Generation*, vol. 6, no. 2, pp. 92–98, March 2012.
- [12] L. Wang, X. Xie, Q. Jiang, H. Liu, Y. Li, and H. Liu, "Investigation of SSR in Practical DFIG-based Wind Farms Connected to a Series-Compensated Power System," *IEEE Transactions on Power Systems*, vol. 30, no. 5, pp. 2772–2779, Sept 2015.
- [13] L. Fan and Z. Miao, "Nyquist-Stability-Criterion-based SSR Explanation for Type-3 Wind Generators," *IEEE Transactions on Energy Conversion*, vol. 27, no. 3, pp. 807–809, Sept 2012.
- [14] Z. Miao, "Impedance-Model based SSR Analysis for Type 3 Wind Generator and Series-Compensated Network," *IEEE Transactions on Energy Conversion*, vol. 27, no. 4, pp. 984–991, Dec 2012.
- [15] N. G. Hingorani and L. Gyugyi, *Understanding FACTS. Concepts and Technology of Flexible AC Transmission Systems*,. New York: John Wiley & Sons, Inc, 1999.
- [16] T. Ackermann, *Wind Power in Power Systems*. John Wiley & Sons, 2005.
- [17] P. Pourbeik, R. Koessler, D. Dickmader, and W. Wong, "Integration of Large Wind Farms into Utility Grids (part 2 - Performance Issues)," in *Power Engineering Society General Meeting, 2003, IEEE*, vol. 3, July 2003, pp. 1520–1525 Vol. 3.
- [18] J. Butler and C. Concordia, "Analysis of Series Capacitor Application Problems," *Electrical Engineering*, vol. 57, no. 2, pp. 110–111, Feb 1938.
- [19] C. Wagner, "Self-Excitation of Induction Motors with Series Capacitors," *Electrical Engineering*, vol. 60, no. 12, pp. 1241–1247, 1941.
- [20] M. Hall and D. Hodges, "Experience with 500-kv Subsynchronous Resonance and Resulting Turbine Generator Shaft Damage at Mohave Generating Station," *IEEE PES Special Publication, Analysis and Control of Subsynchronous Resonance, IEEE Publication*, vol. 76, pp. 22–29, 1976.
- [21] R. Farmer, A. Schwalb, and E. Katz, "Navajo Project Report on Subsynchronous Resonance Analysis and Solutions," *IEEE Transactions on Power Apparatus and Systems*, vol. 96, no. 4, pp. 1226–1232, July 1977.
- [22] M. Bongiorno, A. Peterson, and E. Agneholm, "The Impact of Wind Farm on Subsynchronous Resonance in Power Systems," Elforsk, Stockholm, Sweden, Elforsk Report 11:29, May, 2011.
- [23] T. Ackermann and R. Kuwahata, "Lesson Learned from International Wind Integration Studies," Australian Energy Market Operator, Melbourne, Australia, Tech. Rep., 2011.

- [24] R. K. Varma, S. Auddy, and Y. Semsedini, "Mitigation of Subsynchronous Resonance in a Series-Compensated Wind Farm using FACTS Controllers," *IEEE Transactions on Power Delivery*, vol. 23, no. 3, pp. 1645–1654, 2008.
- [25] P. Anderson, B. Agrawal, and J. V. Ness, *Subsynchronous Resonance in Power Systems*. New York, United States of America: IEEE Press, 1989.
- [26] K. Padiyar, *Analysis of Subsynchronous Resonance in Power Systems*. United States of America: Kluwer Academic Publishers, 1999.
- [27] M. Bongiorno, J. Svensson, and L. Angquist, "Online Estimation of Subsynchronous Voltage Components in Power Systems," *IEEE Transactions on Power Delivery*, vol. 23, no. 1, pp. 410–418, 2008.
- [28] M. Bongiorno, "On Control of Grid-connected Voltage Source Converter," Chalmers University of Technology, Gothenburg, Sweden, PhD Thesis, 2007.
- [29] L. Harnefors, M. Bongiorno, and S. Lundberg, "Input-Admittance Calculation and Shaping for Controlled Voltage-Source Converters," *IEEE Transactions on Industrial Electronics*, vol. 54, no. 6, pp. 3323–3334, Dec 2007.
- [30] J. Sun, "Impedance-based Stability Criterion for Grid-Connected Inverters," *Power Electronics, IEEE Transactions on*, vol. 26, no. 11, pp. 3075–3078, Nov 2011.
- [31] A. Bayo-Salas, J. Beerten, J. Rimez, and D. Van Hertem, "Impedance-based Stability Assessment of Parallel VSC HVDC Grid Connections," in *11th IET International Conference on AC and DC Power Transmission*, Feb 2015, pp. 1–9.
- [32] J. E. Slotine and W. Li, *Applied Nonlinear Control*. New Jersey: Prentice-hall Englewood Cliffs, 1991, vol. 199, no. 1.
- [33] G. Stamatiou, *Converter Interactions in VSC-based HVDC Systems*. Department of Energy and Environment, Electrical Power Engineering, Chalmers University of Technology, 2015, 222.
- [34] G. Pinares, *On the Analysis of DC Network Dynamics of VSC-based HVDC Systems*. Department of Energy and Environment, Electrical Power Engineering, Chalmers University of Technology, 2014, 141.
- [35] L. H. Hansen, L. Helle, F. Blaabjerg, E. Ritchie, S. Munk-Nielsen, H. W. Bindner, P. E. Sørensen, and B. Bak-Jensen, *Conceptual Survey of Generators and Power Electronics for Wind Turbines*. Technical University of Denmark, 2002.
- [36] L. Harnefors, "Modeling of Three-Phase Dynamic Systems using Complex Transfer Functions and Transfer Matrices," *IEEE Transactions on Industrial Electronics*, vol. 54, no. 4, pp. 2239–2248, 2007.

References

- [37] F. Fateh, W. Warren.N., and D. Gruenbacher, "Mitigation of Torsional Vibration in the Drivetrain of DFIG based Grid-Connected Wind Turbine," in *Seventh Annual IEEE Energy Conversion Congress and Exposition*, September 2015.
- [38] A. Petersson, "Analysis, Modeling and Control of Doubly-Fed Induction Generators for Wind Turbines," Ph.D. dissertation, Chalmers University of Technology, 2005.
- [39] H. Mohammadpour, Y. J. Shin, and E. Santi, "SSR analysis of a DFIG-based Wind Farm Interfaced with a Gate-Controlled Series Capacitor," in *Twenty-Ninth Annual IEEE Applied Power Electronics Conference and Exposition (APEC), 2014*, March 2014, pp. 3110–3117.
- [40] G. Slemon, "Modelling of Induction machines for Electric Drives," *IEEE Transactions on Industry Applications*, vol. 25, no. 6, pp. 1126–1131, Nov 1989.
- [41] A. Petersson, "Analysis, Modeling and Control of Doubly-Fed Induction Generators for Wind Turbines," Chalmers University of Technology, Gothenburg, Sweden, Licentiate Thesis, 2003.
- [42] M. Bongiorno and T. Thiringer, "A Generic DFIG Model for Voltage Dip Ride-Through Analysis," *IEEE Transactions on Energy Conversion*, vol. 28, no. 1, pp. 76–85, March 2013.
- [43] G. Tarnowski, P. Kjaer, S. Dalsgaard, and A. Nyborg, "Regulation and Frequency Response Service Capability of Modern Wind Power Plants," in *IEEE Power and Energy Society General Meeting, 2010*, July 2010, pp. 1–8.
- [44] R. Datta and V. Ranganathan, "Decoupled Control of Active and Reactive Power for a Grid-Connected Doubly-Fed Wound Rotor Induction Machine without Position Sensors," in *Thirty-Fourth IAS Annual Industry Applications Conference, 1999. . Conference Record of the 1999 IEEE*, vol. 4, 1999, pp. 2623–2630 vol.4.
- [45] R. Ottersten, "On Control of Back-to-Back Connected and Sensorless Induction Machine Drives," Chalmers University of Technology, Gothenburg, Sweden, PhD Thesis, 2003.
- [46] L. Harnefors and H.-P. Nee, "Model-based Current Control of AC Machines using the Internal Model Control Method," *IEEE Transactions on Industry Applications*, vol. 34, no. 1, pp. 133–141, 1998.
- [47] L. Harnefors, *Control of Power Electronic Converter and Variable-Speed Drives*. Västerås, Sweden: Applied Signal Processing and Control, Dept. of Electronics, Mälardalen University, 2002.
- [48] O. Wallmark, L. Harnefors, and O. Carlson, "An Improved Speed and Position Estimator for Salient Permanent-Magnet Synchronous Motors," *IEEE Transactions on Industrial Electronics*, vol. 52, no. 1, pp. 255–262, 2005.
- [49] I. Vieto and J. Sun, "Small-Signal Impedance Modelling of Type-III Wind Turbine," in *2015 IEEE Power Energy Society General Meeting*, July 2015, pp. 1–5.

- [50] L. Harnefors, "Proof and Application of the Positive-Net-Damping Stability Criterion," *IEEE Transactions on Power Systems*, vol. 26, no. 1, pp. 481–482, Feb 2011.
- [51] I. M. Canay, "A Novel Approach to the Torsional interaction and Electrical Damping of the Synchronous Machine. part I: Theory," *IEEE Power Engineering Review*, vol. PER-2, no. 10, pp. 24–24, Oct 1982.
- [52] I. Canay, "A Novel Approach to the Torsional Interaction and Electrical Damping of the Synchronous Machine part II: Application to an Arbitrary Network," *IEEE Transactions on Power Apparatus and Systems*, vol. PAS-101, no. 10, pp. 3639–3647, Oct 1982.
- [53] R. Nath and C. Grande-Moran, "Study of Sub-Synchronous Control Interaction due to the Interconnection of Wind Farms to a Series Compensated Transmission System," in *Transmission and Distribution Conference and Exposition (T D), 2012 IEEE PES*, May 2012, pp. 1–6.
- [54] D. Xiaoliang and X. Xiaorong, "Influence of DFIG Controller Parameter on SSR Under all Operation Areas," in *Power System Technology (POWERCON), 2014 International Conference on*, Oct 2014, pp. 2618–2622.
- [55] "Overview of Subsynchronous Resonance Analysis and Control in Wind Turbines," *Renewable and Sustainable Energy Reviews*, vol. 27, pp. 234 – 243, 2013.
- [56] E. L. Rees, "Graphical Discussion of the Roots of a Quartic Equation," *The American Mathematical Monthly*, vol. 29, no. 2, pp. 51–55, Feb. 1922.
- [57] M. S. El-Moursi, B. Bak-Jensen, and M. H. Abdel-Rahman, "Novel STATCOM Controller for Mitigating SSR and Damping Power System Oscillations in a Series Compensated Wind Park," *IEEE Transactions on Power Electronics*, vol. 25, no. 2, pp. 429–441, Feb 2010.
- [58] S. Golshannavaz, M. Mokhtari, and D. Nazarpour, "SSR Suppression via STATCOM in Series Compensated Wind Farm Integrations," in *19th Iranian Conference on Electrical Engineering, 2011*, May 2011, pp. 1–6.
- [59] H. Xie and M. M. de Oliveira, "Mitigation of SSR in presence of Wind Power and Series Compensation by SVC," in *International Conference on Power System Technology (POWERCON), 2014*, Oct 2014, pp. 2819–2826.
- [60] H. A. Mohammadpour and E. Santi, "Modeling and Control of Gate-Controlled Series Capacitor Interfaced with a DFIG-based Wind Farm," *IEEE Transactions on Industrial Electronics*, vol. 62, no. 2, pp. 1022–1033, Feb 2015.
- [61] H. A. Mohammadpour, J. Siegers, and E. Santi, "Controller Design for TCSC using Observed-State Feedback Method to Damp SSR in DFIG-based Wind Farms," in *IEEE Applied Power Electronics Conference and Exposition (APEC), 2015*, March 2015, pp. 2993–2998.

References

- [62] H. A. Mohammadpour and E. Santi, "Sub-synchronous Resonance Analysis in DFIG-based Wind Farms: Mitigation Methods; TCSC, GCSC, and dfig controllers - Part II," in *IEEE Energy Conversion Congress and Exposition (ECCE), 2014*, Sept 2014, pp. 1550–1557.
- [63] A. E. Leon and J. A. Solsona, "Sub-synchronous Interaction Damping Control for DFIG Wind Turbines," *IEEE Transactions on Power Systems*, vol. 30, no. 1, pp. 419–428, Jan 2015.
- [64] P. H. Huang, M. S. E. Moursi, W. Xiao, and J. L. Kirtley, "Subsynchronous Resonance Mitigation for Series-Compensated DFIG-based Wind Farm by using Two-Degree-of-Freedom Control Strategy," *IEEE Transactions on Power Systems*, vol. 30, no. 3, pp. 1442–1454, May 2015.
- [65] I. Vieto and J. Sun, "Damping of Subsynchronous Resonance involving Type-III Wind Turbines," in *IEEE 16th Workshop on Control and Modeling for Power Electronics (COMPEL), 2015*, July 2015, pp. 1–8.
- [66] H. Liu, X. Xie, Y. Li, H. Liu, and Y. Li, "Damping DFIG-Associated SSR with Sub-synchronous Suppression Filters: A Case Study on a Practical Wind Farm System," in *International Conference on Renewable Power Generation (RPG 2015)*, Oct 2015, pp. 1–6.
- [67] H. Liu, X. Xie, Y. Li, H. Liu, and Y. Hu, "Damping Subsynchronous Resonance in Series-Compensated Wind Farms by adding Notch Filters to DFIG Controllers," in *IEEE Innovative Smart Grid Technologies - Asia (ISGT ASIA), 2015*, Nov 2015, pp. 1–5.
- [68] X. Xie, L. Wang, H. Liu, H. Liu, and Y. Li, "A Mechanism Study of SSR for Multiple DFIG Wind Generators Connected to a Series-Compensated Power System," in *International Conference on Power System Technology (POWERCON), 2014*, Oct 2014, pp. 2769–2774.
- [69] G. D. Irwin, A. K. Jindal, and A. L. Isaacs, "Sub-synchronous Control Interactions between Type-3 Wind Turbines and Series Compensated AC Transmission Systems," in *2011 IEEE Power and Energy Society General Meeting*, July 2011, pp. 1–6.
- [70] D. Xiaoliang and X. Xiaorong, "Influence of DFIG Controller Parameter on SSR under all Operation Areas," in *International Conference on Power System Technology (POWERCON), 2014*, Oct 2014, pp. 2618–2622.
- [71] L. Fan and Z. Miao, "Mitigating SSR Using DFIG-Based Wind Generation," *IEEE Transactions on Sustainable Energy*, vol. 3, no. 3, pp. 349–358, July 2012.
- [72] H. A. Mohammadpour and E. Santi, "SSR Damping Controller Design and Optimal Placement in Rotor-Side and Grid-Side Converters of Series-Compensated DFIG-based Wind Farm," *IEEE Transactions on Sustainable Energy*, vol. 6, no. 2, pp. 388–399, April 2015.

References

- [73] L. Angquist and C. Gama, “Damping Algorithm based on Phasor Estimation,” in *Power Engineering Society Winter Meeting, 2001. IEEE*, vol. 3, 2001, pp. 1160–1165 vol.3.
- [74] M. Beza, *Power System Stability Enhancement Using Shunt-Connected Power Electronic Devices with Active Power Injection Capability*. Departement of Energy and Environment, Electrical Power Engineering, Chalmers University of Technology, 2015, 168.
- [75] L. Angquist and M. Bongiorno, “Auto-normalizing Phase-Locked Loop for Grid-connected Converters,” in *IEEE Energy Conversion Congress and Exposition, 2009. ECCE 2009.*, Sept 2009, pp. 2957–2964.
- [76] IEEE SSR Task Force, “First Benchmark Model for Computer Simulation of Subsynchronous Resonance,” *IEEE Transaction on Power System Applications*, vol. PAS-9618, no. 5, pp. 1565–1571, Sept./Oct. 1977.

References

Appendix A

Transformation for three-phase system

A.1 Introduction

In this appendix, the transformation used to extract the complex vector from three-phase quantities and vice versa is presented.

A.1.1 Transformation of three-phase quantities into vectors

A three-phase system composed of three quantities, $s_a(t)$, $s_b(t)$ and $s_c(t)$ can be transformed into a vector having two components in a stationary complex reference frame, referred to as xy by applying the transformation stated by

$$\underline{s}^{xy}(t) = s_x + js_y = K \left[s_a(t) + s_b(t) e^{j\frac{2}{3}\pi} + s_c(t) e^{j\frac{4}{3}\pi} \right] \quad (\text{A.1})$$

The transformation constant K can be chosen between 1, $\sqrt{1/2}$ or $\sqrt{2/3}$ to obtain amplitude invariant, rms invariant or power invariant transformation, respectively. The expression of (A.1) is expressed in matrix form as (A.2)

$$\begin{bmatrix} s_x(t) \\ s_y(t) \end{bmatrix} = \mathbf{T}_{32} \begin{bmatrix} s_a(t) \\ s_b(t) \\ s_c(t) \end{bmatrix} \quad (\text{A.2})$$

where the matrix \mathbf{T}_{32} is expressed as

$$\mathbf{T}_{32} = K \begin{bmatrix} 1 & -\frac{1}{2} & -\frac{1}{2} \\ 0 & \frac{\sqrt{3}}{2} & -\frac{\sqrt{3}}{2} \end{bmatrix}$$

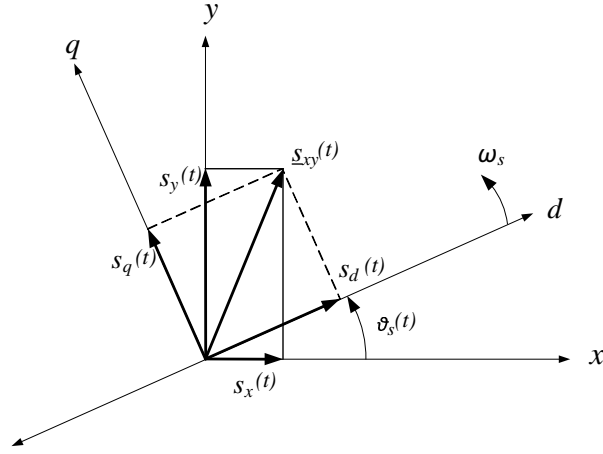


Figure A.1: Relation between xy -frame and dq -frame

Assuming there is no zero sequence, the inverse transformation is given by

$$\begin{bmatrix} s_a(t) \\ s_b(t) \\ s_c(t) \end{bmatrix} = \mathbf{T}_{23} \begin{bmatrix} s_x(t) \\ s_y(t) \end{bmatrix} \quad (\text{A.3})$$

where the matrix \mathbf{T}_{23} is given by

$$\mathbf{T}_{32} = \frac{1}{K} \begin{bmatrix} \frac{2}{\sqrt{3}} & 0 \\ -\frac{1}{\sqrt{3}} & \frac{1}{\sqrt{3}} \\ -\frac{1}{\sqrt{3}} & -\frac{1}{\sqrt{3}} \end{bmatrix}$$

A.1.2 Transformation from fixed to rotating reference frame

For a vector expressed as \underline{s}_{xy} in the xy -frame having an angular frequency $\omega_s(t)$ in the counter-clockwise direction, a rotating dq -frame that rotates with the same angular frequency $\omega_s(t)$ can be defined. In this rotating reference frame, the vector \underline{s}_{xy} appears as a fixed vector. By projecting the vector \underline{s}_{xy} in the d -axis and q -axis of the dq -frame, the components of the vector in the dq frame can be obtained as illustrated in Fig. A.1

The transformation can be expressed using vector notations as

$$\underline{s}_{dq}(t) = s_d(t) + js_q(t) = \underline{s}_{xy}(t)e^{-j\vartheta_s(t)} \quad (\text{A.4})$$

where $\vartheta_s(t)$ is expressed as

$$\vartheta_s(t) = \vartheta_s^0(t) + \int \omega_s(t)dt$$

The inverse transformation from the rotating dq -frame is expressed as

$$\underline{s}_{xy}(t) = \underline{s}_{dq}(t)e^{j\vartheta_s(t)} \quad (\text{A.5})$$

Chapter A. Transformation for three-phase system

Appendix B

Benchmark Model for SSR Studies

B.1 Introduction

In this appendix, the two IEEE benchmark model used for SSR studies are introduced. The first IEEE benchmark model deals with SSR as a result of radial resonance while the second benchmark model deals with parallel resonance in the power system

B.1.1 IEEE First Benchmark Model (IEEE FBM)

The IEEE First Benchmark Model (IEEE FBM) shown in Fig. B.1 is based on a radial connection of a 892.4 MVA synchronous generator connected to a series compensated transmission network [25] [76]. The system has a rated voltage of 539 kV and a rated frequency of 60 Hz. The parameters for the synchronous generator and for the transmission line can be found in Table B.1 and Table B.2, respectively. The generator shaft model parameters are reported in Table B.3.

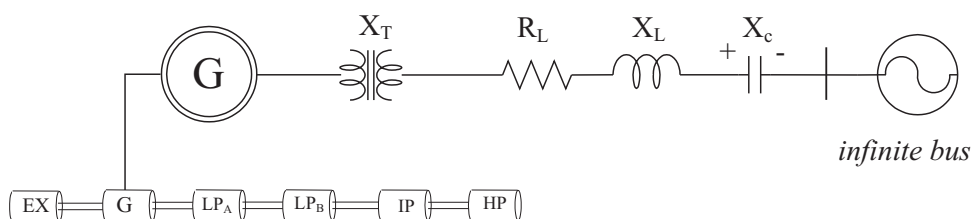


Fig. B.1 Single-line diagram of IEEE first benchmark model

Chapter B. Benchmark Model for SSR Studies

TABLE B.1: IEEE FBM Synchronous Generator Parameters

Reactance	Values [pu]	Time constants	Value [sec]
$X_{a\sigma}$	0.13	T'_{d0}	4.3
X_d	1.79	T''_{d0}	0.032
X'_d	0.169	T'_{q0}	0.85
X''_d	0.135	T''_{q0}	0.05
X'_q	0.228		
X''_q	0.2		

TABLE B.2: IEEE FBM Network Parameters

Network resistance	R_L	0.02 pu
Transformer reactance	X_T	0.14 pu
Transformer ratio		26/539 kV
Line reactance	X_L	0.5 pu

TABLE B.3: IEEE FBM Shaft Parameters

Mass	Inertia H [s^{-1}]	Shaft section	Spring constant K [pu T/rad]
	H [s^{-1}]		K [pu T/rad]
HP turbine	0.092897	HP-IP	19.303
IP turbine	0.155589	IP-LPA	34.929
LPA turbine	0.858670	LPA-LPB	52.038
LPB turbine	0.884215	LPB-GEN	70.858
Generator	0.868495	GEN-EX	2.82
Exciter	0.0342165		

The IEEE FBM has been modified to accommodate an aggregate DFIG based wind farm, the parameter of which are presented in Table B.4. The Network parameter for the modified IEEE FBM is given in Table B.6

TABLE B.4: DFIG Aggregate Model parameter

Rated power	100 MW
Rated voltage	33 kV
X_{ls}	0.158367 pu
X_m	3.8271871 pu
X_{lr}	0.065986 pu
R_s	0.0092417 pu
R_r	0.0075614 pu
X_f	1.055 pu
R_f	0.1055 pu
C_{dc}	$\frac{50 \times 20000}{(33/0.69)^2} \mu F$

TABLE B.5: Induction Generator Parameters

Rated power	100 MW
Rated voltage	26 KV
X_{ls}	0.08168 pu
X_{lr}	0.14870 pu
X_m	4.289 pu
R_s	0.004820 pu
R_r	0.006313 pu

TABLE B.6: Network Parameters for DFIG Farm

Network resistance	R_L	0.02 pu
Transformer reactance	X_T	0.14 pu
Transformer resistance	R_{TL}	0.00146 pu
Transformer ratio		33/161 kV
Line reactance	X_L	0.1 pu
Line resistance	R_L	0.02 pu
Series compensation	X_c	% of X_L
Line reactance (line 2)	X_{L2}	0.1 pu
Line resistance (line 2)	R_{L2}	0.002 pu

Chapter B. Benchmark Model for SSR Studies